Synthesis of core-shell high-K nanoparticles

Yanling Gao

Faculty of Engineering

University of Duisburg-Essen

This dissertation is submitted for the degree of

Doctor of Philosophy

Institute for Material Science 2015

Tag der mündlichen Prüfung: 08.09.2015

Erstgutachter: Prof. Dr. rer. nat. Doru C. Lupascu

Zweitgutachter: Prof. Paula Maria Vilarinho

I would like to dedicate this thesis to my loving parents, Yong Gao and Chunying Zhang, who have always loved me unconditionally and whose good examples have taught me to work hard for the things that I aspire to achieve. This work is also dedicated to my husband, Aijun Zhang, who has been a constant source of support and encouragement during the challenges of life. I am truly thankful for having you in my life.

Declaration

I hereby declare that except where specific reference is made to the work of others, the contents of this dissertation are original and have not been submitted in whole or in part for consideration for any other degree or qualification in this, or any other University. This dissertation is the result of my own work and includes nothing which is the outcome of work done in collaboration, except where specifically indicated in the text. This dissertation contains fewer than 65,000 words including appendices, reference, footnotes, tables and equations and has less than 150 figures.

Yanling Gao
2015

Acknowledgements

During my PhD study, I got a lot of help and encouragement. I would glad to express my appreciation and acknowledgement during this exciting journey.

First and foremost, I would like to thank Prof. Dr. D. C. Lupascu, my advisor and first reader of this dissertation, for his kind guidance during my PhD study. His passionate, diligent, critic-thinking influences my research tremendously. I am impressed by his knowledge, strong logic and creativity. Without his mentoring, it is impossible for me to survive and finish my PhD study.

I would like to express my gratitude to Frau Prof. Paula Vilarinho from the Department of Materials and Ceramic Engineering at the University of Aveiro for being my second reader of this dissertation.

I would also like to thank Prof. Dr. Schmechel, Prof. Dr. Behrens and Frau Prof. Birk for serving on my thesis committee and providing additional guidance and support. Their kindness and pertinent advice always broaden my horizons in research.

I am very lucky to have great members in our dynamic group: Hans-Joachim Keck, Sabine Kriegel, Vladimir Shvartsman, Irina Anusca, Miriana Vadala, Morad Etier, Danka Gobeljic, Gerhard Lackner, Susanne Palecki, Marianela Escobar, Maryam Khazaee, Ahmadshah Nazrabi, Mehmet Sanlialp, Harsh Trivedi, Kevin Voges, Nadia Gharbi, Simon Kugai, Marc Borbe, Alfred Gäbel, Patrick Dubray, Stefan Nawrath. They provided a friendly and cooperative atmosphere at work and made my daily life here joyful. Particularly grateful to Vladimir Shvartsman, who helped me a lot with important comments and suggestions in research and to Patrick Dubray, who not only introduced me to various techniques in the lab but also helped me with every problem concerning my practical work.

I would like to thank to Prof. Dr. Markus Winterer from Laboratory for Nanoparticle Process Technology at the University of Duisburg-Essen for the preparation of $Ba_{0.6}Sr_{0.4}TiO_3$ nanoceramics by Spark Plasma Sintering.

I also would like to express thanks to Prof. Dr. Matthias Epple from Institute for inorganic chemistry at the University of Duisburg-Essen for performing the FT-IR measuremnts and to Prof. Dr. Mathias Ulbricht from Institute of Technical Chemistry II at the University of Duisburg-Essen for the measurements of particle size distribution and streaming/zeta

potential. The data provided by them helped me a lot to accomplish this work.

The supports of the Center for Nanointegration Duisburg-Essen (CENIDE) are gratefully acknowledged.

Thanks to my other colleagues for their scientific helps during the research work, who give selfless collaboration and contribution to my work: Anna Elsukova, Inge Danielzik, Smail Boukercha, Kateryna Loza, Miriam Engel, Yang Liu, Devendraprakash Gautami.

Abstract

In recent years, the development of core@shell structured nanoparticles has received great research attention because of the combination of different properties in one particle based on different compositions of the core and the shell. The core often shows the relevant property (e.g. semiconductors, metals, magnetic oxides, encapsulated molecules), while the shell can not only avoid the aggregation and oxidation of the particles, but also can alter the dispersion characteristics of the particles by surface modification, so that the possibility is given to blend the core@shell particles into the polymer matrices.

$BaTiO_3$ is one of well-known dielectric materials that is also used in a variety of semiconductor devices owing to its high and frequency-independent permittivity with low dielectric loss. In this work, we aspire to develop a versatile, cost efficient, environmental friendly, and easy-to-scale up method for synthesizing $BaTiO_3$ nanoparticles and $BaTiO_3$-based different types of core@shell nanoparticles: $BaTiO_3$@SiO_2 and Ag@$BaTiO_3$ with the core@shell structure.

The "Organosol" sythesis is proposed to produce hydrophobic $BaTiO_3$ nanoparticles at temperatures as low as room temperature. The advantages of this method are a high yield, a simple but precise control of the size of the particles, low process temperature, short reaction time, as well as low cost of reagents.

$BaTiO_3$@SiO_2 compsite nanoparticles with tunable thickness from 3 nm to 20 nm are successfully prepared by a reverse microemulsion method. Specifically, the formation of $BaTiO_3$@SiO_2 is performed by using hydrophobic BaTiO3 nanoparticles as seeds in a Triton X-100/n-hexanol/cyclohexane/water reverse microemulsion (W/O). The shell is formed by hydrolysis and condensation of tetraethyl-orthosilicate (TEOS) on the surface of the $BaTiO_3$ particles. The TEM and EDS elemental mapping images clearly show that the $BaTiO_3$@SiO_2 compsite nanoparticles have a core@shell structure.

Ag@$BaTiO_3$ composite nanoparticles with tunable optical properties were formed in two steps: (1) the synthesis of a Ag organosol, (2) followed by its incorporation with $BaTiO_3$ "organosol" precursor to prepare Ag@$BaTiO_3$ composite nanoparticles. A controllable nanolayer of $BaTiO_3$ on the surface of Ag was formed at different Ag/Ba molar ratios. The UV-vis results reveal changes in the optical features of the Ag and Ag@$BaTiO_3$ composite nanoparticles

corresponding to the medium where the nanoparticles are embedded in and the thickness of the $BaTiO_3$ shell. It was found that the ultrathin $BaTiO_3$ shell with a thickness less than 5 nm in composite significantly alters the optical feature and results in almost complete absorption of light in broad spectrum.

The future work will be focused on the preparation of polymer-based nanocomposites homogeneously incorporating our synthesized colloidal core@shell nanoparticles for development of organic photovoltaic devices.

Zusammenfassung

In den letzten Jahren haben Kern@Schale Nanopartikel stark an Bedeutung in Forschung und Entwicklung neuartiger funktionaler Materialien gewonnen, da hier die Möglichkeit besteht, verschiedene Funktionalitäten zu kombinieren und die Eigenschaften durch Zusammensetzung, Dicke des Kerns und der Hülle und Partikelgröße gezielt zu beeinflussen. Als Kern Materialien kommen hierbei unter anderem Halbleiter, Metalle, magnetische Oxide und gekapselte Moleküle zum Einsatz. Die Schale kann den Kern vor Umwelteinflüssen schützen, die Agglomeration vermindern, die Stabilität und Dispergierbarkeit erhöhen, z. B. die kernoberfläche lassen sich funktionalisieren, dadurch wird ein homogenes Einbringen anorganischer Kernpartikel in eine organische Matrix möglich.

$BaTiO_3$ ist ein sehr bekanntes dielektrisches Material und wird als Dielektrikum in Kondensatoren verwendet aufgrund seiner hohen und frequenzunabhängigen relativen Permittivität mit niedriger dielektrischen Verluste. Der Fokus der Arbeit liegt auf der Synthese und Charakterisierung von $BaTiO_3$ Nanopartikeln und die Verwendung von $BaTiO_3$- Nanopartikeln zur Herstellung von verschiedenen Kern@Schale Nanopartikel: $BaTiO_3$@SiO_2 und Ag@$BaTiO_3$.

Für die Herstellung von $BaTiO_3$ Nanopartikeln wird eine umfangreiche, kosteneffiziente und umweltverträgliche “Organosol” Synthese bei niedrigen Temperaturen entwickeln. Diese einfache, schnelle und schonende Synthese bietet viele Möglichkeiten, auf das gewünschte Produkt Einfluss zu nehmen. Hinzu kommt die einfache Skalierbarkeit und die genaue Kontrolle der Partikelgröße.

Des Weiteren wird die Herstellung von $BaTiO_3$@SiO_2 Nanopartikel mit Kern@Schale-Struktur über inverse Mikroemulsion als Reaktionsmedium gezeigt. Die inverse Mikroemulsionslösung (W/O) besteht aus Triton X-100, n-Hexanol, Cyclohexan und einer wässrigen Phase. Bei diesem Verfahren werden aus einem Tetraalkylorthosilicat (TEOS) durch eine Ammoniak-katalysierte Hydrolyse-Kondensationsreaktion in einer inversen Mikroemulsion SiO_2 beschichtete $BaTiO_3$ Nanopartikel, wobei die SiO_2 schale eine Dicke im Bereich von 3 nm bis 20 nm aufweist, erzeugt. Mikrostrukturanalysen, so wie TEM-EDS-Elementverteilungsbilder, zeigen SiO_2 auf der $BaTiO_3$ Nanopartikel-Oberfläche gebildet wird.

Der dritte Teil der Arbeit befasst sich mit der Synthese und Charakterisierung von Ag@$BaTiO_3$ Nanopartikel. Die Herstellung erfolgt in zwei Schritten: (1) Herstellung eines Ag Organo-sols, (2) anschließend Einbringen des hergestellten Ag Organosols in ein $BaTiO_3$ “Organosol” Precursor. UV/Vis-Spektroskopie ermöglicht die Untersuchung der Bildung und Aggregation von Ag und Ag@$BaTiO_3$ Nanopartikel. Die spektrale Lage der Plasmonresonanz wird von mehreren Faktoren beeinflusst, z.B. dem umgebenden Medium, auch der $BaTiO_3$ Schichtdicke. Es zeigt sich eine erhebliche Veränderung der spektralen Lage von Ag@$BaTiO_3$ Nanopartikeln

mit einer ultradünnen Schale von weniger als 5 nm. Es entsteht ein breites spektrum, wenn sie alles auffallende Licht fast vollständig absorbieren.

Die zukünftige Arbeit konzentriert sich auf die angestrebte homogene Einbettung unserer hergestellten Nanopartikeln mit Kern@Schale-Struktur in Polymermatrizes zur Anwendung und Entwicklung zukünftiger organischer Solarzellen.

Contents

List of Figures

List of Tables

Chapter 1

Introduction and Aim of Work

1.1 Research Background and Motivation

Nanoscience and nanotechnology has become a very interesting research branch due to the creation of new nanomaterials with the development of new technologies. In this regard, nanoparticle-based material engineering has risen very much in recent years, because nanoparticles having nanoscale particle sizes exhibt new interesting optical, electrical and magnetic properties, they are completely different from those of bulk materials due to large specific surface area and the quantum confinement effect. Much interest has been concentrated on their applicability in catalytic, ceramic, electronic devices as well as polymer composites and coatings [32].

Ferroelectric nanoparticles, such as lead zirconate-titanate ($Pb[Zr_xTi_{1-x}]O_3$ ($0 \leq x \leq 1$), PZT), barium titanate ($BaTiO_3$, BTO), calcium-copper titanate ($CaCu_3Ti_4O_{12}$, CCTO), sodium niobate ($NaNbO_3$), among others, are key to many modern technologies, in particular piezoelectric actuators and electro-optic modulators due to their high dielectric constant, high dipole moment, and high electromechanical coupling coefficient [33]. Amongst them, lead-free perovskite $BaTiO_3$ is one of the most extensively studied ferroelectric materials, because of its environmentally friendly feature, making it a good substitute for Pb-containing compounds for various applications. Because the nanotechnology industry is growing rapidly today, for extending the range of applications or for improving single phase's properties, the combination with other types of functional materials is currently proposed. Over the last decade, there have been immense efforts to prepare core@shell nanostructured nanoparticles with tailored structural, optical, and surface properties. The purpose of coatings on core-particles is carried out for different reasons like surface modification, increasing functionality, stability, dispersibility, and control release of the core material. The presence of the shell can alter some properties of core like surface charge, functionality, and reactivity. For example, temper-

ature stability of dielectric constant is important for capacitor applications, which is associated with the core@shell structure having a different chemical composition between bulk grain and grain boundary [34, 35]. These microstructures are usually obtained by mixing small amounts of several oxide additive coatings to $BaTiO_3$ powders. There are many kinds of materials available for coating of the $BaTiO_3$ nanoparticles, like metal oxide, noble metals and polymer material. In the field of high-permittivity dielectrics it is highly desirable to have the grains of the ceramic composed of a core of pure $BaTiO_3$ surrounded by a SiO_2 shell, because the resulting SiO_2 coated nanoparticles are chemically stable, fairly biocompatible, nontoxic, and can be prepared in narrow size distribution. Furthermore, SiO_2 coating will lead to an improved sintering behavior of $BaTiO_3$ particles since SiO_2 is known to be a good sintering aid [36, 37]. Moreover, a homogeneous distribution of SiO_2 layer coating on $BaTiO_3$ particle is very important because the inhomogeneous presence of small amounts of liquid phases gives rise to exaggerated grain growth [38] and the segregation of SiO_2 into grain boundaries was found to deteriorate electrical properties [39].

$BaTiO_3$-based dielectric powder is most widely used in the multilayer ceramic capacitor (MLCC) industry. Recently, Wei et al. [1] proposed a method to prepare core@shell structured dielectric particles which consist of a conductive core and one or more thinly coated layers of dielectric material for the application of multilayer ceramic capacitors (MLCC) instead of conventionally solid dielectric $BaTiO_3$ particles as the capacitor's active layers (Figure 1.1). The coated dielectric shell will form thin barrier layers along the conductive particle surface through co-firing. In particular, the use of core@shell particles with a thin shell of high permittivity dielectric material improves the capacitance volumetric efficiency, and the use of core@shell particles with a thick shell of dielectric will improve capacitor device's energy storage capacity as the results of improved electrical and mechanical strength. Figure 1.1 (c) shows the effective dielectric constant of three MLCCs made from $BaTiO_3$, $SrTiO_3$, and PLZT core@shell particles as a function of the shell thickness. However, a shell thickness less than 10 nm may have a low resistivity or cause electrical shorting when the core@shell particles are made into the capacitor devices. In order to make high quality shells with less defects and uniform thickness, chemical coating through reaction such as sol-gel, hydrothermal, co-precipitation methods, or chemical vapor deposition are preferred.

Despite the fact that the main interest with core@shell dielectric particles is more concentrated on MLCC devices, these said particles have a significant influence on other fields of science as well. For example, they can be also used in plasmonic metamaterial absorbers, a booming research field aiming at the manipulation of light at the nanoscale. An ideal perfect absorber is an object that absorbs all light that falls onto it and it is valuable for many important applications, e.g., photodetection or collection of solar energy (photovoltaic cells).

For example, an absorber based on chemically-synthesized Au@SiO_2 core@shell structured dielectric nanparticles was fabricated, as shown in Figure 1.2 [2].

This dissertation work aims to gain a deeper understanding of the core@shell systems, their chemistry, properties and morphology control, as well as to optimize the synthesis methods for the production of $BaTiO_3$-based core@shell nanostructures, meanwhile, investigate the mechanistic processes involved in the formation of the core@shell nanoparticles.

Specifically, emphasis was placed to provide some answers to the following problems:

1. Is it possible to directly produce hydrophobic nanocrystalline $BaTiO_3$ with narrow size distribution and tunable properties?

2. What is the role of the surfactant oleic acid in the synthesis of $BaTiO_3$ nanoparticles? How does a washing process affect the obtained structures?

3. What are the specific effects observed on crystalline phases as well as on particle morphology?

4. How can the presented "organosol" synthetic strategy be expanded to produce a broad range of core@shell structures?

5. Can we use plasmonic nanoparticles to create optical-frequency metamaterials by combining plasmonic nanoparticles with dielectric shells?

The investigation of the above mentioned aspects is compiled in this thesis. Fabrication and characterization of hydrophobic $BaTiO_3$ and its stable core@shell nanostructured particles will be presented. Furthermore, particular attention is given to the "organosol" synthesis process of $BaTiO_3$, to study its influence on the material properties, like the crystallinity of the products, morphology, or crystal structure. Following this, the effects of synthesis parameters, as surfactants, metal precursors or solvents, along with post-treatment procedures on the core@shell structure development will be investigated. A detailed study of the $BaTiO_3$ nanoparticles, their morphology and structure development will be provided during the discussion of the synthetic pathway. Next, the "organosol" synthetic strategy to obtain perfectly shaped, uniformly coated core@shell structure, as well as post-treatment procedures will be introduced. Attempt will be made to produce materials suitable for polymer-based composite photovoltaic fabrication. Finally, possible applications and synthesis extension prospects for the investigated core@shell structure systems will be given.

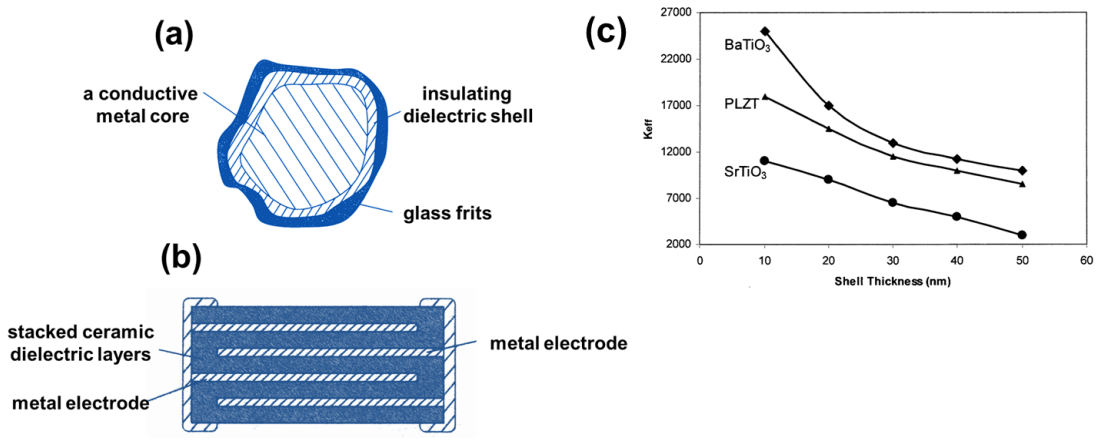

Figure 1.1: shows (a) a core@shell particle cross section with a conductive metal core, a dielectric coated shell, (b) a schematic view of the cross section of a multilayer ceramic capacitor, and (c) shows the effective dielectric constant (K_{eff}) of the capacitors made from $BaTiO_3$, $SrTiO_3$, and PLZT core@shell particles as a function of shell thickness [1].

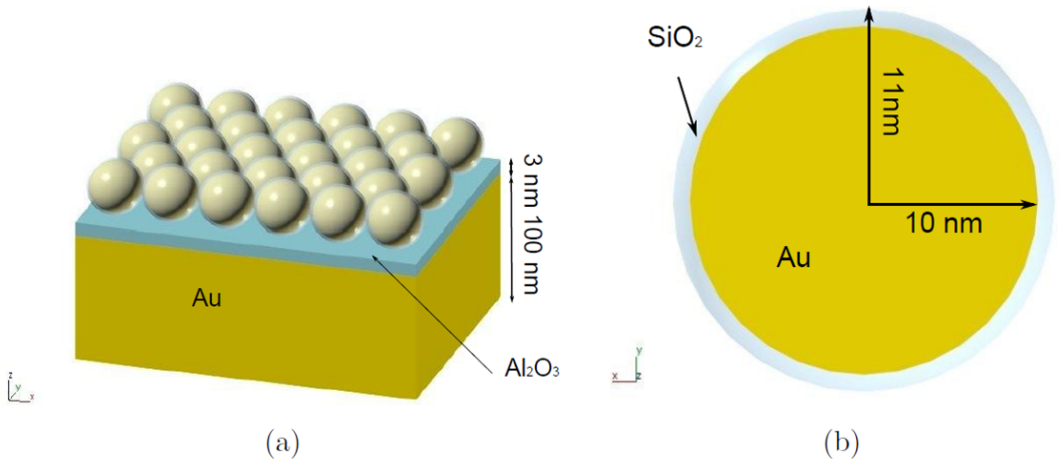

Figure 1.2: (a) Three-dimensional schematic view of Au@SiO_2 core@shell nanoparticles based absorber and (b) The cross section view of the Au@siO_2 nanoparticles [2].

1.2 Thesis Objectives

The overall objective of this thesis is to develop inexpensive, environmental friendly, and easy-to-scale up methods for synthesizing nanosized $BaTiO_3$ and $BaTiO_3$-based core@shell nanostructured particles. The main achievements of the work performed in this study are summarized as follows:

1.2.1 Study of the "organosol" route

"Organosol" is generally understood in a sol in which an organic liquid forms the dispersion medium. The use of organic solvents instead of an aqueous one might be a promising solution to this problem in which the particles gain steric stabilization due to the presence of giant hydrophobic stabilizing ligands. A variety of wet chemical methods have thus far been developed for the nanocrystal synthesis. The main issues are to have control over particle size and size distribution, surface passivation, and crystallinity of the nanocrystal. In a good solvent, the ligands extend from the nanocrystal surface and provide steric stabilization, which typically limits the size of the generated particles in the nanometer range and prevents unwanted agglomeration. To prevent nanosized particles from aggregation, capping ligands have to anchor to the particle surface. We have found that oleic acid is an effective capping ligand in preparing oxide-based nanostructures without any agglomerations, even at elevated processing temperature. Hence, the current "organosol" approach offers an inexpensive, safe and facile synthesis route to produce oxide-based nanomaterials with high yield.

1.2.2 Synthesis of hydrophobic $BaTiO_3$ nanoparticles

An "organosol" route for synthesizing a variety of different perovskite oxides nanoparticles, such as $BaTiO_3$, (Ba,Sr)TiO_3, $SrTiO_3$, $BaZrO_3$, etc. nanoparticles will be explored. The desired nanoparticles should be stable and hydrophobic with the targeted size in the range of ca. 10-15 nm and possess excellent dispersibility in organic solvents. This method offers an alternate low-cost route to perovskite nanopowders easily dispersed in organic media. Indeed, during the preparation of the nanoparticles their stabilization is done using organic molecules, the surfactants. This surface modification of the nanoparticles decreases their surface free energy, and thus reduces their tendency to aggregate. Furthermore, we can change the chemical composition, shape, and size of nanoparticles by inducing small variations in the synthetic process, and therefore, we manage to precisely tailor them according to the desired application. The control over the synthesis of the colloidal nanoparticles gives a great variety of possibilities in terms of properties (optical, thermal, mechanical, electronic, magnetic) that

can be tuned over large ranges. No one has really addressed the key challenge of these robust hydrophobic materials, we expect these hydrophobic ceramics to generate far-reaching technology.

1.2.3 Synthesis of $BaTiO_3$@SiO_2 core@shell nanoparticles

The study of the incorporation of $BaTiO_3$ particles into a silica matrix to obtain hybrid core@shell structures is very important, because of significant changes and/or improvements in the dielectric, electric, and optical properties of the resulting products. TEOS (tetraethyl orthosilicat), an organometallic compound of silicon, as a precursor, through a hydrolysis-condensation reaction. Reverse microemulsion was used in this study for the production of $BaTiO_3$@SiO_2 core@shell nanoparticles. Advantages of this method are that the resulting silica nanoparticles have "smooth" surfaces, display good monodispersity, and that nanoparticles with nonpolar ligands can be directly coated.

1.2.4 Synthesis of Ag@$BaTiO_3$ core@shell nanoparticles

Though the research on stabilization of Ag nanoparticles has grown, studies on the interaction of Ag nanoparticles with polymer organic semiconductors, e.g. P3HT, are still progressing. Nonetheless, reports on Ag@$BaTiO_3$ nanoparticles are far fewer compared to Ag@SiO_2 core@shell nanoparticles, mainly because of the poor wetting properties. In this work, we are developing a novel silver and barium titanate composite nanoparticle Ag@$BaTiO_3$ with tunable optical properties based on the core-shell nanostructure comprising either a Ag core with dielectric $BaTiO_3$ shell or a small amount of Ag cores dispersed in a continuous dielectric $BaTiO_3$shell matrix, which depends on the amount of shell precursor to obtain the desired shell. Further development and extension of current synthetic strategy are being pursued to combine these core@shell nanostructured Ag@$BaTiO_3$ nanoparticles into polymer nanocomposite form. We believe that advanced synthetic techniques and greater stability of $BaTiO_3$ shell-isolated Ag nanoparticles dispersions can result in the significant enhancement of device performance of organic solar cells.

1.3 Thesis Organization

This thesis has been divided into five main chapters, each of which explains in detail the process of research that has been carried out. Chapter 1 motivates the present work further followed by Chapter 2 which offers a brief background information on the three key types of nanoparticles: $BaTiO_3$, SiO_2, and Ag, as well as the corresponding core@shell nanoparticles.

In Chapter 3 we present detailed information about all the characterization techniques that were used to obtain the experimental data in Chapters 4, 5 and 6. In Chapter 4 synthesis of $BaTiO_3$ using the "organosol" route is described as a simple and effective way to prepare perovskite oxides. Chapter 5 is dedicated to the synthesis and characterization of $BaTiO_3$@SiO_2 nanoparticles, where a reverse microemulsion method to synthesize core@shell structures is proposed in detail and a discussion on the shell thickness of SiO_2 in this core@shell structure is given. Chapter 6 is focused on Ag@$BaTiO_3$ core@shell nanoparticles. This modification of Ag nanoparticles with $BaTiO_3$ shell leads to enhance a light absorption due to coupling of the Ag nanoparticles and the dielectric $BaTiO_3$ shell. Finally, Chapter 7 is a summary of the major conclusions that result from the performed work. There are also suggestions for future work on Ag@$BaTiO_3$ /PVDF-TrFE copolymer composite films.

1.4 Peer Reviewed Publications and Conference Proceedings

1.4.1 Conference Proceedings

Y. Gao and Doru C. Lupascu, "Synthesis and Characterization of $BaTiO_3$ Nanopowders and $BaTiO_3$/$CoFe_2O_4$ Nanocomposites," ***Mater. Res. Soc. Symp. Proc.*** Vol. 1397 (2012).

M. Etier, Y. Gao, V. V. Shvartsman, D. C. Lupascu, J. Landers, and H. Wende, "Magnetoelectric properties of 0.2$CoFe_2O_4$-0.8$BaTiO_3$ composite prepared by organic method," Proceedings of 2012 21st IEEE Int. Symp. on Applications of Ferroelectrics held jointly with 11th IEEE European Conference on the Applications of Polar Dielectrics and IEEE PFM, ISAF/ECAPD/PFM, Article number 6297820 (2012).

1.4.2 Publications

M. Etier, C. Schmitz-Antoniak, S. Salamon, H. Trivedi, Y. Gao, A. Nazrabi, J. Landers, D. Gautam, M. Winterer, D. Schmitz, H. Wende, V. V. Shvartsman, and D. C. Lupascu, "Magnetoelectric coupling on multiferroic cobalt ferrite-barium titanate ceramic composites with different connectivity schemes," ***Acta Materialia 90***, 1-9 (2015).

Y. Gao, V. V. Shvartsman, D. Gautam, M. Winterer, and D. C. Lupascu, "Nanocrystalline barium strontium titanate ceramics synthesized via the "organosol" route and Spark Plasma Sintering," ***J. Am. Ceram. Soc.*** **97**, 2139-2146 (2014).

M. Etier, V. V. Shvartsman, Y. Gao, J. Landers, H. Wende, and D. C. Lupascu, "Magnetoelectric effect in (0–3) $CoFe_2O_4$-$BaTiO_3$(20/80) composite ceramics prepared by the organosol

route," ***Ferroelectrics*** **448**, 77-85 (2013).

M. Escobar Castillo, V. V. Shvartsman, D. Gobeljic, Y. Gao, J. Landers, H. Wende, and D. C. Lupascu, "Effect of particle size on ferroelectric and magnetic properties of $BiFeO_3$ nanopowders," ***Nanotechnology*** **24**, 355701 (2013).

Y. Gao, A. Elsukova, D.C. Lupascu, "Preparation of SiO_2 Encapsulated $BaTiO_3$ Nanoparticles with Tunable Shell Thickness by Reverse Microemulsion," ***Particle and Particle Systems Characterization*** **30** (10), 832–836 (2013).

Y. Gao, V. V. Shvartsman, A. Elsukova, and D. C. Lupascu, "Low-temperature synthesis of crystalline $BaTiO_3$ nanoparticles by one-step "organosol"-precipitation," ***J. Mater. Chem.*** **22**, 17573-17583 (2012).

M. Etier, Y. Gao, V. V. Shvartsman, A. Elsukova, J. Landers, H. Wende, and D. C. Lupascu, "Cobalt ferrite/barium titanate core/shell nanoparticles," ***Ferroelectrics*** **438**, 115-122 (2012).

1.4.3 Work in Progress

Y. Gao, N. Gharbi, S. Kugai, A. Elsukova, and Doru C. Lupascu, "Core-shell Ag@$BaTiO_3$ Plasmonic Absorber Systems Synthesized via the "Organosol" Route, " work in progress.

Y. Gao, I. Anusca, H. Trivedi, S. Salamon, A. Elsukova, Doru C. Lupascu, "$BaTiO_3$-$CoFe_2O_4$ bi-phasic Janus/Zebra-type nanocomposites based on organosol route," work in progress.

1.5 Important Outcome of the Research

The following section details the important outcomes obtained while carrying out this research.

1. Oleate-modified $BaTiO_3$ nanoparticles have been prepared by the "organosol" route as main part of this work (§ Chapter 4.2).

2. To our knowledge, the SiO_2 ultrathin shells (~3 nm) coated $BaTiO_3$ were firstly experimentally synthesized using a reverse microemulsion method (§ Chapter 5.2).

3. The relative permittivity (ε_r) in nanocomposites is dependent on interfacial polarization and space charge polarization, therefore, it is highly probable that the $BaTiO_3$ coated Ag nanoparticles might exhibit high dielectric constant with low dielectric loss. By carrying out dielectric measurements to core@shell Ag@$BaTiO_3$ nanoparticles the relative permittivity (ε_r) of the Ag@$BaTiO_3$ nanoparticles increased prominently (§ Chapter 6).

4. UV-vis spectroscopic studies revealed the optical properties of Ag@$BaTiO_3$ core@shell nanostructures can be tuned by adjusting the concentration of Ag nanoparticles in $BaTiO_3$ matrix and thickness of $BaTiO_3$ layer. Most remarkably, the Ag nanoparticles coated by an ultrathin dielectric $BaTiO_3$ shell with a thickness less than 5 nm absorbs almost all light that falls onto it compared to pure Ag (§ Chapter 6). This excellent property has motivated us to study Ag nanoparticles embedded in a dielectric $BaTiO_3$ matrix with the aim to design a perfect absorber (plasmonic blackbody), which can be profitably used for the plasmonic enhancement of thin film solar cells through increased optical absorption.

Chapter 2

Nanoparticle Literature Review

Nanoparticles are defined as small particles sized between 1 to 100 nanometers in at least one dimension. Currently, there are more than 1.600 nanotechnology-based consumer products according to an analysis by Nanotechproject.com [40]. Compared to their counterparts in bulk states, manufactured nanomaterials have the merits of better adjustable electronic properties, better tunable optical properties, and higher reactivity. In the following sections, I will focus on three different nanoparticles: barium titanate ($BaTiO_3$), silicon dioxide (SiO_2), and silver (Ag) that have been widely studied both theoretically and experimentally.

2.1 $BaTiO_3$ Nanoparticles

$BaTiO_3$ is a ferroelectric and piezoelectric material which has a variety of commercial applications, including multilayer ceramic capacitors (MLCCs), embedded capacitance in printed circuit boards, underwater transducers (sonars), and thermistors with positive temperature coefficient of resistivity (PTCR).

2.1.1 Structure and Dielectric Property of $BaTiO_3$

$BaTiO_3$ has a typical perovskite structure, which is shown in Figure 2.1. Perovskite materials, with a general stoichiometry of ABO_3, represent a unique class of crystalline solids that demonstrate a variety of interesting dielectric, piezoelectric, ferroelectric, and electro-optic properties. The unique properties of perovskite materials are the result of the crystal structure, phase transitions as a function of temperature, and the size of the ions present in the unit cell.

Above its Curie point (about 130 °C), the unit cell of $BaTiO_3$ is cubic as shown in Figure 2.2 [4]. The barium (Ba) ions reside at the corners of the cubic forming a closepacked structure along with the oxygen (O) ions, which occupy the face centers of the cubic. Each Ba ion is

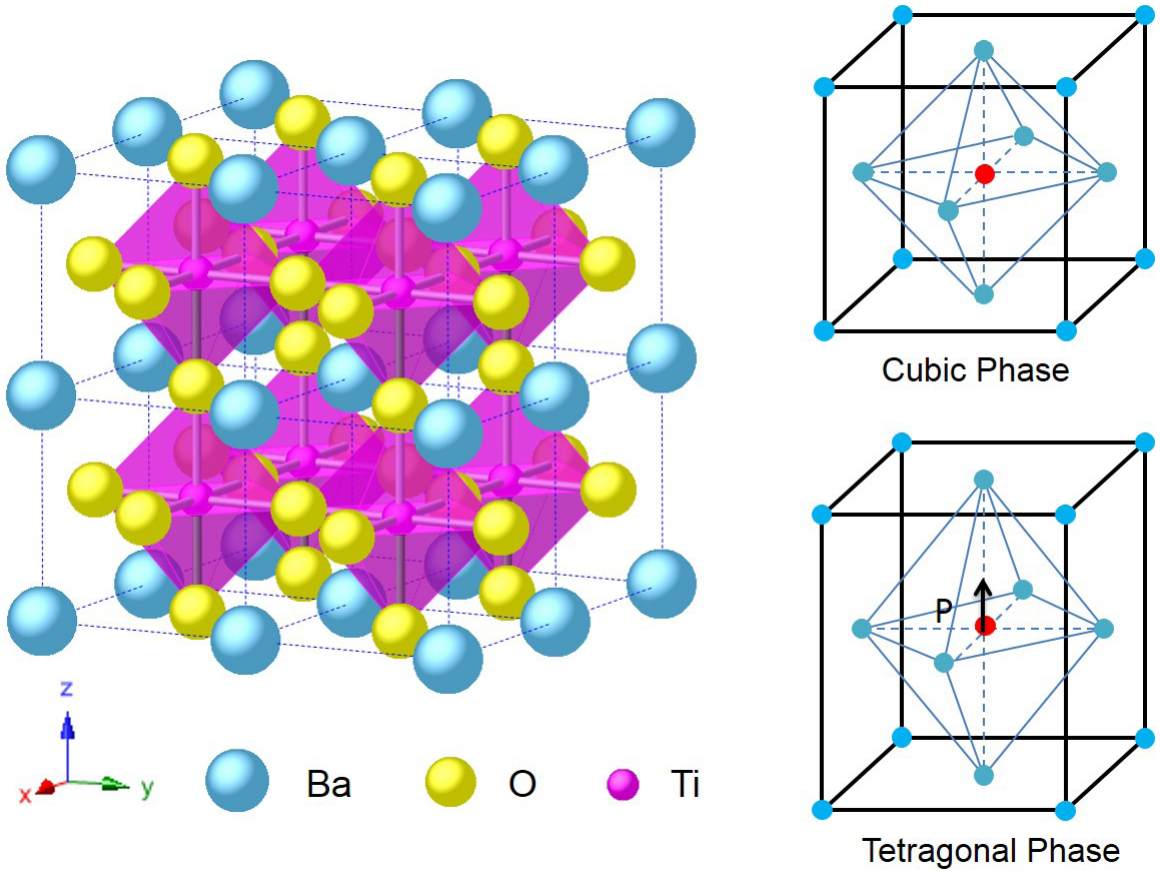

Figure 2.1: Schematic diagram of perovskite $BaTiO_3$ crystallographic structure and its phases [3].

surrounded by twelve O ions, and each O ion is surrounded by four Ba ions and eight O ions. In the center of the face-centered cubic unit cell, the small highly charged titanium (Ti^{4+}) ion is octahedrally coordinated by six oxygen ions.

The crystal structure and dielectric characteristics of $BaTiO_3$ strongly depend on temperature. When the temperature is below the Curie temperature, the cubic structure is slightly distorted to a ferroelectric tetragonal structure having a dipole moment along the c direction [4, 41]. When the temperature goes down below 0 °C, the tetragonal structure will transform to an orthorhombic ferroelectric phase with the polar axis parallel to a face diagonal. When the temperature is reduced further to -80 °C, it will transform to a rhombohedral structure with the polar axis along a body diagonal. All of the phase transformations of $BaTiO_3$ single crystals are illustrated in Figure 2.2. The temperature dependence of the relative permittivity of $BaTiO_3$ measured in the a and c directions is shown in Figure 2.3.

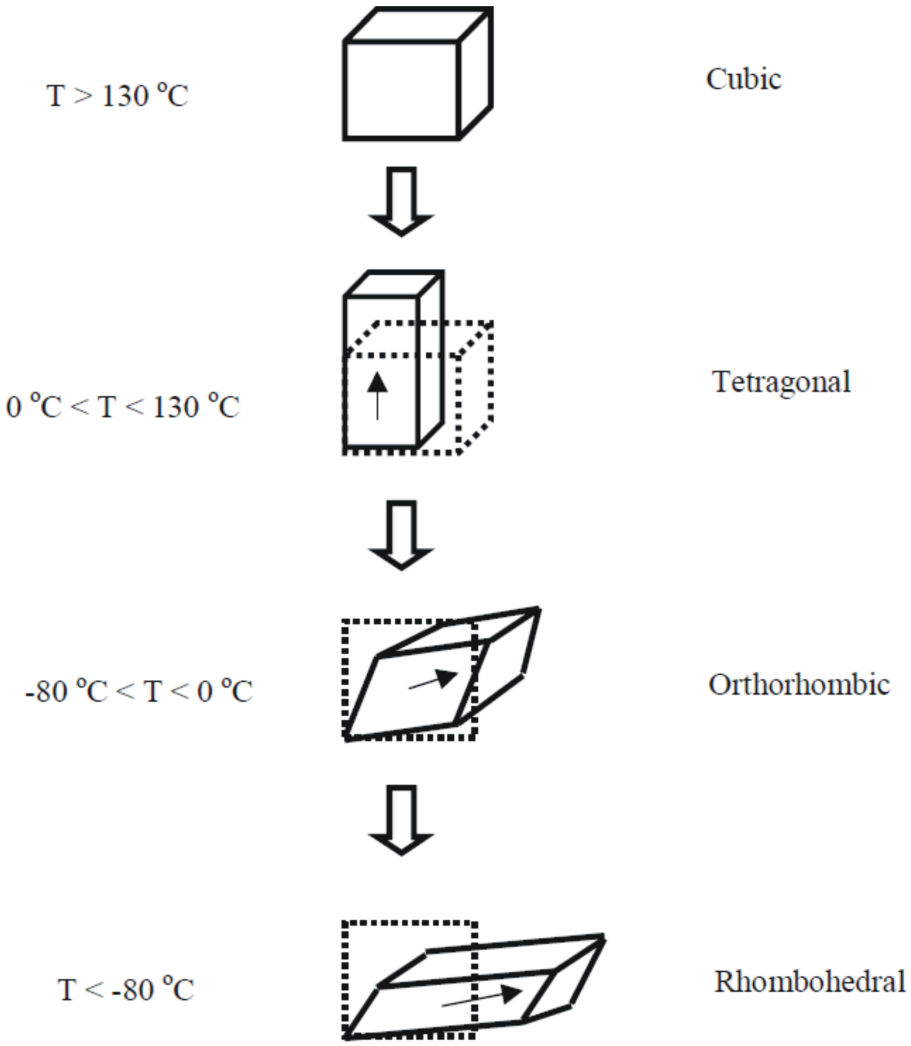

Figure 2.2: Phase transformations of the $BaTiO_3$ crystal at different temperatures [4].

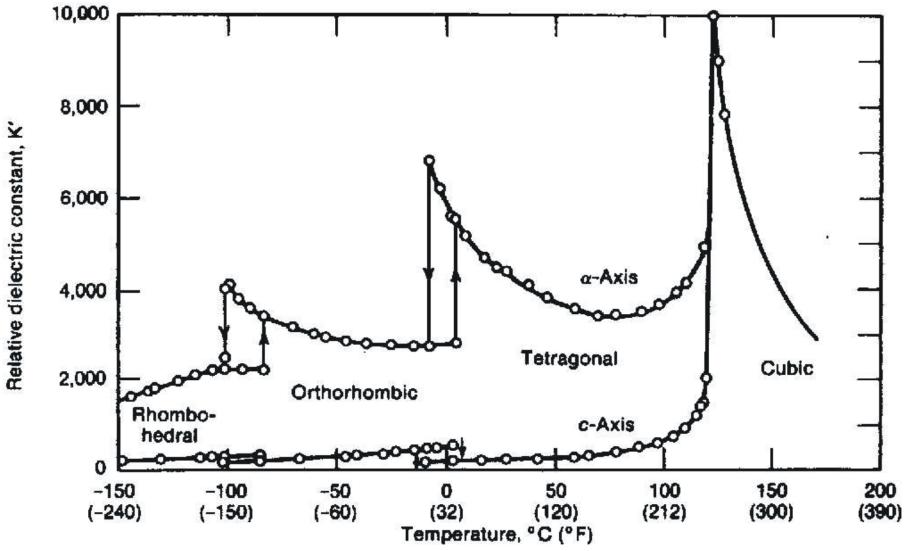

Figure 2.3: Temperature dependence of relative permittivity of $BaTiO_3$ single crystal [4].

2.1.2 Synthesis of $BaTiO_3$ Nanoparticles

Several different synthesis routes have been developed to manufacture nanoscale $BaTiO_3$ powders, which can be mainly performed in two ways: (1) mixed oxide (solid state) preparation. (2) wet - chemical preparation method, so called because of the use of a solvent. To understand the advantages and disadvantages of each route, a review of the common methods is presented. Recent reviews by Adair, Suvaci and Pithan et al. [42] provide good overviews of the different synthesis routes. The general description of some processes widely used for the preparation of $BaTiO_3$ nanopowders is mentioned below. Pathways for $BaTiO_3$ preparation from different precursors are schematically shown in Figure 2.4. One of the main disadvantages of several of the routes is the necessary high-temperature calcination step which leads to the formation of hard agglomerates. Table 2.1 is a list of the most common synthesis routes used to produce nanoscale $BaTiO_3$ powders and their characteristics.

Solid-state synthesis is one of the traditional methods for the synthesis of $BaTiO_3$ powder through heating $BaCO_3$ and TiO_2 to temperatures as high as 1100-1200 °C [5, 43, 44]. This method, however, leads to large $BaTiO_3$ particles (usually above 1 μm) with wide grain-size distribution, irregular morphologies and impurities, which may result in poor electrical properties and difficult reproducibility of sintered ceramics. To obtain finer $BaTiO_3$ powders with high quality, many synthesizing methods have been developed. Among those methods, sol-gel [45–47] and hydrothermal synthesis [48–51] are the most widely used methods for nanocrystalline $BaTiO_3$ synthesis.

In the sol-gel process, $BaTiO_3$ gels can be obtained by hydrolyzing the metal alkoxide with the addition of water. After gelation, the gels are dried and calcined at high temperatures to remove the chemically bound water and crystallize the amorphous gel. The most advantageous characteristics of this method are the high purity and the excellent control of the composition of the resulting powders. The calcination temperature is lower than that of solid-state routes, and therefore agglomerates formed are weaker and easier to break up during milling. However, the expensive raw materials and the low yield rate are the main hindrances for the commercial application of this method. In contrast to this, hydrothermal synthesis can lower the processing temperature, where aqueous solutions of barium and titanium sources are mixed and sealed in a high temperature-pressure reaction vessel and heated (e.g., below 300 °C). During the hydrothermal formation of $BaTiO_3$, a basic environment is necessary for $BaTiO_3$ to precipitate, and that pH is dependent on the Ba concentration in the starting solution. Cheaper starting precursors are frequently used, such as barium hydroxide or barium chloride and titanium oxide or titanium chloride. This process produces fine $BaTiO_3$ powders (< 300 nm) with narrow size distribution, high crystallinity, and high purity. However, the high solution pH during synthesis also leads to the incorporation of large amounts of hydroxide defects into the lattice. After synthesis the powder is washed with an acetic acid solution to remove $BaCO_3$. The acid wash leads to Ba dissolution from the particle and a Ba deficient surface.

Recently, several research groups have focused on the direct wet-chemical synthesis routes based on precipitation of $BaTiO_3$ in aqueous or mixed organic-aqueous media at lower temperatures (< 150 °C) and ambient pressure. Whether the technique is called low temperature aqueous synthesis (LTAS) [52], low temperature direct synthesis (LTDS) [53], or solvent refluxing [54], the basic synthesis steps are similar. Comparing with the hydrothermal method, they do not require an autoclave, and the synthesis process is conducted in water-based solvent or in a mixed solvent of alcohol and water under mild conditions.

In conclusion, for the synthesis of $BaTiO_3$, there is a number of challenges that must be addressed for such an approach to be advantageous from a manufacturing standpoint. The ideal synthesis would [55]:

1. Facilitate low-temperature crystallization of $BaTiO_3$ (at or near room temperature)
2. Maintain phase-pure stoichiometric ratios of Ba:Ti
3. Allow accurate control over grain or particle size at the nanoscale
4. Allow selective crystallization of the tetragonal (ferroelectric) phase over the cubic (paraelectric) phase
5. Allow the formation of monodisperse colloidal nanoparticles
6. Be easily scaled-up to produce quantities appropriate for manufacturing purposes.

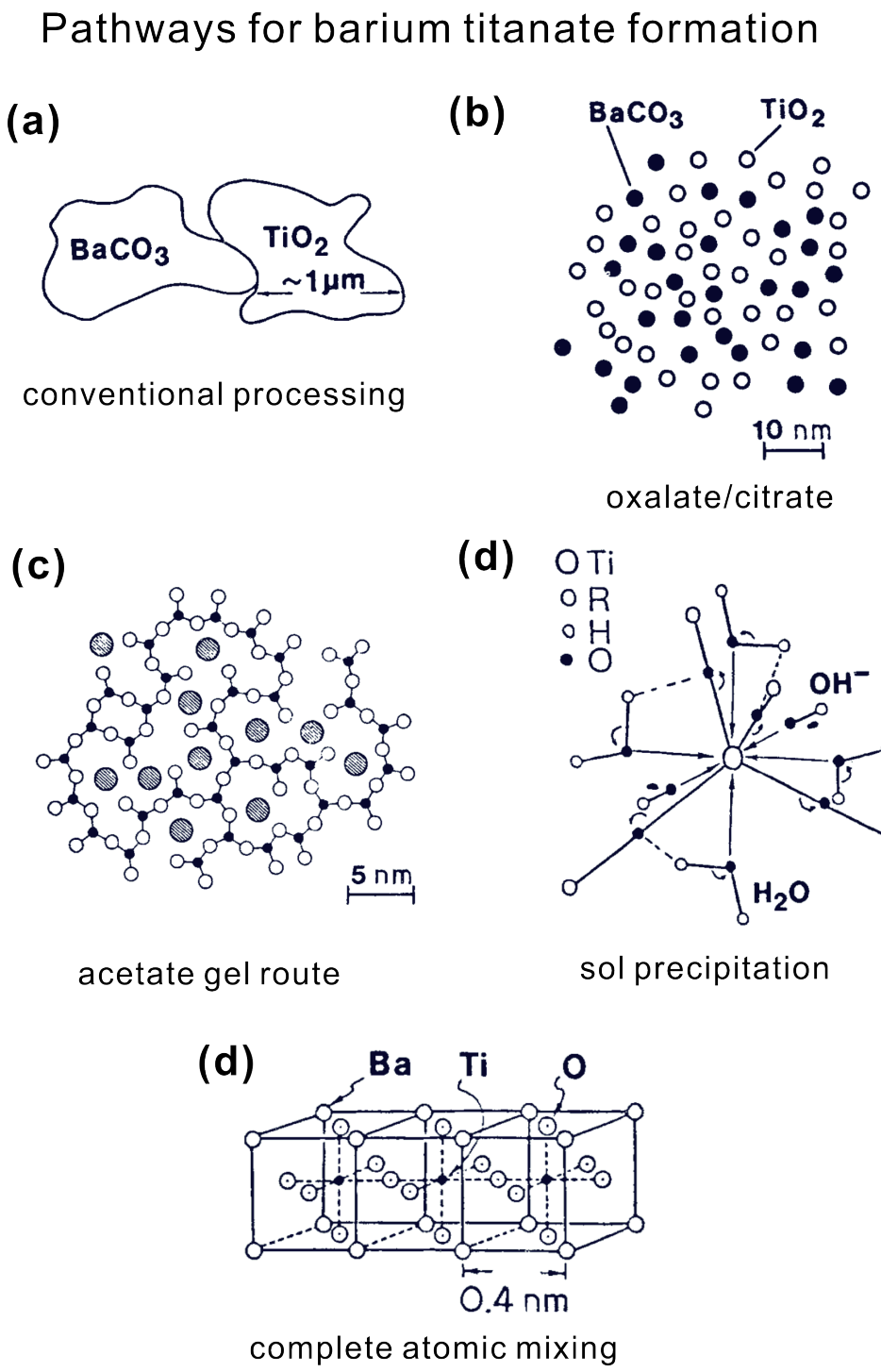

Figure 2.4: Pathways for evolution of crystalline $BaTiO_3$ from different precursors. (a) conventional processing; (b) oxalate/citrate; (c) acetate gel route; (d) sol precipitation; (e) complete atomic mixing [5].

Method	Particle Size	Impurities	Advantages	Disadvantages
Mixed Oxide	400nm to 100's µm	Large quantities of impurities due to starting materials and milling method.	• Easy process to perform on a large scale. • Relatively cheap starting materials	•High impurity levels • High calcination temperatures • Large amounts of aggregation leading to large particle sizes. • Milling usually required. • Poor stoichiometric control from particle to particle.
Coprecipitation	10 nm – 10's µm	Chloride and other impurities present from starting materials. Contamination if milling is required.	• Low impurity levels. • Low reaction temperatures. • Stoichiometric mixing approaches atomic level.	• Usually requires a milling treatment to obtain desired particle size. • More time consuming than mixed oxide method. • Tedious washing required to remove chloride ions.
Sol-Gel	5-100 nm	Minimal contaminants from organic precursors. Small amounts of Si contamination from glassware.	• Very low impurity levels. • Stoichiometric on the atomic level. • Low processing temperatures (20-650°C).	• Relatively expensive starting materials. • Low temperature methods are generally time consuming with low product yield.
Vapor Phase	20 nm - micron level	Small levels of contamination from starting materials.	• Low processing temperatures (100-~800°C). • Easy to produce nanosized particles.	• Some precursor materials are costly. • Collection without aggregation is difficult. • Stoichiometry control can be difficult.
Hydrothermal	3 nm –micron level	Small levels of contamination from starting materials and reaction vessel. Hydrothermal (OH) defects due to aqueous synthesis	• Low processing temperatures (60-500°C). • Particles are formed in solution giving potential control over agglomeration. • High purity and atomic scale stoichiometry. • Particle morphology easily controlled.	• Some precursor materials are costly. • Recovery from suspensions without agglomeration. • Redispersion of agglomerates.

Table 2.1: List of common techniques and their characteristics used in the synthesis of nanoscale $BaTiO_3$. Taken from Adair and Suvaci [31].

2.1.3 Surface Chemistry and Dispersion of $BaTiO_3$

The dispersion of $BaTiO_3$ powders in either an aqueous or a nonaqueous medium has received great attention [56–66]. This is particularly critical in dispersing nanopowders, i.e., particle sizes < 100 nm, in liquid media for nanoceramic fabrication and microprocessing, for example, in order to attain the interesting properties of nanocomposites, it is extremely important to be able to homogeneously disperse the nanoparticles in polymer matrices. In general, the dispersion of nanoparticles in a liquid consists of three stages: (a) wetting of the powder, (b) disintegration of large agglomerates into smaller aggregates of primary particles and (c) stabilization of the powder against reagglomeration [67]. However, a complicated surface chemistry of $BaTiO_3$ and the resultant interactions in liquid media lead to a myriad of problems. $BaTiO_3$ is not thermodynamically stable in water, causing dissolution of Ba^{2+} ions [63, 68–70] and leaving a TiO_2-rich surface (See Eq. 2.1).

$$BaTiO_{3(s)} + 2H^{+} \rightarrow Ba^{2} + TiO_{2(s)} + H_2O \tag{2.1}$$

In the past decade, finding suitable dispersants and binder systems for the aqueous processing of $BaTiO_3$ to limit particle aggregation and dissolution during nucleation and growth has been of interest [62, 71]. Many studies focusing on the $BaTiO_3$ dispersion in non-aqueous media have also been reported [58, 72]. S. Bhattacharjee et al. used polyvinyl butyral (PVB) that can act both as a binder and as a dispersant to attach and stabilize the basic $BaTiO_3$ particle surface in a toluene-methanol solvent system giving rise to a dense coating on the particle and thus imparting steric stabilization [67]. Recently, striving to improve $BaTiO_3$ dispersions in polymer matrices, surface modification of $BaTiO_3$ has been achieved by oleic acid by surfactant adsorption [73, 74] or polymer coatings [75]. Shinn-Jen Chang et al. treated $BaTiO_3$ nanoparticles with hydrogen peroxide (H_2O_2) to produce -OH groups on the surfaces of the nanoparticles, then the hydroxylated $BaTiO_3$nanoparticles were chemically modified with sodium oleate (SOA), $CH_3(CH_2)_7CH{=}CH(CH_2)_7COONa$, as shown in Figure 2.5.

2.2 SiO_2 Nanoparticles

SiO_2 is an important inorganic material useful in a variety of insulation, protection, and diffusion barrier applications. They are considered as the mainstay-building unit in designing and developing nanostructures for a large variety of applications. A simple flowchart for applications of SiO_2 is shown in Figure 2.6. Furthermore, it is suitable for the coating of nanoparticles made from both organic and inorganic materials, because it is highly stable against degradation.

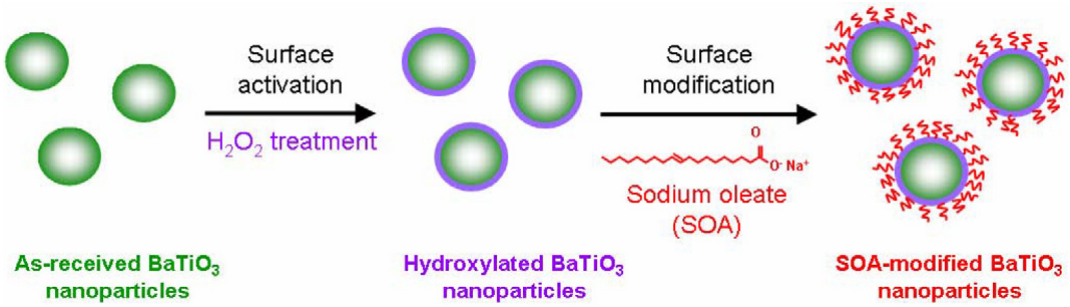

Figure 2.5: The processes for hydroxylation and surface modification of $BaTiO_3$ nanoparticles [6].

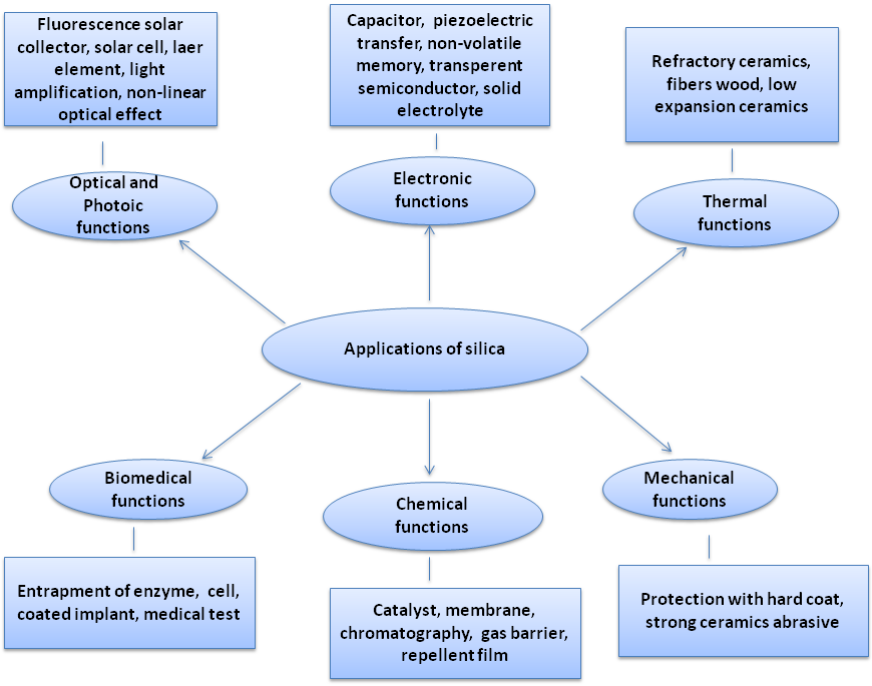

Figure 2.6: Applications of SiO_2 according to S. Sakka [7].

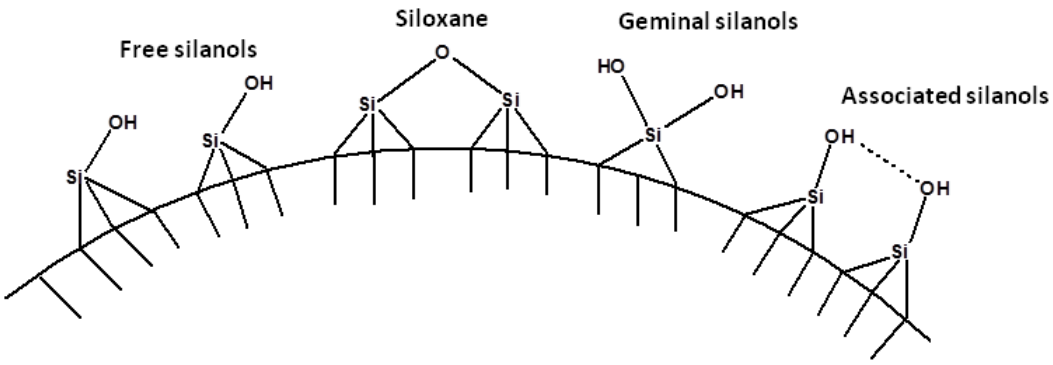

Figure 2.7: SiO_2 particle showing various silanol groups [8].

2.2.1 Colloidal SiO_2

Silica is the common name for silicon dioxide (SiO_2), one of the most abundant component on the earth‘s crust except carbon which occurs in crystalline and amorphous forms (non-crystalline). Colloidal SiO_2 is often used to refer to concentrated dispersions and stable dispersions or "sols" made of discrete and dense amorphous SiO_2 nanoparticles in a liquid. If the liquid is organic, it is called an organosol but, the most commonly used is water and then it is referred to as an aquasol or hydrosol [8]. The particles of amorphous SiO_2 are built up by a random packing of $[SiO_4]^{4-}$ units. This results in a non-periodic structure with the general molecular formula SiO_2 [8]. The bulk structure terminates at the surface in two different ways; oxygen on the surface through siloxane groups (≡Si-O-Si≡) or silanol groups (≡Si-OH). Different forms of silanols are presented in Figure 2.7. A SiO_2 sol is said to be stable if the particles do not settle and do not aggregate at a significant rate. An aggregate in colloidal science is a group of particles held together in any possible way. The term aggregate is used to describe the structure formed by the cohesion of colloidal particles. SiO_2 sols lose their stability by aggregation of colloidal particles. Colloidal SiO_2 particles can be linked together or aggregate by gelation, coagulation, flocculation and coacervation [8].

2.2.2 Synthesis of SiO_2 Nanoparticles

For the time being, the Stöber method as well as the microemulsion method are the prevailing choices for synthesis of SiO_2 nanoparticles (Figure 2.8) [9]. Both methods are based on the polymerisation of tetraethylorthosilane (TEOS) under basic conditions.

The Stöber synthesis developed in the 1960’s was the first method reported for making highly spherical, highly monodisperse SiO_2 nanoparticles with diameters ranging from 50 nm

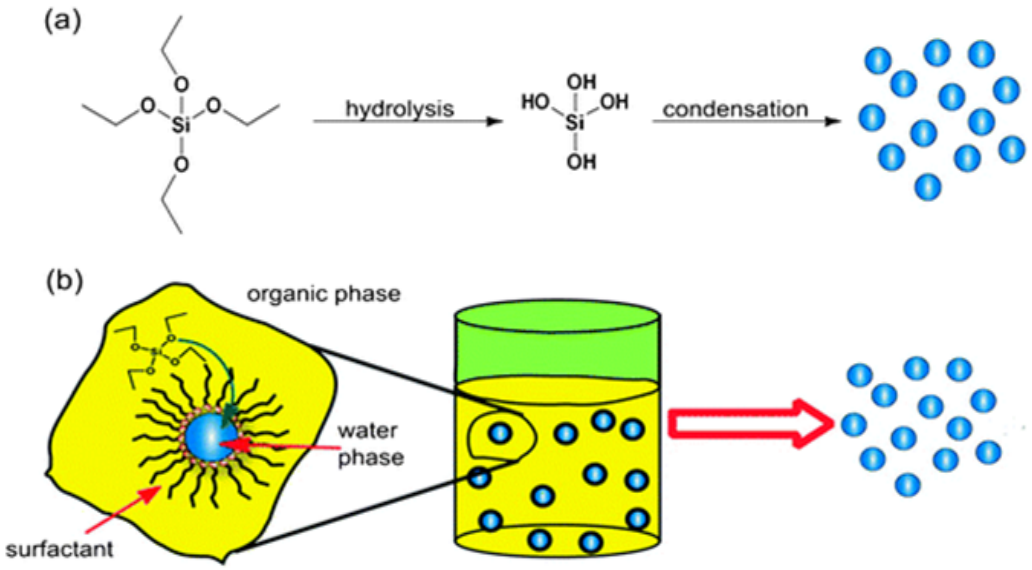

Figure 2.8: Methods for synthesizing solid silica nanoparticles. (a) The Stöber method, in which the hydrolysis and condensation of TEOS is facilitated by base in ethanol/water. (b) The reverse phase microemulsion, in which TEOS is hydrolyzed at the micellar interface and enters the aqueous droplet to form a silica nanoparticle within the micelle [9].

to 2 μm [76]. In a typical Stöber procedure (Figure 2.9), ethanol, ammonium hydroxide, and water are mixed together, and then TEOS is introduced into the mixture with stirring. TEOS is hydrolyzed catalyzed by ammonium hydroxide and then the silicic acid produced by the hydrolysis of TEOS condenses to form amorphous spherical SiO_2 particles. The diameter of the SiO_2 particles from the Stöber process is controlled by the relative contribution from nucleation and growth processes. The resulting spherical units are the nuclei that develop into larger particles by Ostwald ripening [77]. At pH = 7-10, the SiO_2 nanoparticles are negatively charged and repel each other. Therefore, the particles can continue to grow without aggregation. Above pH 10, the SiO_2 begins to dissolve as Silicate. At low pH, the SiO_2 particles bear very little ionic charge. Thus, the particles can collide and aggregate into chains and then form gel networks. This also happens when salts are present at high pH, because the salts can neutralize the SiO_2 [78] (Figure 2.10). Generally, the Stöber process yields monodisperse coated particles with an evenly distributed shell thickness. Nevertheless, the formation of pure SiO_2 particles besides the coating of the nanoparticles is always a side effect in the coating process. Therefore, it is crucial to control the concentrations of both TEOS precursor and ammonia catalyst to suppress the development of secondary nuclei. The Stöber SiO_2 particles are very hydrophilic.

The second synthesis route to prepare SiO_2 is the reverse-micelle or water-in-oil (w/o) microemulsion process [79–82]. Unlike traditional macroemulsion, a microemulsion is a ther-

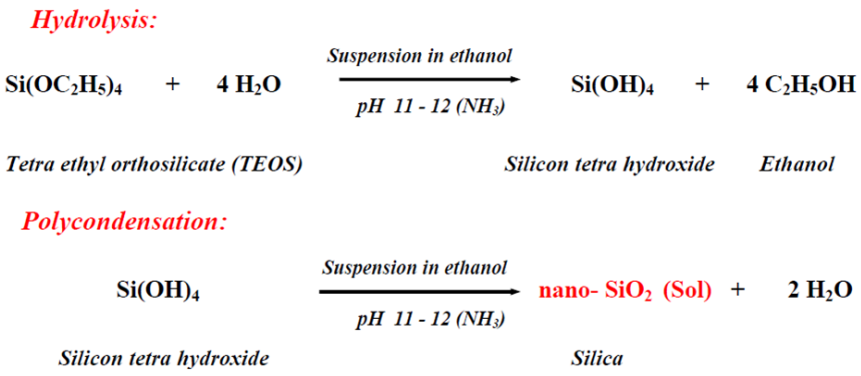

Figure 2.9: Synthesis of Stöber spherical SiO_2 particles: hydrolysis and condensation of TEOS.

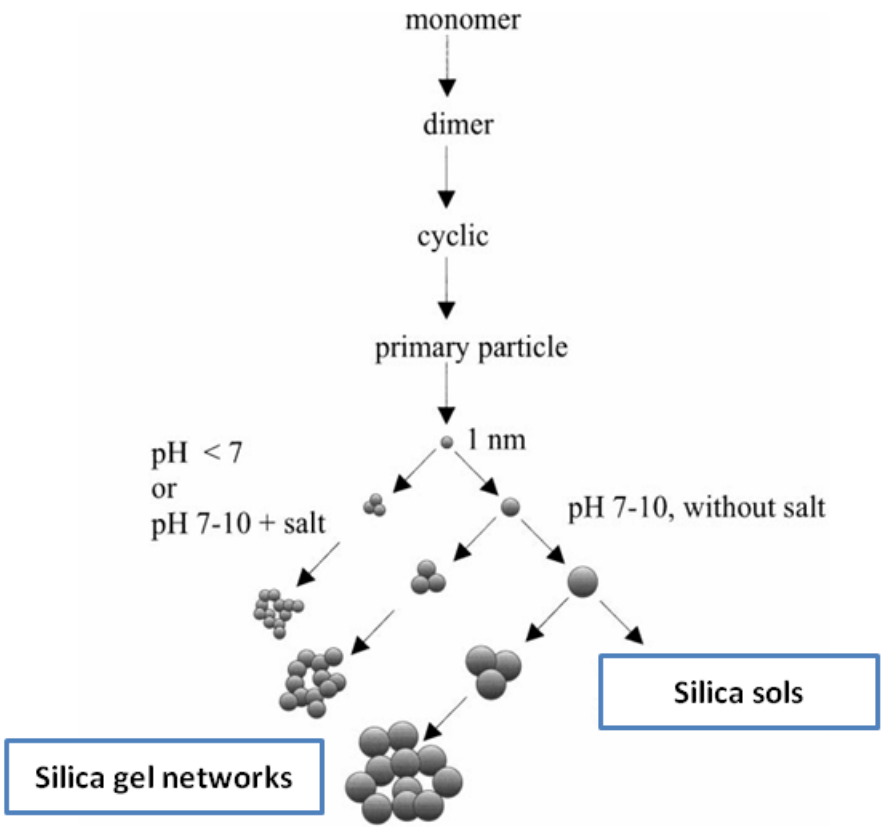

Figure 2.10: Polymerization behavior of SiO_2 (modified and redrawn from Iler [10]).

modynamically stable dispersion of two immiscible liquids, where the microdomain of either or both liquids is stabilized by an interfacial film of surfactant and sometimes cosurfactant which was first reported in 1943 by Hoar and Schulman [83, 84]. The microemulsion method has many advantages such as simplicity of operation, facile control of the properties of the hybrid nanoparticles by experimental conditions including the number and size of encapsulated nanocrystals, the core size and shell thickness. For example, TEOS is used as precursor for SiO_2 particle formation and ammonium hydroxide as catalyst analogously to the Stöber method. The polar ammonium hydroxide is located in the water phase, whereas TEOS is partitioned between the aqueous and organic phases. Diffusion of the TEOS into the micelles, which act as "nanoreactors", promotes the coating reaction. The surfactants also act as capping agents preventing the flocculation of the products.

The surfactant-covered water pools offer a unique environment for formation of nanoparticles of tailored size and shape. The molar ratio of water to surfactant (S), w_0 :

$$w_0 = \frac{[H_2O]}{[S]} \tag{2.2}$$

yield the relationship between w_0 and the micellar radius r_m:

$$r_m = \frac{3V_s}{\Sigma_s} + \frac{3V_w w_0}{\Sigma_s} \tag{2.3}$$

where, Σ_s is the molar interfacial area at the surfactant-oil boundary; V_s, V_w are the molar volume of surfactant and water respectively [84].

Ideal reaction conditions have to be specifically adjusted to the type and size of the nanoparticles. Furthermore, the formed nanoparticles have to be precipitated and centrifuged to isolate them. The nanoparticles cannot be kept in a colloidal state to minimize aggregation effects. Moreover, it is virtually impossible to completely remove the surfactant molecules by washing. Typically, the microemulsion process is applied to nanoparticles with a hydrophobic surface [85], whereas the Stöber method can be used for both hydrophilic and hydrophobic nanoparticles.

2.3 Ag Nanoparticles

Ag nanoparticles are important materials that have been studied extensively [86–90]. The ever-increasing attention and study of Ag nanoparticles is due to their widespread applications in the areas of solar technology, medicine, textiles, electronics, and green technology. Ag nanoparticle properties such as strong light scattering and little absorption are being exploited for light harvesting by their incorporation into the photoactive layer of photovoltaic

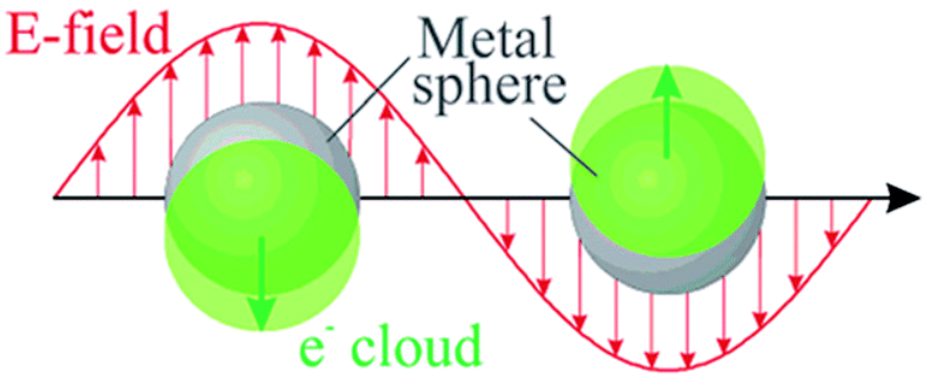

Figure 2.11: Schematic of plasmon oscillation for a sphere, showing the displacement of the conduction electron charge cloud relative to the nucleus. Reprinted with permission from ref. [11]. Copyright 2003, American Chemical Society.

cells thereby reducing surface reflectance [91].

2.3.1 Electro-optical properties of Ag Nanoparticles

The unique optical properties of Ag nanoparticles arise from their surface plasmon resonance (SPR) when interacting with light of various wavelengths in the visible range. An exact analytical, theoretical description of SPR of spherical metal nanoparticles is part of Mie's theory for scattering and absorption of light by spheres [92, 93]. Surface plasmons are the waves that propagate along the surface of the metal. When the wave vector of incident light is the same as that of oscillation of plasmons, these plasmons oscillate in resonance with the light. This resonant interaction between the SPs and the electromagnetic field of incident light leads to the phenomenon called SPR as illustrated in Figure 2.11.

Ag colloids have been extensively characterised by UV-Vis spectroscopy because they exhibit an intense absorption band in this region, known as the surface plasmon absorption band (SPAB), which is a product of the colloid's nanoparticles physical properties, including their size, shape, surrounding dielectric medium, coupling of the colloids and adsorbed solutes [11]. In principle, almost any color of the Ag colloidal solution in any part of the visible spectrum can be produced with changes in the nanoparticles size and shape. For example, Figure 2.12 shows the spectra of both the Ag seed colloid and the colloids of Ag larger particles grown from the seed. For smaller particle size, the colloidal Ag appears yellow, a narrower/sharper absorbance band is observed, while the larger particles appear blue with a wider broader peak.

With respect to Mie's explanation, metal nanospheres with particle size ($2R$) smaller than the wavelength of light λ have an extinction coefficient k_{ex} (absorption and scattering) given

by the following equation (Eq. 2.4) [92].

$$k_{ex} = \frac{24\pi^2 R^3 \varepsilon_h^{3/2}}{\lambda} \frac{\varepsilon_2}{[\varepsilon_1 + 2\varepsilon_h]^2 + \varepsilon_2^2} \tag{2.4}$$

In the equation, the wavelength of light is λ, and the dielectric constant of the surrounding medium is ε_h where the terms ε_1 and ε_2 reveal the real and the imaginary parts of the dielectric constant of the metal, ε_m, ($\varepsilon_m = \varepsilon_1 + \varepsilon_2$). If the imaginary part of the dielectric constant of the metal (ε_2) is small, the resonance condition which results in the absorption maximum is produced ($\varepsilon_1 = -2\varepsilon_h$). The dielectric constant of the metal ε_m is affected by the change in the size of nanoparticles which results in the change of the surface plasmon resonance which is generally explained as the intrinsic size effect [94].

According to Eq. 2.4 given above, the appearance and the region of the plasmon absorption band also is related to the dielectric constant ε_h of the surrounding medium. A dielectric shell on a metal nanoparticle can change the local environment. For example, a metal nanoparticle in water (n≈1.33), the presence of a silica shell (n≈1.5) will result in a weak red-shift in the plasmonic response. However, the resonance of a metal nanoparticle embedded in a matrix layer with a large index of refraction, n, (for example, a microcrystalline silicon medium with n≈4), will strongly red-shift, while a silica shell on a metal nanoparticle embedded in the same medium has a very strong blue-shift effect on the plasmon resonance, as shown in Figure 2.13. Based on the Mie theory for a single spherical particle, Bala Krishna Juluri and co-works have also developed a Rappture tool called nmie on Nanohub.org [14]. This tool calculates the extinction, scattering, and absorption efficiencies of single nanoparticle (1 layer), core@shell nanoparticle (2 layer) and nanomatryushka nanoparticle (3 layer) using Mie equation. The user can change the layer composition (Au/Ag or dielectric) and the refractive index of the surrounding medium, and also change the wavelength range of the calculation, as shown in Figure 2.14. we can do many simulation cases and compare with each other.

2.3.2 Synthesis of Ag Nanoparticles

Various methodologies are available to synthesize Ag nanoparticles such as, chemical reduction of silver ions, thermal reduction in organic solvents, reversed micelle processes, photoreduction, ultrasonic radiation, microwave irradiation [95, 96].

Among all the synthesis methods, the most frequently used procedure is the chemical reduction of Ag^+ into zero valent silver (Ag^0) in aqueous solution [97–105]. Commonly, a silver salt (e.g. $AgNO_3$) is mixed with a reducting agent (e.g. either sodium borohydride, $NaBH_4$ (See Eq. 2.5), or sodium citrate, $Na_3C_6H_5O_7$ (See Eq. 2.6)) and a coating agent (Figure 2.15 (a)). As shown in Figure 2.15 (a), we can see that after having been reduced,

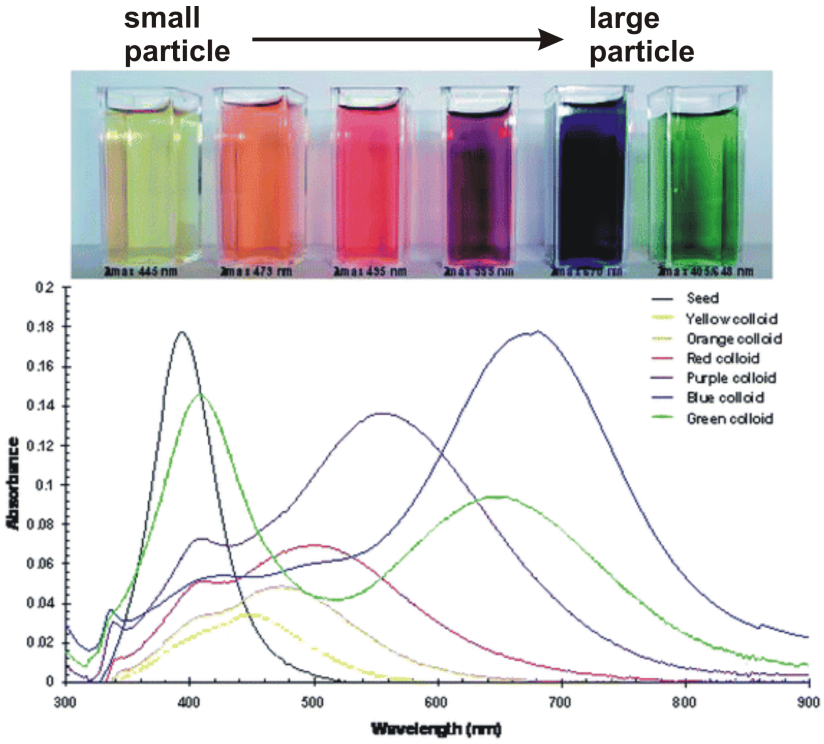

Figure 2.12: UV-Vis spectra of aqueous Ag colloids [12].

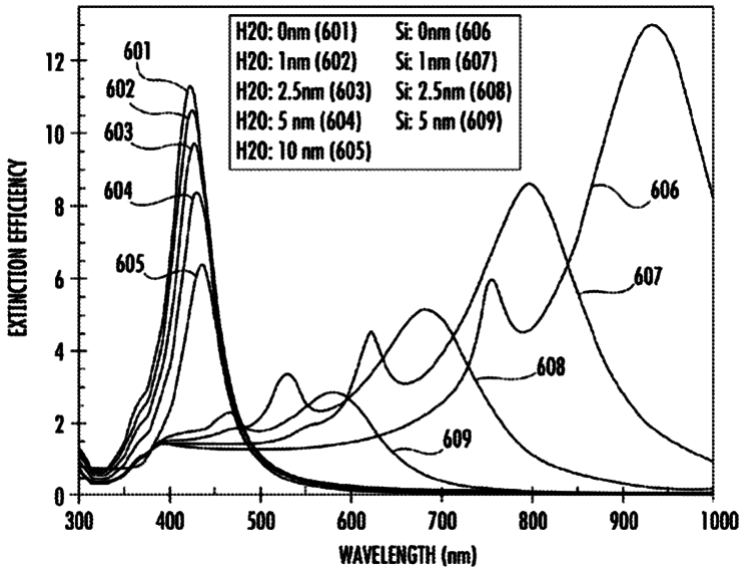

Figure 2.13: shows simulations of 50 nm silver nanoparticles coated with silica shells in water (601, 602, 603, 604, 605) and microcrystalline silicon (606, 607, 608, 609) environments. The curves are named according to the surrounding environment and the silica shell thickness [13].

Figure 2.14: Nmie tool calculates extinction, scattering and absorption efficiencies of single and multilayer nanoparticles [14].

the zero valent silver atoms aggregate thus forming the Ag nanoparticles. The coating agent like citrate ions attaches on their surface, preventing particle collisions and agglomeration, and adding specific properties to the Ag nanoparticles. However, this method employs many chemical agents making it hazardous to the environment. Following this, thermal reduction of Ag^{+} into zero valent silver (Ag^{0}) in organic solvents without requiring the addition the capping or reducing agents is much more suitable to be used in preparing Ag nanoparticles as it is relatively more environmentally friendly (Figure 2.15 (b)).

$$AgNO_3 + BH_4^- \rightarrow Ag^0 + \frac{1}{2}H_2 + \frac{1}{2}B_2H_6 + NO_3^- \tag{2.5}$$

$$2AgNO_3 + C_6H_5O_7^{3-} \rightarrow 2Ag^0 + C_5H_4O_5^{2-} + H^+CO_2 + 2NO_3^- \tag{2.6}$$

2.4 Core@Shell Nanoparticles

Various types of core-shell nanoparticles have been developed in outstanding efforts between academia and industry in the last decades. The core-shell nanoparticles exhibit improved physical and chemical properties over their single-component counterparts, and hence are

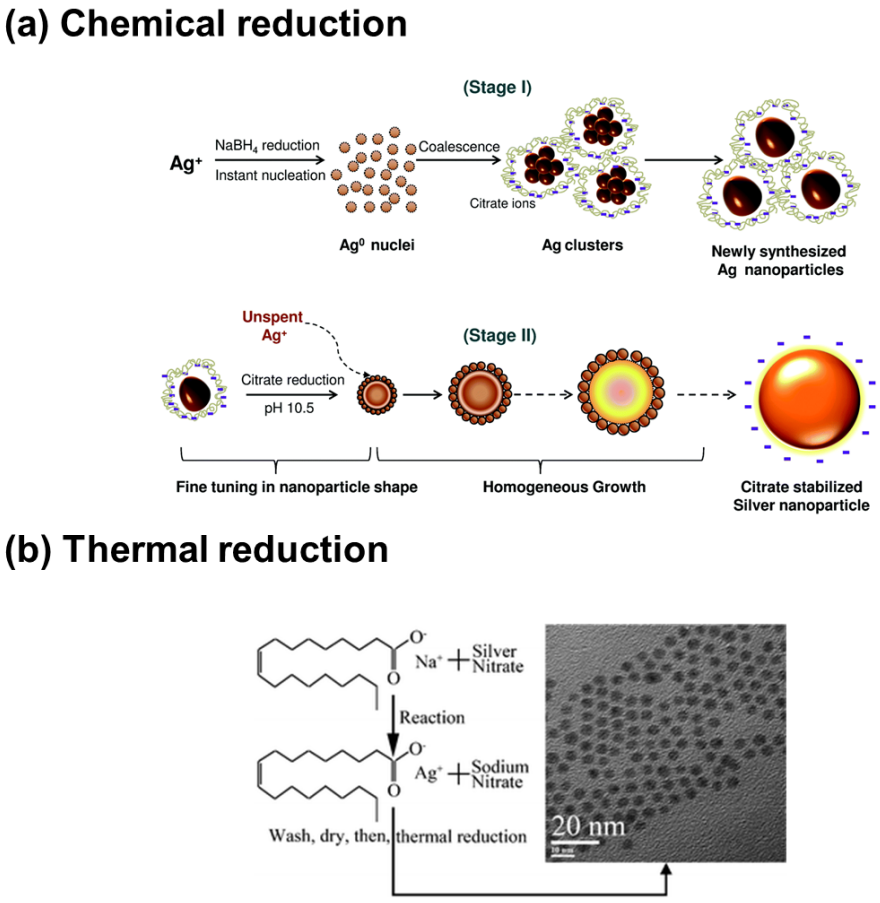

Figure 2.15: Schematic representation of Ag nanoparticles synthesized by (a) chemical reduction [15] and (b) thermal reduction [16].

potentially useful in a broader range of applications, for example, in biomedicine and electronics. Shell coatings with homogenous thicknesses can be grown on top of the nanoparticle, even leading to three layer structures and more. The shell materials can be metal or dielectric materials. Such a core@shell nanoparticle design, as shown in Figure 2.16, consists of a core, having the property, which demand the largest volume, for example, ferroelectricity or magnetism. The coating shell 1 is chosen to facilitate the chemical reactions needed for the functionalisation of the particles, but at the same time it can protect the active core from oxidation or degradation. The outmost shell provides the contact with the surrounding media and this shell is either hydrophilic or hydrophobic strongly depending on the applications. The choice of core or shell materials of the core-shell nanoparticle is strongly dependent on the end-use for different applications. Adela Ben-Yakar and co-works reported methods and compositions related to dielectric coated metal nanoparticles for the plasmonic enhancement of thin film solar cells through increased optical absorption [13]. Among the different inorganic material coating, SiO_2 is most common one.

1. SiO_2 shells: The coating of nanoparticles with silica shells is a popular option for a number of reasons. Silica is chemically inert and exceptionally stable, (especially in aqueous media), there are several well-established and simple protocols for its preparation, and its porosity can be controlled. SiO_2 particles can be synthesized with a Stöber process, while a modified Stöber process can be used to grow silica shells on metal cores. SiO_2 shells can have a profound impact on the plasmon resonance condition, which can be profitably used for photovoltaic applications [2]. The shell formation generally comprises two steps: the polymerization of TEOS, followed by addition of an outer thin shell, e. g. a different silane coupling agent bearing a functional group of further functionalisation. The most common example of these silanes is (3-Aminopropyl)triethoxysilane (APTES) that, after coating, yields nanoparticles with terminal amine groups. There has been an increasing number of examples reported in recent years, not only with magnetic (e.g. Fe_3O_4) nanoparticles [18, 106–108] (Figure 2.17 (a)), but also with other materials, such as ferroelectric (e.g. $BaTiO_3$) [109, 110] (Figure 2.17 (b)) and optical (e.g. Ag, Au) nanoparticles [20] (Figure 2.17 (c)).

2. Ag (Au) shells: For biomedical applications, Au and Ag are ideal coating due to their chemical inertness, extreme chemical stability, and biocompatibility, as well as easy functionalization, because they exhibit high-affinity binding to amine (-NH_2) or thiol (-SH) terminal groups of organic molecules [111]. Therefore, a great deal of research has been devoted to explore and develop nanocomposites, with required optical properties but within a suitable size range and so nanoshells were first introduced. These nanoshell

structures can be extremely interesting for plasmonic studies. Their most striking feature is that it is possible to adjust the plasmon resonance of the Ag (Au) shell coated nanoparticles over the whole visible and infrared region of the spectrum by adjusting the ratio of metal shell thickness to outer diameter of the particle. One of the most popular and successful approaches to the preparation of metal nanoshells is based on "self assembly monolayers (SAMs) and colloidal chemistry". For example, a new class of Au nanoshells containing dielectric $BaTiO_3$ cores are described by FarrokhTakin and co-workers [21], as shown in Figure 2.18 (I), where small Au particles (Au nuclei sites) are attached to the surface of $BaTiO_3$ particles and subsequent shell growth, reducing a Au salt in the presence of the Au nuclei sites. The thickness of the Au coating can be tuned by controlling the amount of the starting Au precursor. The plasmonic resonance peak of $BaTiO_3$@Au nanoshells is in the near infrared wavelength centered around 750 nm (Figure 2.18 (II)).

3. ABO_3 (perovskite) shells: So far, relatively little attention has been drawn to the fabrication and characterization of multiferroic core-shell nanoparticles with a ferromagnetic core and a ferroelectric shell as depicted in Figure 2.19, in such a configuration, an insulating ferroelectric perovskite ABO_3 layer is supposed to prevent an electrical contact between the more conducting magnetic phases, moreover, in which there is very good mechanical contact at the interface between two synthesized ferroic phases and high piezoelectric and magnetostrictive effects arise in both phases [112, 113]. In general, the synthesis of core-shell (perovskite) nanoparticles is conventionally carried out in two successive steps: (1) the precipitation of the core nanoparticles and (2) the creation of a perovskite shell around each nanoparticle. Liu and coworkers prepared spinel ferrite-perovskite core-shell nanoparticles like $Fe_3O_4/PbTiO_3$, γ-$Fe_2O_3/PbTiO_3$, γ-Fe_2O_3/Pb(Zr,Ti)O_3, $CoFe_2O_4/BaTiO_3$, $CoFe_2O_4/PbTiO_3$ and $CoFe_2O_4$/Pb(Zr,Ti)O_3 by combining a solvothermal route with conventional annealing [23]. Figure 2.20 shows the high-resolution TEM (HRTEM) image of the core-shell structure of γ-$Fe_2O_3/PbTiO_3$. After the coating, the ferroelectric layer dramatically affects the crystal structure, resistivity and magnetic properties of the composites. A similar approach was proposed by Buscaglia and coworkers, who reported on the preparation of γ-Fe_2O_3@$BaTiO_3$ [114] and $Ni_{0.5}Zn_{0.5}Fe_2O_4$@$BaTiO_3$ [115] core-shell submicron particles.

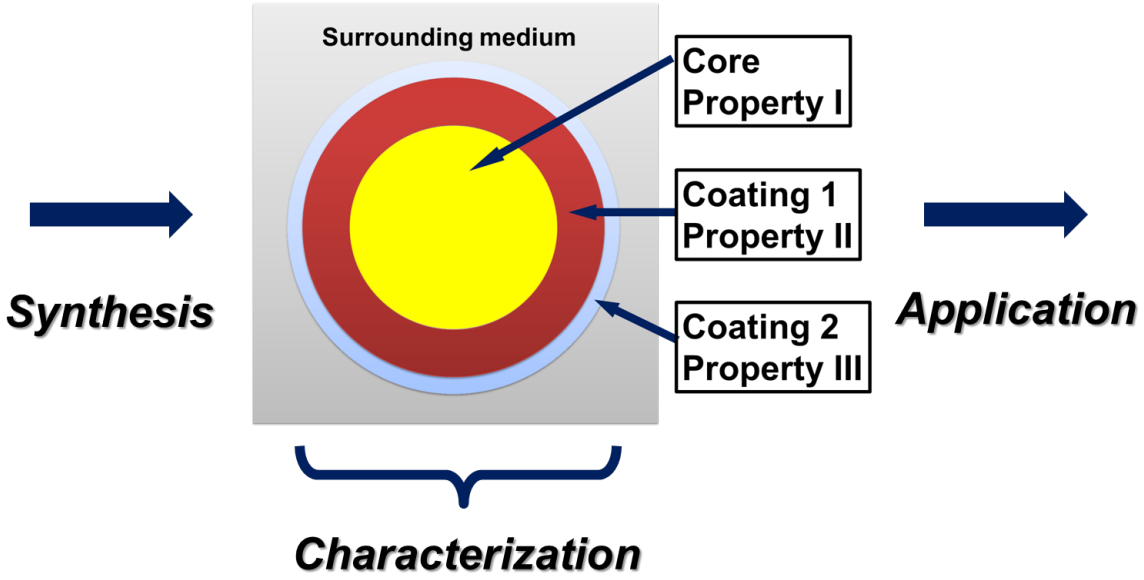

Figure 2.16: Schematic core-double shell nanoparticle emphasizing the importance of synthesis, characterization and application. The properties of the core and coating 1 are selective to the demand of the physics (e.g., optical and dielectric); the coating 2 is selected in view of the interaction with the surrounding medium (e.g., hydrophilic or hydrophobic) [17].

2.5 Concluding remarks

From the above study it can be concluded that nanoparticles and core-shell nanoparticles have lots of importance in different important areas especially biomedical, pharmaceutical, and electronics. Therefore, during the years different research groups have been trying to synthesize core@shell particles by different routes. But in all methods there are some limitations either particle separation is difficult or reaction steps are complicated. But in a hydrophobic organic surfactant medium it is easy to separate the particle after complete reaction and it is also cost effective. People have tried to synthesize particles in organic medium but most of them are mainly for single composite pure particles. Much less literature is available on core@shell nanoparticle synthesis in an organic surfactant medium.

In this thesis, we are trying to synthesize nanoparticles by using an "organosol" route that also provides a platform to produce nanoparticles with core@shell structures. Specifically we chose $BaTiO_3$ nanoparticle as both core and shell material with the intension to produce multifunctional $BaTiO_3$-based systems with a core@shell nanostructure. It is necessary to control the thickness of the shell to obtain shell behaviors while maintaining core properties.

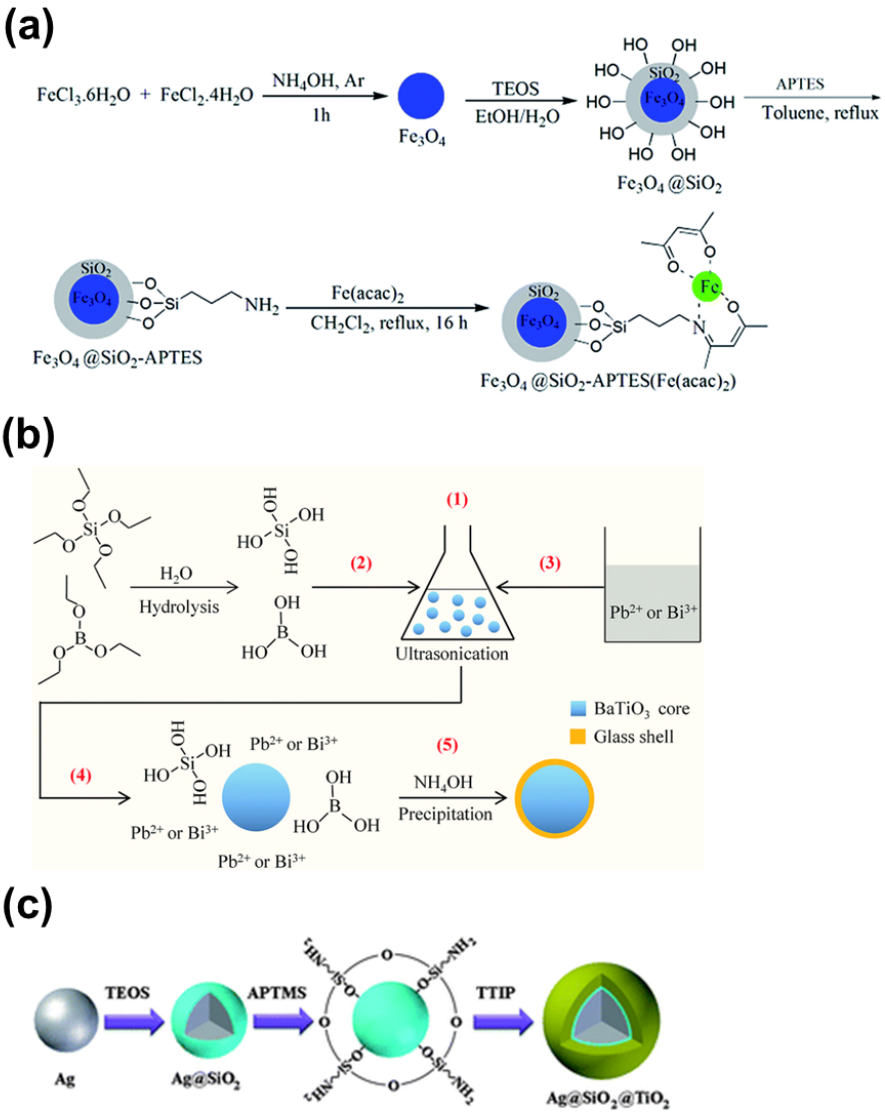

Figure 2.17: Schematic illustration of the preparation of (a) magnetically recoverable heterogeneous nanocatalyst Fe_3O_4@SiO_2-APTES($Fe(acac)_2$) [18], (b) $BaTiO_3$/low melting glass core-shell nanoparticles [19], and (c) Ag@SiO_2@TiO_2 triplex core-shell nanoparticles [20].

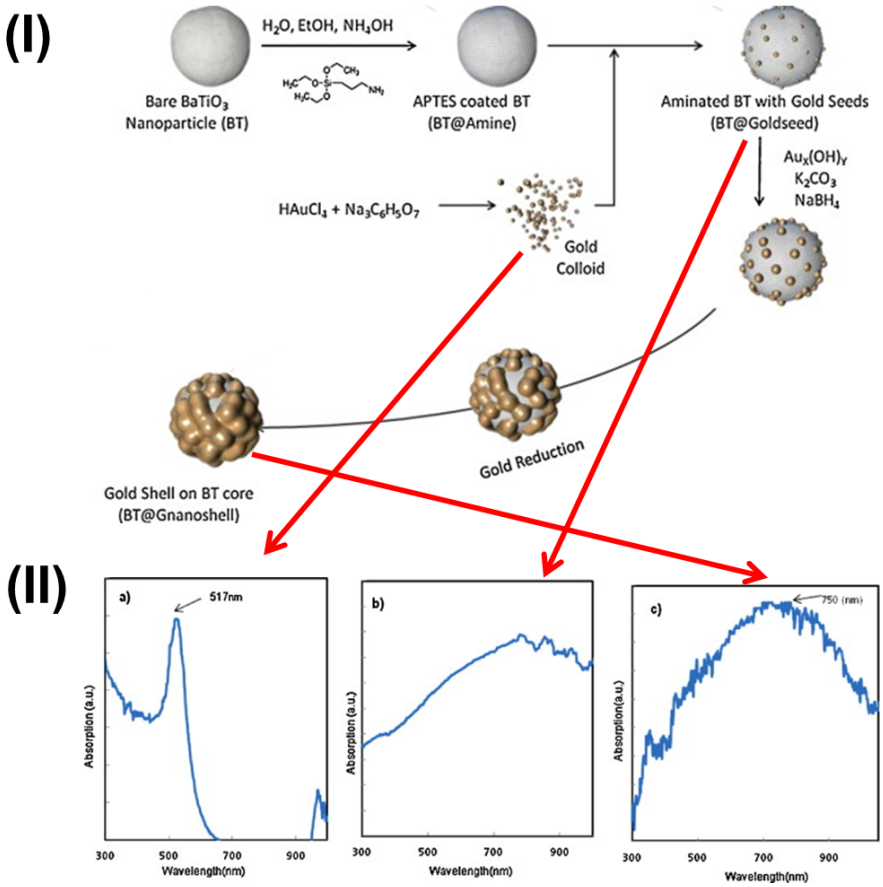

Figure 2.18: (I) The scheme of Preparation process of $BaTiO_3$@Au nanoshells. (II) UV-vis absorption spectra: (a) gold nanoparticles by Weiser method, characteristic SPR of λ = 517 nm, (b) $BaTiO_3$@Au seed, and (c) $BaTiO_3$@Au nanoshell, SPR red shift to 750 nm [21].

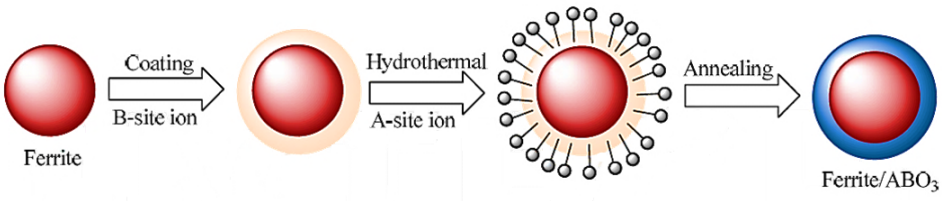

Figure 2.19: Schematic of the two-step approaches used for the fabrication of core-shell ferrite/perovskite nanoparticles by soft-solution routes [22].

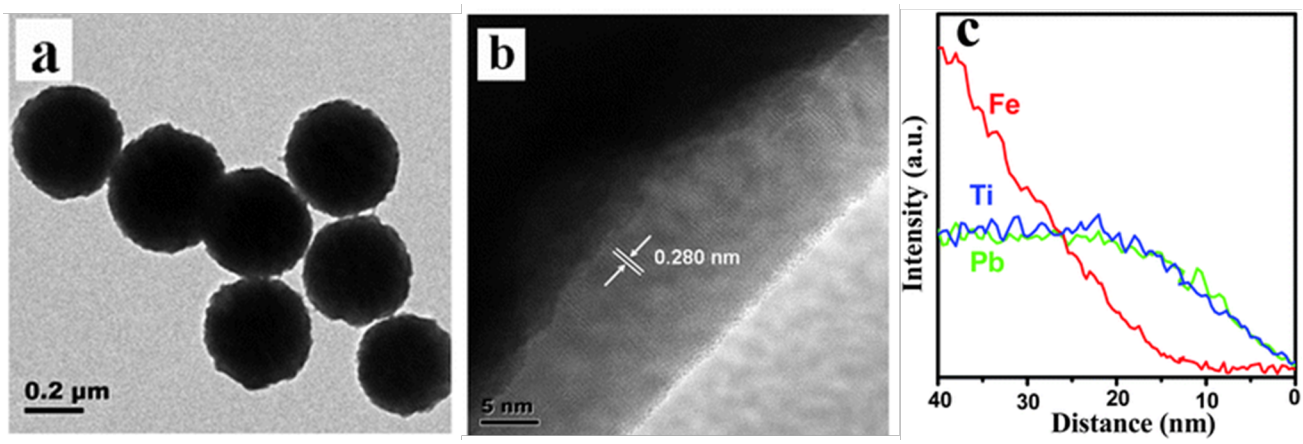

Figure 2.20: (a) TEM image of γ-Fe_2O_3/$PbTiO_3$. (b) HRTEM of a γ-Fe_2O_3/$PbTiO_3$ core@shell particle. (c) Position dependence of Fe, Pb and Ti elements from center to edge of a γ-Fe_2O_3/$PbTiO_3$ particle with a distance of 40 nm [23].

Chapter 3

Characterization Techniques for Nanoparticles

The discussion in this section is focused on the fundamentals and basic principles of the characterization methods. Technical details, operation procedures, and instrumentations are not the subjects of discussion here. The intention of this section is to provide a short summary. For details of the methods used in this work the reader is referred to the relevant literature [116–118].

3.1 Structural Characterization

3.1.1 Electron Microscopy

Electron microscopy is a technique of characterizing materials down to the atomic level. It has been serving as a powerful tool for analyzing and constructing new nanomaterials such as carbon nanotubes, metal and semiconductor quantum dots, and nanowires. We can broadly divide electron microscopy into two categories: Scanning Electron Microscopy (SEM) and Transmission Electron Microscopy (TEM).

3.1.1.1 Fundamentals of SEM

SEM is a type of electron microscope capable of producing high resolution images of a sample surface. It complements optical microscopy for examing and interpreting microstructure texture, topography, surface features and chemical composition ($< 1\ \mu m$). In SEM, electrons from the electron gun are focused to a small spot on the sample surface, 5 to 10 nm in diameter. The electron beam scans the sample like the spot on a television screen. Most of the

SEM operate at several to several tens of kilovolts. The resolution of a state-of-the-art field-emission SEM is around 5 nm. A schematic diagram of an SEM apparatus is given in Figure 3.1. A detailed description of the technique and background theory can be found elsewhere [119–121]. Image formation in SEM depends on the acquisition of signals produced from the electron beam and specimen interactions (Figure 3.2). The types of signals produced by an SEM include secondary electrons (SE), back-scattered electrons (BSE), and characteristic X-rays. The most widely used signal produced by the interaction of the primary electron beam with the specimen is the SE emission signal. When the primary beam strikes the sample surface causing the ionization of specimen atoms, loosely bound electrons may be emitted. These are referred to as secondary electrons. BSE are beam electrons that are reflected from the sample by elastic scattering. BSE images can provide information about the distribution of different elements in the sample. In addition to imaging versatility, SEMs are often coupled with X-ray analyzers, energy dispersive X-ray spectrometer (EDX or EDS). When an energetic electron beam is incident on the sample, X-rays are emitted when the electron beam removes an inner shell electron from the sample, causing a higher energy electron to fill the shell and release energy. These characteristic X-rays are used to identify the composition and measure the elements present in the sample.

SEM analyses for our samples were performed with a FEI Quanta 400 FEG Environmental Scanning Electron Microscope (ESEM) (Figure 3.3). This microscope is equipped with a field emission gun, operating at an accelerating voltage variable from 0.5 to 30 kV, with a claimed resolution of 2 nm. The instrument can be used in high vacuum mode (HV), low-vacuum mode (LV) and the so called ESEM (Environmental SEM) mode. The instrument is fitted with an EDAX Genesis energy-dispersive X-ray spectrometer for elemental analysis. Qualitative and quantitative analysis, elemental mapping and line scans can be performed.

For conventional imaging, specimens must be electrically conductive, at least at the surface, and electrically grounded to prevent the accumulation of electrostatic charge at the surface. Nonconductive specimens tend to charge when scanned by the electron beam, and especially in secondary electron imaging mode, this causes scanning faults and other image artifacts. They are therefore usually coated with an ultrathin coating of electrically-conducting material, commonly gold, deposited on the sample either by low vacuum sputter coating or by high vacuum evaporation. Conductive materials in current use for specimen coating include gold, gold/palladium alloy, platinum, iridium, tungsten, chromium and graphite. Coating prevents the accumulation of static electric charge on the specimen during electron irradiation.

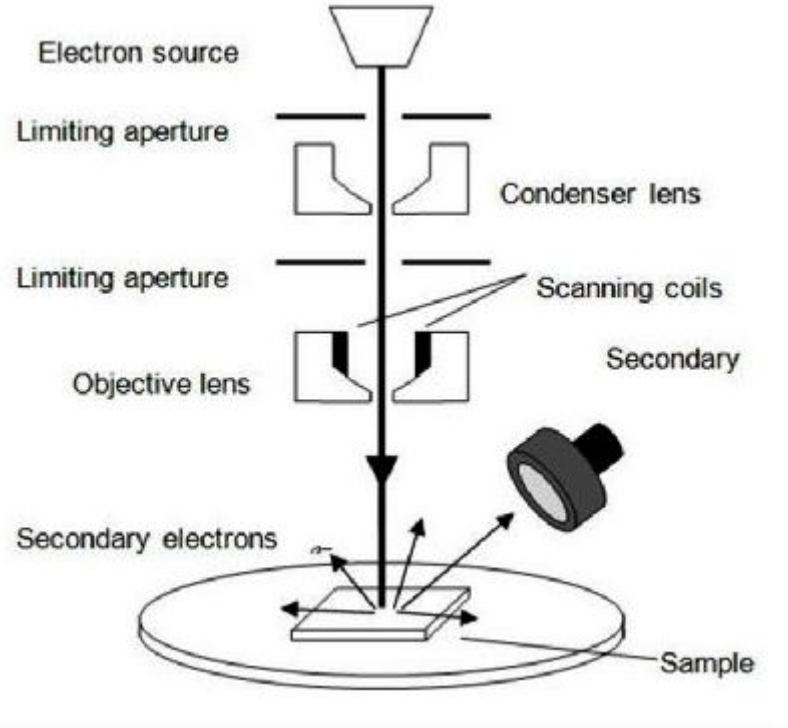

Figure 3.1: Schematic diagram of a scanning electron microscope [24].

3.1.1.2 Fundamentals of TEM

TEM is one of the most important tools of nanotechnology for imaging nanomaterials with sub-nanometer resolution (High-Resoluion TEM). It provides access to much information about the sample, such as analysis of crystalline defects and interfaces at the atomic scale, multilayers, nanoscrystals and nanostructures.

In comparison to SEM, TEM uses the transmitted electron signal. In order to get any information using TEM, the specimens have to be electron transparent (< 100 nm). The typical acceleration voltage is 80-200 kV. The electrons are emitted from a thermionic electron emitter. The illumination aperture and the area of specimen illuminated are controlled by a set of condenser lenses (Figure 3.4). The function of the objective lens is either image or diffraction pattern formation of the specimen. TEM diffraction patterns are used to identify the crystal structure and lattice repeat distance (Figure 3.5). In our case, the image mode is used to investigate the size and distribution of the nanoparticles. The crystalline structure is studied by the diffraction mode. A detailed description about TEM can be found elsewhere [121–123].

The FEI Tecnai F20 TEM is used to get information regarding particle size, particle shape and crystal structure (Figure 3.6). It has a maximum operating voltage of 200 kV, with a point-to-point resolution of 0.24 nm and lattice resolution of 0.14 nm. Three sample holders

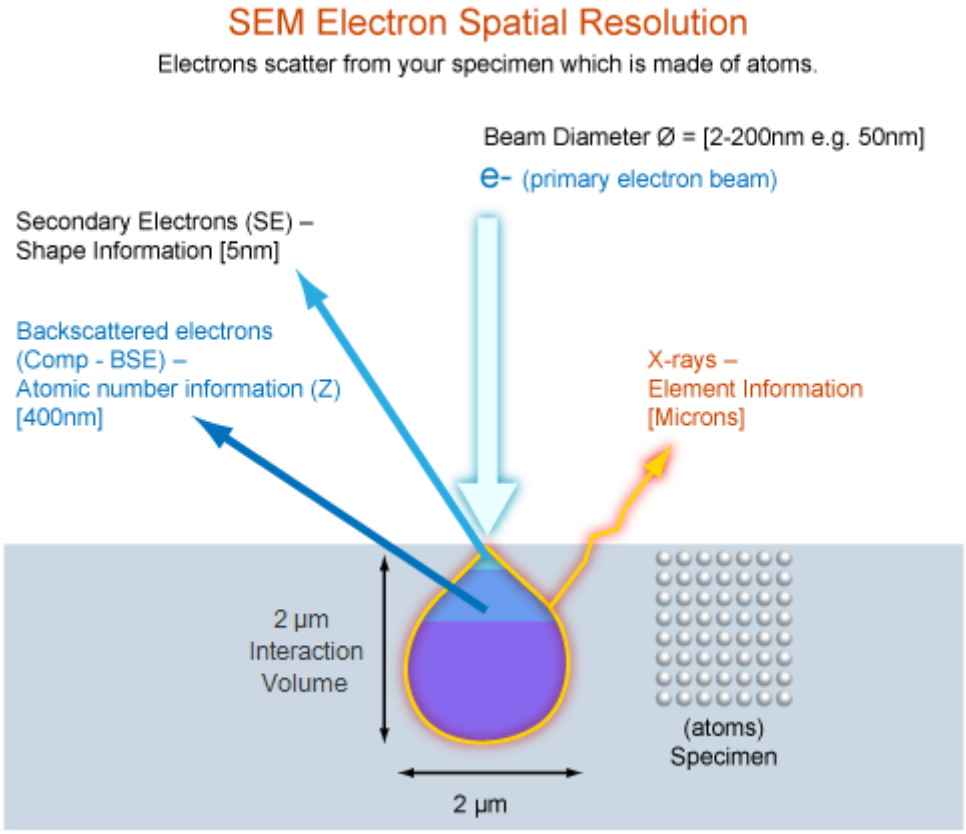

Figure 3.2: The typical spatial resolution of different signals, secondary electrons, backscattered electrons and X-rays, in the scanning electron microscope [25].

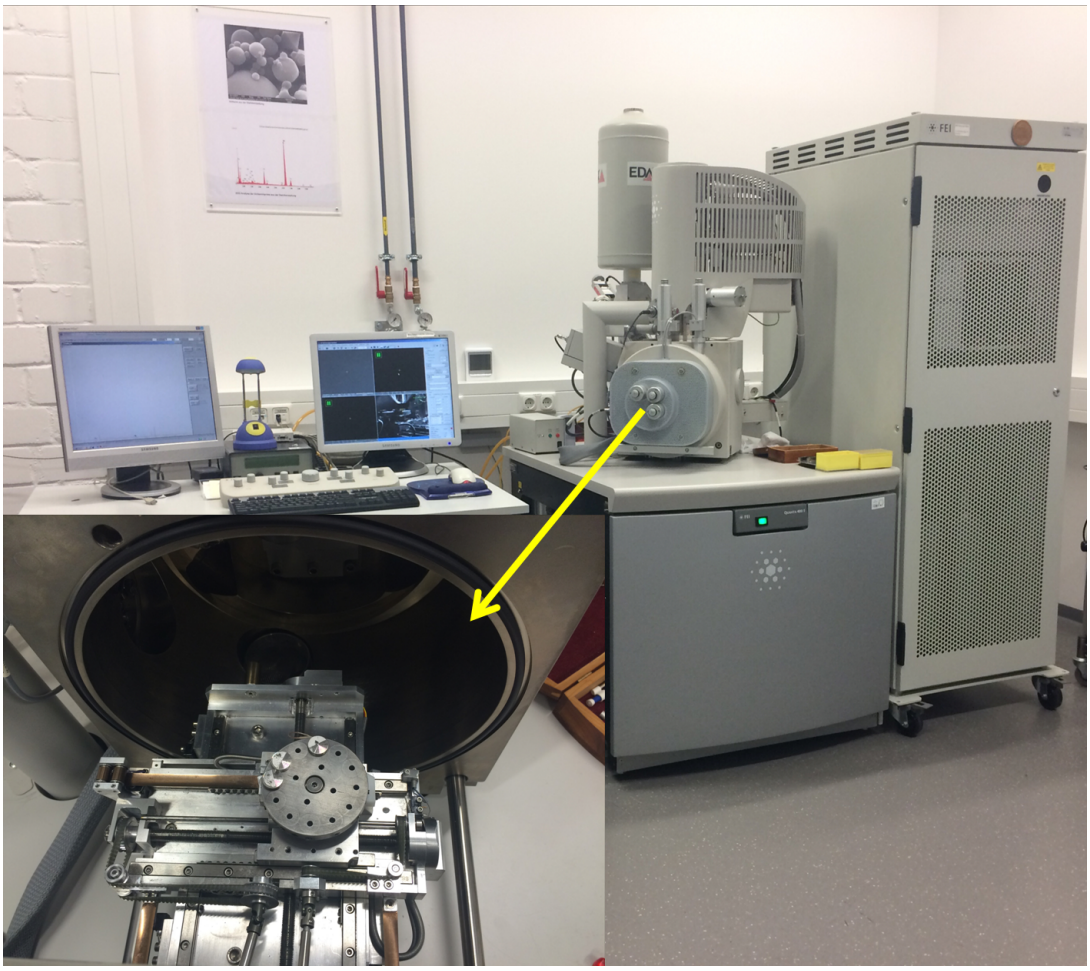

Figure 3.3: FEI Quanta 400 FEG Environmental Scanning Electron Microscope.

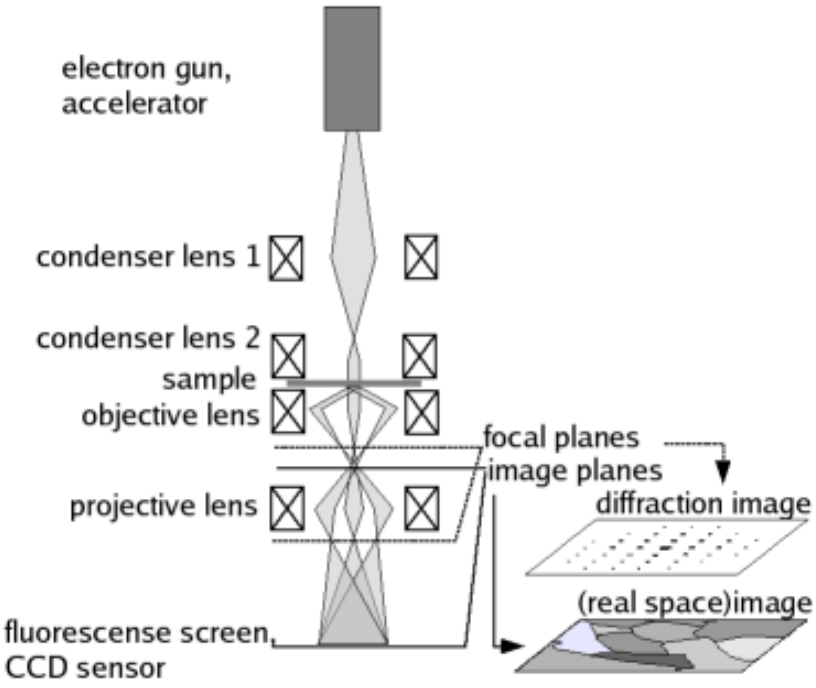

Figure 3.4: Ray diagram of a transmission electron microscope for imaging and diffraction.

are available: a standard, room-temperature holder, a high-tilt tomography room-temperature holder, and a Gatan 626 high-tilt Cryo-sample holder. The microscope is equipped with a CCD camera for STEM, HAADF detector, and EDAX EDX, and is also equipped with the FEI Xplor3D tomographic data acquisition software.

3.1.2 X-ray Powder Diffraction

The X-ray powder diffraction (XRD) is a routine technique used for the characterization of crystalline solids and determination of their structure, e. g. how the atoms pack together in the crystalline state and the size and the shape of the unit cell, etc. It is a non-destructive technique and requires no elaborate preparation of samples.

An expanded view of the diffraction of X-rays from the repeating planes of atoms in a crystalline structure is shown in Figure 3.7. Powder diffraction patterns are typically plotted as the intensity of the diffracted X-rays vs. the angle θ-2θ geometry. Peaks will appear in the diffraction pattern at 2θ values when constructive interference is at a maximum, that is, when Bragg's Law ($n\lambda = 2d_{hkl}sin\theta$) is satisfied, where θ is the angle between the incident beam and scattering planes, d_{hkl} is the spacing between the planes in the atomic lattice, n is an integer determined by the order give, and λ is the wavelength of the incident X-ray beam.

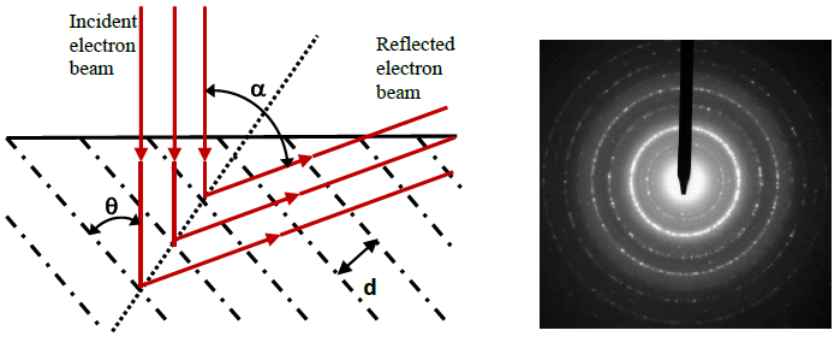

Figure 3.5: Schematic of a beam incident on a pair of planes separated by a distance d, and Electron diffraction pattern of a polycrystalline sample [26].

In our experiments a Siemens D-5000 X-ray powder diffractometer (λ = 1.5418 Å (Cu $K\alpha$)) was used (Figure 3.8). During data collection, the sample remains in a fixed position and the X-ray source and detector are programmed to scan over a range of 2θ values. The working conditions were typically: 2θ scanning between 20° and 90°, with a 0.01° step and a scanning speed of 1°/sec. By measuring the 2θ values for each diffraction peak, we can calculate the d-spacing (the distance between the diffracting planes) for each diffraction peak. A PC with the Bruker DiffracPlus software suite installed controlls the diffractometer. The diffractograms are analysed by evaluation program EVA 3.0 of package Diffrac Plus Basic from Bruker Analytical X-ray systems. The phases are identified using JCPDS files.

3.2 Chemical Characterization

3.2.1 Ultraviolet-visible Spectroscopy

Ultraviolet-visible (UV-Vis) spectroscopy refers to absorption spectroscopy or reflectance spectroscopy in the UV-Vis spectral region (i.e 200nm-800nm) of the electromagnetic spectrum. In this region of the electromagnetic spectrum, atoms, ions or molecules undergo electronic transitions from ground state to excited state. The absorbed or transmitted light for given material is the characteristic of its chemical structure. A spectrum is a graphical representation of the amount of light absorbed or transmitted by matter as a function of the wavelength. The UV-Vis spectrometer records absorption, A, as a function of the incident light wavelength [124]. The analysis is based on Beer-Lambert law (Eq. 3.1).

$$A(\lambda) = -log(\frac{I}{I_0}) = \varepsilon \cdot b \cdot c \tag{3.1}$$

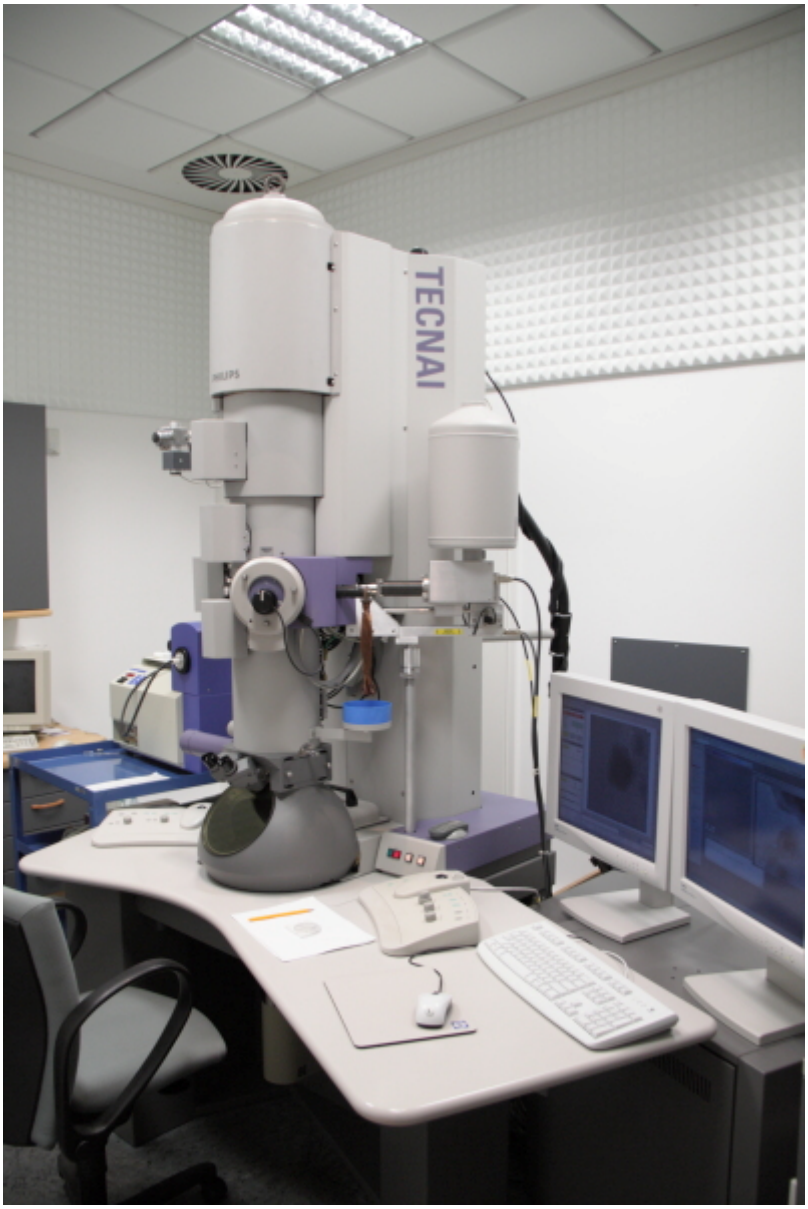

Figure 3.6: FEI Tecnai F20 Transmission Electron Microscope.

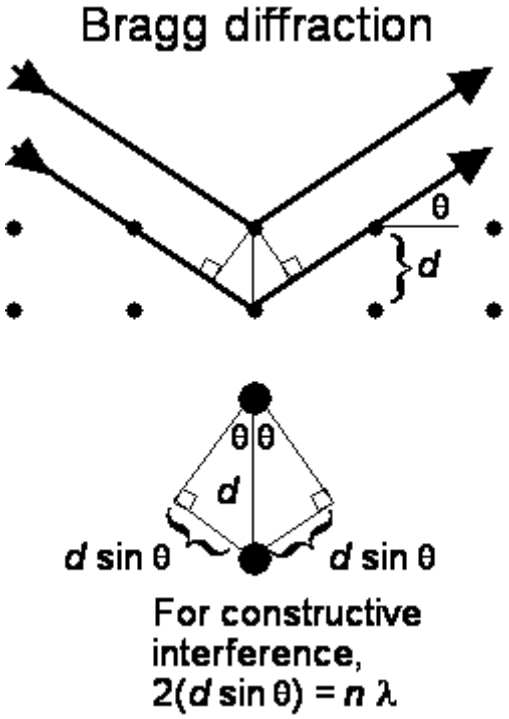

Figure 3.7: A graphical representation of X-ray Radiation Diffracting from crystal planes and what Bragg's law represents.

Figure 3.8: Siemens D5000 Powder X-ray diffractometer.

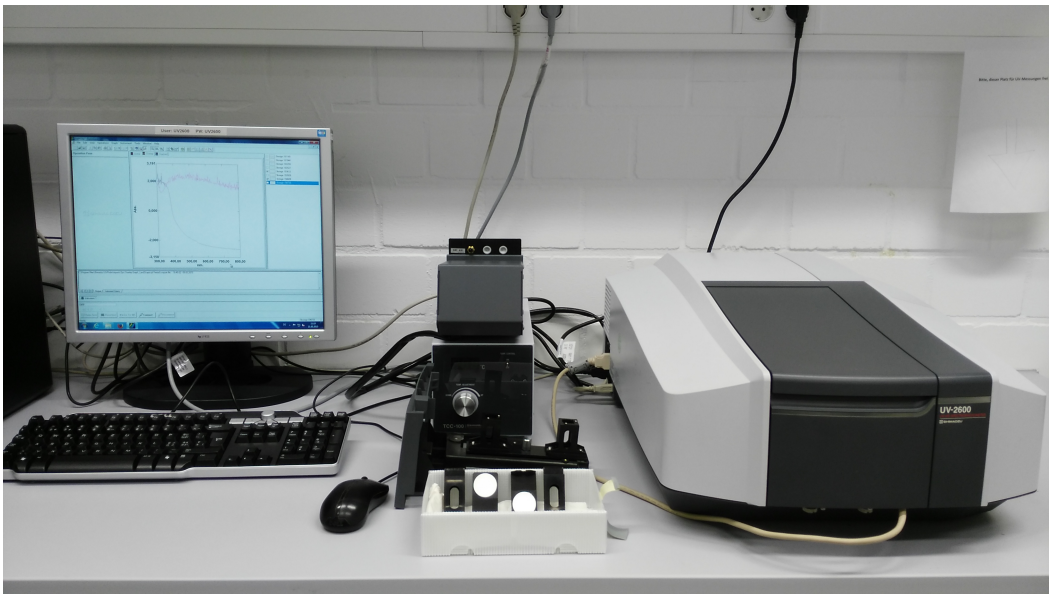

Figure 3.9: UV-2600-Shimadzu UV-Vis spectrophotometer.

where I_0 is the incident light intensity, I is the resulting intensity, A (dimension less quantity) is the absorbance, b (cm) is the cell path length, c is concentration (moles/liter) of the solution and ε is the molar absorptivity (liter/mole/cm).

With respect to nanoparticle analysis, UV-Vis spectroscopy is particularly effective in cases where the surface plasmon resonance of metal nanoparticles is in the visible spectrum. It is a useful technique which allows to estimate the nanoparticle size, concentration, and aggregation level. As a part of this research work, a UV-2600-Shimadzu UV-Vis spectrophotometer was used for optical characterization of the synthesized nanoparticles (Figure 3.9). The UV-Vis measurements spanned a wavelength range from 200 nm up to 1.400 nm. The containers for the sample and reference solution must be transparent to the radiation which will pass through them. Quartz cuvettes are required for spectroscopy in the UV range. These cells are also transparent in the visible range. The cuvettes are rectangular and 1 cm of interior width. This width is the path length (b) in the Beer-Lambert law.

3.2.2 Fourier Transform Infrared Spectroscopy

Fourier transform infrared (FT-IR) spectroscopy is an excellent chemical analytical tool due to the correlation between the wavenumbers at which a molecule absorbs infrared radiation and its structure. According to this correlation, the structure of unknown molecules can be identified from its infrared spectra, as well as quantitative information can be also provided, such as the concentration of a molecule in a sample. Infrared radiation is electromagnetic ra-

Functional Group	Type of Vibration	Characteristic Absorptions (cm-1)	Intensity
Carbonyl			
C=O	stretch	1670-1820	strong
Acid			
C=O	stretch	1700-1725	strong
O-H	stretch	2500-3300	strong, very broad
C-O	stretch	1210-1320	strong
Aldehyde			
C=O	stretch	1740-1720	strong
=C-H	stretch	2820-2850 & 2720-2750	medium, two peaks
Amide			
C=O	stretch	1640-1690	strong
N-H	stretch	3100-3500	unsubstituted have two bands
N-H	bending	1550-1640	
Anhydride			
C=O	stretch	1800-1830 & 1740-1775	two bands
Ester			
C=O	stretch	1735-1750	strong
C-O	stretch	1000-1300	two bands or more
Ketone			
acyclic	stretch	1705-1725	strong
cyclic	stretch	3-membered - 1850 4-membered - 1780 5-membered - 1745 6-membered - 1715 7-membered - 1705	strong
α,β-unsaturated	stretch	1665-1685	strong
aryl ketone	stretch	1680-1700	strong

Table 3.1: Characteristic IR Absorption Frequencies of Functional Groups Containing a Carbonyl (C=O).

diation which covers the wavenumbers between 13300 cm^{-1} and 3.3 cm^{-1}. The infrared region is usually divided into 3 regions: near-infrared (13300 - 4000 cm^{-1}), middle-infrared (4000 - 200 cm^{-1}) and far-infrared (200 - 3.3 cm^{-1}) regions. Organic compounds have fundamental vibration bands in the mid-infrared region, which is why the region is widely used in infrared spectroscopy [125]. Table 3.1 shows the characteristic IR Absorption frequencies of some functional groups containing a carbonyl (C=O).

In this research work FT-IR spectra were measured out on a Bruker Vertex 70 spectrometer (Figure 3.10) in the range 4000 - 400 cm^{-1} using transmittance (%) - wavenumber (cm^{-1}) dependence and higher precision running parameters: spectral resolution better than 0.01 cm^{-1}, photometric accuracy better than 0.1%, and OPUS v.6.0 software for the spectra acquisition. All spectra were baseline corrected. The samples were prepared in KBr (potassium bromide) pellets.

Figure 3.10: Bruker Optics Vertex 70 FTIR Spectrometer.

3.3 Particle Charge Characterization

One of the most important parameters in the colloidal system is the surface charge of the nanoparticles. Nearly any surface of the nanoparticles carries ionic charge. When it is sufficiently high nanoparticles repel each other keeping a dispersion stable. If it is low, the nanoparticles of the dispersion may coagulate. When suspended in water, the nanoparticle surface charge is immediately compensated by surrounding ions, forming an electrostatic double layer (Figure 3.11) [126]. A means of investigating their surface charges is highly desirable in order to try to predict and control their behaviour during preparation, processing and application. A valuable parameter in this respect and one which can be easily determined is the zeta potential, ζ, which exists at the effective boundary between the particle and its surrounding medium.

3.3.1 Charge Titration

The Stabisizer® instrument opens the door to particle charge analysis. The interface potential of particles is measured as streaming/zeta potential and represents the degree of electrostatic repulsion between particles [127]. The Stabisizer® particle charge titration system is based on the well established oscillating streaming potential method (Figure 3.12 (b)). The surface charge is related to the so-called streaming potential (SP) of the suspended particles inside a narrow capillary. In this research work, both streaming potential (mV) and pH are measured simultaneous using the Stabisizer PMX 200C set-up from Particle Metrix GmbH (Figure 3.12 (a)). Prior to measurement, the Teflon beaker and pistons were cleaned with piranha solution

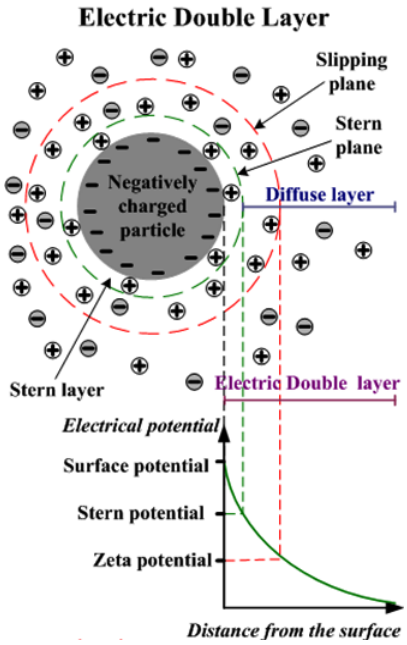

Figure 3.11: Schematic representation of the distribution of ions around a charged particle in solution.

(H_2SO_4:H_2O_2=3:1) and then rinsed with ultrapure water. 10 μL of the sample ($BaTiO_3$ or $BaTiO_3$@SiO_2) was dispersed into 10 ml of 10 mM KOH solution. Then this solution was poured in to the Teflon beaker. This beaker has two electrodes - anode and cathode. A pH meter was fixed to the beaker in such a way that it can come into contact with the solution. An apropriate piston was immersed into the beaker and the mixture was titrated with 5 mM HCl till pH 2. When the dispersion is titrated versus pH, the iso-electric point (IEP) is the pH with 0 mV potential. The iso-electric point (IEP) of any nanoparticle dispersion is seen as the maximum point of instability (Figure 3.13).

Further to the surface potential measurement capabilities of the system PMX 200C, a dynamic light scattering (DLS) size measurement is available as an option. The PMX 200CS is the model equipped with a 180° DLS Nanotrac® probe (Figure 3.12 (a)) for measuring the size and size distributions in the range of 0.8 nm to 6.5 μm.

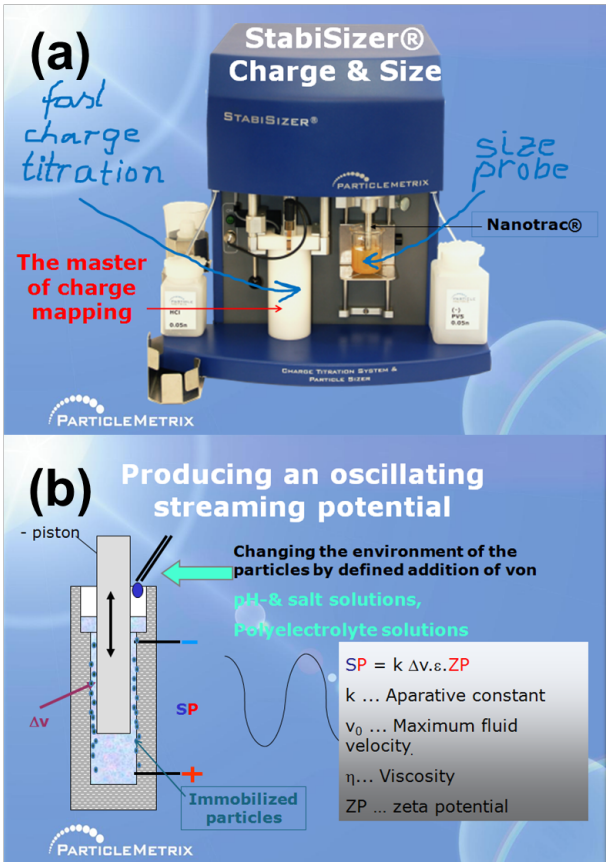

Figure 3.12: (a) Stabisizer PMX 200C and (b) sample cell with oscillating piston and oscillating streaming potential (SP) that is proportional to the zeta potential of the particles.

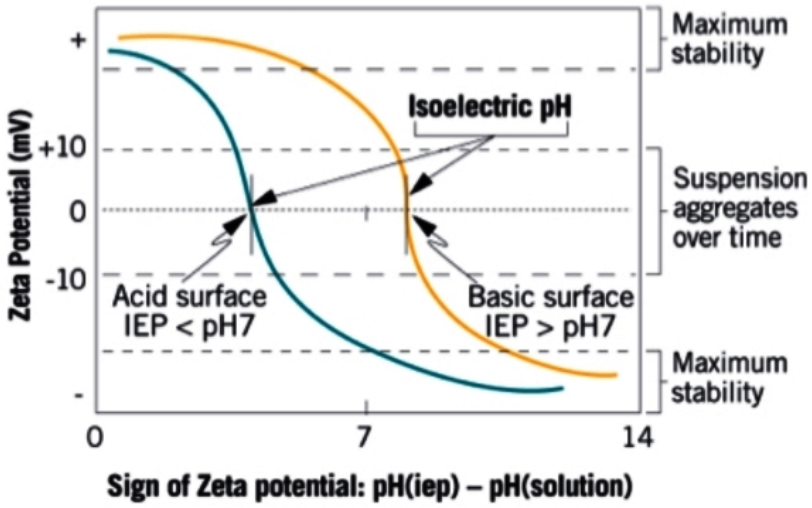

Figure 3.13: Effect of pH on Zeta Potential [27].

Research Work

The following chapters of the thesis are based on the following publications:

- Chapter 4

Y. Gao, V. V. Shvartsman, A. Elsukova, and D. C. Lupascu, “Low-temperature synthesis of crystalline $BaTiO_3$ nanoparticles by one-step "Organosol”-precipitation,” ***J. Mater. Chem.*** **22**, 17573-17583 (2012).

- Chapter 5

Y. Gao, A. Elsukova, D.C. Lupascu, “Preparation of SiO_2 Encapsulated $BaTiO_3$ Nanoparticles with Tunable Shell Thickness by Reverse Microemulsion,” ***Particle and Particle Systems Characterization*** **30** (10), 832–836 (2013).

- Chapter 6

Yanling Gao, Nadia Gharbi, Simon Kugai, Anna Elsukova, and Doru C. Lupascu, “Core@shell Ag@$BaTiO_3$ Plasmonic Absorber Systems Synthesized via the Organosol Route,” in preparation.

Chapter 4

Low-temperature synthesis of crystalline $BaTiO_3$ Nanoparticles by one-step "Organosol”-precipitation

4.1 Abstract

The “Organosol”- precipitation method is proposed to produce nanosized particles of barium titanate ($BaTiO_3$) at temperatures as low as room temperature. The advantages of this method are a high yield, a simple but precise control of the size of the particles, low process temperature, short reaction time, as well as low cost of reagents. The particles were systematically characterized by powder X-ray diffraction (XRD), Raman scattering, scanning electron microscopy (SEM), high-resolution transmission electron microscopy (HRTEM), thermogravimetric thermal analysis (TGA/DSC), infrared spectroscopy (IR), and impedance analysis. The nearly uniform sized $BaTiO_3$ nanocrystals exhibit granular shape of around 15 nm in diameter. Oleic acid retards crystallization and thus allows generating a uniformly small grain size and excellent dispersibility in organic solvents. The surface energy of the particles is modified and crystallization in cubicles also arises. The mechanism of powder formation is discussed. The method offers an alternate low-cost route to perovskite nanopowders easily dispersed in organic media.

4.2 Introduction

With the recent demands placed on cellular and mobile technologies the need for nanoparticles of highly engineered materials has increased. The high volume, low cost, and superior

properties of passive electronic components requires that precision powders for electronic components are inexpensive, of high quality, and can be produced at high yield. The synthesis of high quality powders of high dielectric constant, especially perovskite structured materials, has been of specific interest. The dependence of volumetric capacitance of a multi-layer ceramic capacitor (MLCC) on the thickness of the active layer is well-documented. Nanoparticles and their assembly provide potential to reduce layer thickness below the current standard of 1 μm [4, 128, 129]. Much work on a variety of synthesis routes for the synthesis of barium titanate ($BaTiO_3$) nanoparticles has appeared recently. Solid-state carbonate reactions [130], a modified Clabaugh process [131], and low temperature direct synthesis (LTDS) [53] and several other routes [132–134] have all been investigated. The first two routes are common commercial methods used to produce powders, however each require further processing, either milling or calcination, to produce nanoscale $BaTiO_3$, while powders produced by LTDS have a high hydroxyl defect concentration and a low Ba/Ti ratio. More recently Brutchey et al. [135–138] utilized a vapour diffusion sol-gel route that offers a very low temperature (16 °C), economical and environmental friendly pathway to 6 nm $BaTiO_3$ nanoparticles. However, it could be difficult to enlarge the reaction scale by using this method (e.g. in terms of cost feasibility). In this work, the "organosol" route is proposed to produce nanosized particles of $BaTiO_3$ at temperatures as low as room temperature. The advantages of this method are a high yield, a simple but precise control of the size of the particles, low process temperature, short reaction time, as well as low cost of the reagents. Under the correct synthesis conditions powders can be produced with low defect concentrations and controlled stoichiometry that requires no further processing making "organosol" synthesis an excellent choice for the commercial synthesis of $BaTiO_3$. Furthermore, the interest in undertaking this work was to synthesize $BaTiO_3$ nanoparticles with good dispersibility in organic media. Because the hydrophobic $BaTiO_3$ nanoparticles not only yield improved compatibility for homogeneous dispersions in polymer matrix layers, but also acted as inorganic fillers in polymer-based composites to increase the effective dielectric constant. The as-prepared $BaTiO_3$ nanocrystals exhibit a granular shape of around 15 nm in diameter. Oleic acid retards crystallization and thus allows generation of a uniformly small grain size and excellent dispersibility in organic solvents. The surface energy of the particles is modified and crystallization in cubes also arises. The mechanism of powder formation will be discussed below.

4.3 Experimental Details

4.3.1 Preparation of a barium titanium oleate precursor

All chemicals were reagent grade and used without further purification. Barium acetate ($Ba(CH_3COO)_2$, $Ba(OAc)_2$, 99%, Sigma-Aldrich, Steinheim, Germany) and titanium isopropoxide ($Ti(OCH(CH)_2)_4$, $Ti(O^iPr)_4$, 97%, Sigma-Aldrich, Steinheim, Germany) were used as the barium and titanium sources, respectively. Oleic acid ($((CH_2)_7CH]CH(CH_2)_2COOH$ or RCOOH/OA, 65-88%, Sigma-Aldrich, Steinheim, Germany) and toluene were used as the surfactant and organic solvent in precursor preparation, respectively. Figure 4.1 is a flow diagram of the procedure used in the synthesis. The total concentration of the precursor was 0.2 M with a molar ratio of Ba : Ti of 1 : 0.93. Degassed distilled water was utilized as an additional agent for preparing 4 M NaOH solution. A sketch of the experimental process is shown in Figure 4.2 according to the following chemical reactions:

Substitution:

$$Ti(O^iPr)_4 + RCOOH \rightarrow Ti(O^iPr)_{4-x}(OOCR)_x + xPrOH \tag{4.1}$$

$$Ba(OAc)_2 + RCOOH \rightarrow Ba(OOCR)_2 + HOAc \tag{4.2}$$

Nucleophilic attack by $RCOO^-$

$$Ti(O^iPr)_{4-x}(OOCR)_x + Ba^{2+} + 2RCOO^- \rightarrow [Ti(O^iPr)_{4-x}(OOCR)_{x+2}]^{2-} + Ba^{2+} \tag{4.3}$$

To simplify notation: $[Ti(O^iPr)_{4-x}(OOCR)_{x+2}]^{2-} \rightarrow [Ti(OR')_6]^{2-}$
Strongly alkaline condition:

$$[Ti(OR')_6]^{2-} + 6OH^- \rightarrow [Ti(OH)_6]^{2-} + Ba^{2+} \rightarrow BaTiO_3 + H_2O \tag{4.4}$$

$$RCOO^- + Na^+ \rightarrow RCOONa$$

2.55 g of barium acetate were suspended in a solution of 60 ml oleic acid. First, argon gas was flowed through the entire reaction system at a constant rate for 1 hour. Then the suspension was heated up to ca. 450 °C (reflux temperature) under argon atmosphere at which

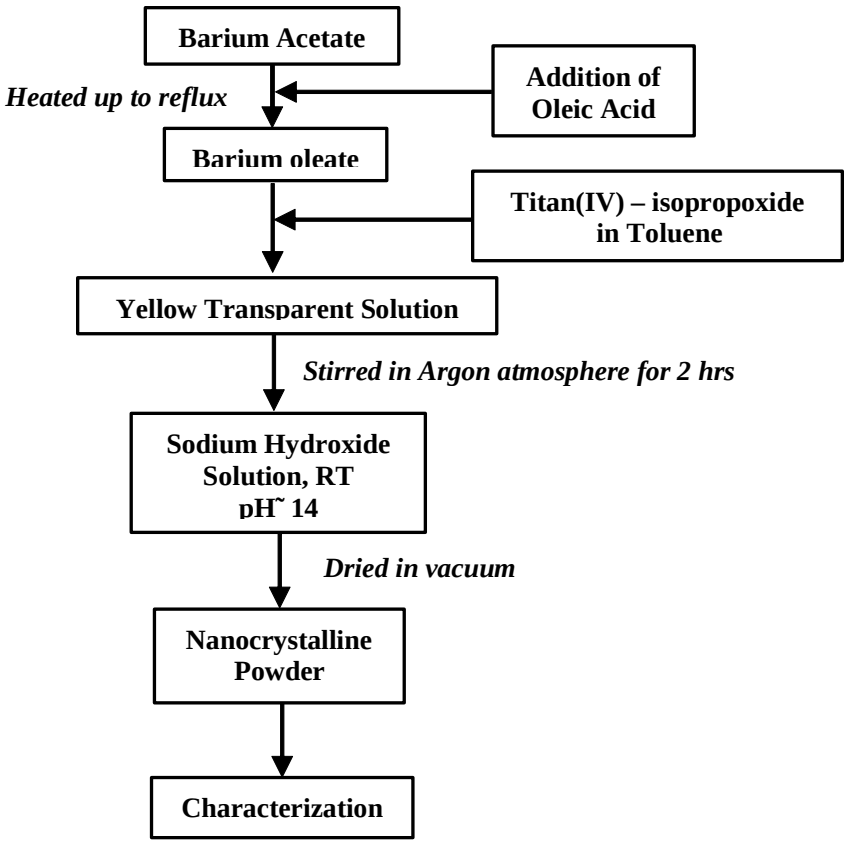

Figure 4.1: A schematic procedure for synthesis of $BaTiO_3$ nanoparticles.

point a bright yellow transparent solution of barium oleate was formed. After cooling to 80-100 °C under argon flow, 2.75 ml $Ti(O^iPr)_4$ and 80 ml toluene solution were quickly moved into the reaction chamber under magnetic stirring to obtain an orange transparent solution of a barium titanium oleate complex precursor. This fresh organic precursor solution was stirred for 2 hours under argon atmosphere to produce a homogeneous solution.

4.3.2 Synthesis of $BaTiO_3$ nanoparticles

The above barium titanium oleate complex precursor was mixed with 100 ml of 3 M NaOH (pH > 13). Immediately, a slightly yellow-white slurry was formed. The excess liquid was removed by vacuum filtration, and the dried slurry was kept in a vacuum drying oven at various reaction temperatures (25 °C, 40 °C, 60 °C, 80 °C and 100 °C) for 12 hours for solidification and crystallization. The dried powders were washed with methanol and acetone while performing ultrasonic treatment for 20 minutes to get rid of the “free” oleates. After centrifuging, as-prepared $BaTiO_3$ nanoparticles were collected. The three subsequent treatment conditions used were: I) calcination, II) washing, and III) washing and calcination. Ethanol /1 % acetic

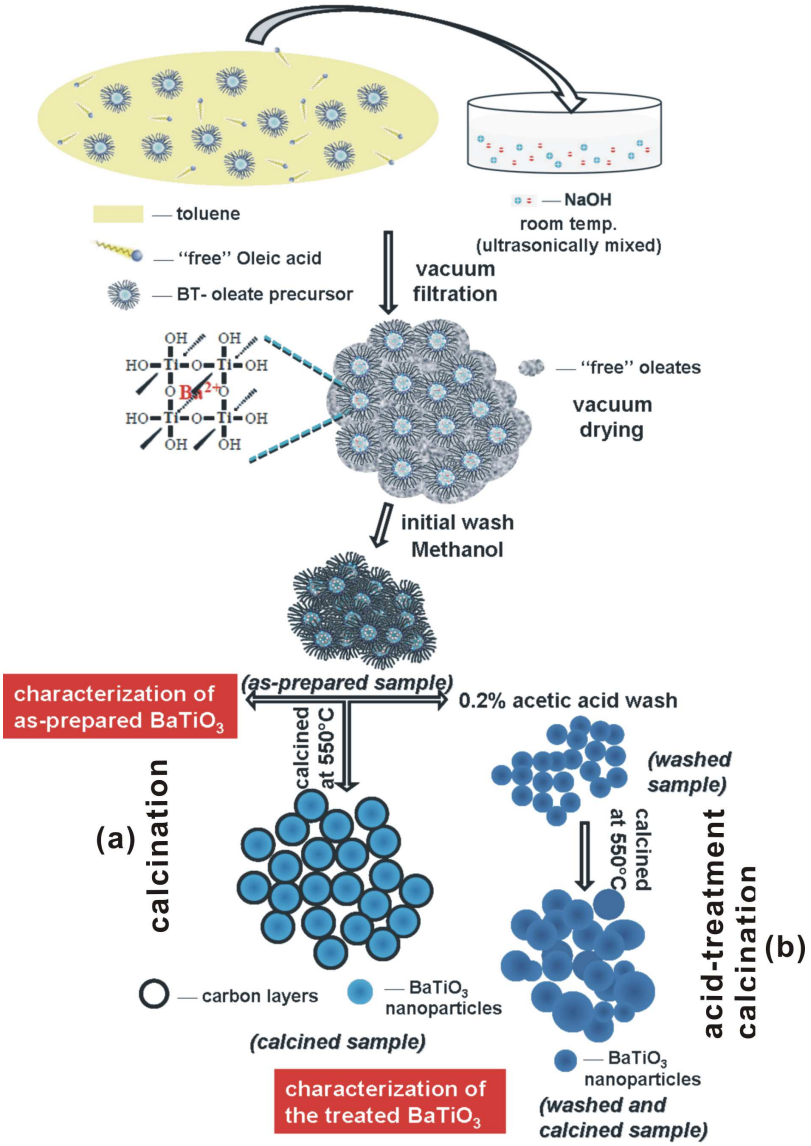

Figure 4.2: Schematic diagram of the synthesis procedure and treatment conditions of the $BaTiO_3$ nanoparticles: (a) calcination and (b) acid-treatment and calcination.

acid (v/v ≈ 1:1) mixtures were used for washing under ultrasonic treatment for 20 minutes in order to remove surfactants coated on the nanoparticle surfaces, the remaining sodiu m ions, as well as $BaCO_3$ impurities from the $BaTiO_3$ powders. The washed $BaTiO_3$ nanoparticles were re-dispersed in toluene. This sequence of re-dispersion in toluene and centrifuging to separate the solvent was repeated three times. Finally, the washed $BaTiO_3$ nanoparticles could be well dispersed in organic solvents. This procedure was sufficient to produce a dispersion of 20 nm diameter $BaTiO_3$ nanoparticles suspended in chlorobenzene with no additional surfactant in the solution.

4.3.3 Powder characterization

The as-prepared and heat-treated nanoparticles were analyzed by thermogravimetric analysis (TGA, METTLER TOLEDO TGA/DSC 1 Star System), Fourier transform infrared spectroscopy (FT-IR, FTS 175), X-ray diffraction (XRD, Siemens D5000, Cu$K\alpha$, 40kV, 40 mA), scanning electron microscopy (SEM, Quanta 400 FEG), high resolution transmission electron microscopy (HR-TEM, Tecnai F20), and Raman scattering (BRUKER RFS 100/S, 514.5 nm, 600 mW). Particle size distributions were calculated on a number basis using image analysis software (Scion Image Beta 4.0.2, Scion Corporation, Fredrick, MD). Particle morphology and size were determined using high resolution transmission electron microscopy and scanning electron microscopy. Phases present and other physical properties were determined using a variety of characterization techniques. X-ray diffraction (XRD) was used to determine the solid phases present. The diffracted Cu$K\alpha$ X-ray radiation (λ = 1.54178 Å) on the sample surface was collected using a continuous scanning at ~ 0.8°/min from 20° to 80°. Density measurements were performed using helium pycnometery (Multivolume Pycnometer 1305, Micromeritics, Norcross, GA). TEM analysis was performed using holey-carbon film on Cu grids (Electron Microscopy Sciences, Fort Washington, PA) as the sample holder. A single drop of dilute suspension was placed on each TEM grid. For FT-IR samples, 15 mg of $BaTiO_3$ powder was added to 285 mg of KBr powder and ground in a mortar and pestle to give a fine mixture. In order to evaluate the dielectric permittivity of $BaTiO_3$ nanoparticles the washed $BaTiO_3$ powder (with particle size 15 nm according to TEM data) was uniaxially pressed at 520 MPa (1.5 tons) into disks (6 mm in diameter, 0.6 mm thick). The disk surfaces were ground gently and a conductive silver paste was applied to the flat surfaces and fired in a vacuum oven at 120 °C for 8 h to assure that there was no remaining water in the sample. These disks were then filled with epoxy resin (EpoFix Resin UN-no.3082 and EpoFix hardener UN-no. 2259) to avoid penetration of ambient air during measurement. These epoxy-filled disks can be further heated to a temperature above about 100 °C to melt the epoxy resin so that it filled the spaces between the particles. The dielectric measurements were performed at room

temperature using a Solartron 1260 impedance analyzer with dielectric interface 1296.

4.4 Results and discussion

4.4.1 Preparation of oleate-modified $BaTiO_3$ crystallites with various sizes

The successful formation of $BaTiO_3$ nanoparticles is attributed to the modification of $Ti(O^iPr)_4$ to $Ti(O^iPr)_{4-x}(RCOO)_x$, a process comparable to the formation of the titanyl-acylate-type precursor which was formed by reacting $Ti(O^iPr)_4$ with acetic acid [139–142]. As reported in the literature, $Ti(O^iPr)_4$ can readily react with oleic acid to generate yellow oleic acid-titanium complexes $Ti(O^iPr)_{4-x}(C_{17}H_{33}COO)_x$ at 80 °C in which one or more isopropoxide groups are replaced with an oleate ligand with concomitant release of isopropyl alcohol (See Eq. 4.1) [143, 144].

The mechanism of formation of $Ti(O^iPr)_{4-x}(C_{17}H_{33}COO)_x$ was studied by FTIR spectroscopy. A doublet of stretching bands around 1500 cm^{-1} (ν_{as} (COO) at 1560 cm^{-1} and ν_s (COO) at 1440 cm^{-1}) that corresponds to bidentate oleate ligands ($C_{17}H_{33}COO^-$) linked to titanium is expected [145–148]. Figure 4.3 (a) and (b) show the FTIR spectra of pure oleic acid and the mixture of $Ti(O^iPr)_4$ (0.01 mol) and oleic acid (0.06 mol) after 1 hour at 80 °C, respectively. A characteristic C=O stretching band of oleic acid appears at 1710 cm^{-1} in Figure 4.3 (a). The decrease in intensity of the free C=O stretching band after adding $Ti(O^iPr)_4$ in Figure 4.3 (b) shows that oleic acid has reacted with $Ti(O^iPr)_4$. A new strong band appearing at ~ 1558 cm^{-1} is attributed to the asymmetric COO^- stretching vibration, indicating the coordination of oleic acid to titanium centers to form titanium oleate complexes by ligand substitution. The symmetric COO^- stretching band at ~ 1440 cm^{-1} is usually difficult to locate due to its overlap with C-H bending vibrations at 1467, 1450, and 1375 cm^{-1} (attributed to symmetric CH_2, asymmetric CH_3, and symmetric CH_3 in oleate, respectively [145]). Another characteristic C=O stretching vibration of isopropyl oleate at 1735 cm^{-1} also can be observed [146]. The by-product, isopropyl oleate, was generated either by nonhydrolytic elimination/condensation of unstable $Ti(O^iPr)_{4-x}(C_{17}H_{33}COO)_x$, which can remove some of the oleate and isopropoxide ligands together, or by a slow esterification reaction between the reactant oleic acid and the released isopropyl alcohol. Figure 4.3 (c) shows the FTIR spectrum of a methanol-wash precipitate from the reaction mixture of oleic acid with $Ti(O^iPr)_4$ after adding Tetramethylammoniumhydroxid (TMAH), used as a precipitating agent. As a result, the asymmetric and symmetric COO^- stretching bands at ~ 1558 cm^{-1} and ~ 1435 cm^{-1} can be clearly observed after the complete removal of any unreacted oleic acid and isopropyl oleate from the reaction system. In our case, the frequency separation ($\triangle\ \nu < 130\ cm^{-1}$) between the ν_{as} (COO^-) at

1558 cm^{-1} and ν_s (COO^-) at 1435 cm^{-1} suggests that $C_{17}H_{33}COO^-$ acts as a bidentate chelating ligand [145, 149].

In the "organosol", Ba^{2+} ions were distributed homogenously over the titanium oleate precursor matrix so that Ba^{2+} ions are surrounded by many oxygen ions in octahedral coordination to titanium in addition to the two oleate ligands belonging to them. The mixing of the above precursors with NaOH causes formation of a stabilized complex of titanium $[Ti(OH)_6]^{2-}$ (See Eq. 4.3) that can react with Ba^{2+} ions according to Eq. 4.4. We believe that the soluble Ba^{2+} ions cover the surface of the $[Ti(OH)_6]^{2-}$ and are then incorporated into the titanium structure to counterbalance the negative charge, causing the rupture of Ti-O-Ti and formation of Ti-O-Ba bonds [150]. Thereafter, the precipitates will grow in a ripening process. At first, optimum conditions for formation of $BaTiO_3$ using the "organosol" route were screened at various reaction temperatures at 25 °C, 40 °C, 60 °C, 80 °C and 100 °C in vacuum, denoted as sample A1(25 °C), A1(40 °C), A1(60 °C), A1(80 °C), and A1(100 °C), respectively. XRD patterns (Figure 4.4 (a)) confirm that the $BaTiO_3$ nanoparticles prepared at all temperatures in vacuum are in the perovskite phase. Even the particles prepared at room temperature are crystalline, however with formation of a $BaCO_3$ impurity phase. It was also observed that the diffraction peak intensities do not change markedly with elevation of the reaction temperatures from 40 to 80 °C. For samples prepared at temperatures above 100 °C the crystallinity was further improved. Simultaneously, the (111) peak shifts to higher 2θ. Figure 4.4 (b) illustrates the relation between the reaction temperatures, lattice constant a, and the crystallite size, d. The latter was estimated from the width of the diffraction peaks using the Scherrer equation,

$$\triangle (2\theta) = \frac{K\lambda}{d cos\theta} \tag{4.5}$$

where $\triangle(2\theta)$ is full width at half maximum (FWHM) for the peak situated at 2θ angle, λ= 1.54056 Å is the wave length of Cu$K\alpha$ radiation, and K is the Scherrer constant. For spherical particles with cubic symmetry K = 0.9 [151]. Intriguingly, both the crystallite size and the lattice parameter of the $BaTiO_3$ powders first expand as the reaction temperature is increased to 40 °C and then shrink with increasing reaction temperatures up to 100 °C.

It is well known that many factors, such as defects and impurities in the grain lattice of powders can affect the lattice parameter of the powder. Unfortunately, unavoidably the hydroxyl (OH^-) defects often exist in the lattice of $BaTiO_3$ chemically prepared at very low temperature [152]. Thus, this abnormal crystallographic feature of the as-prepared $BaTiO_3$ particles is assumed to result from lattice defects, due to OH^- incorporation in the unit cell. While the OH^- content is not concluded to be responsible entirely for the cubic structure of

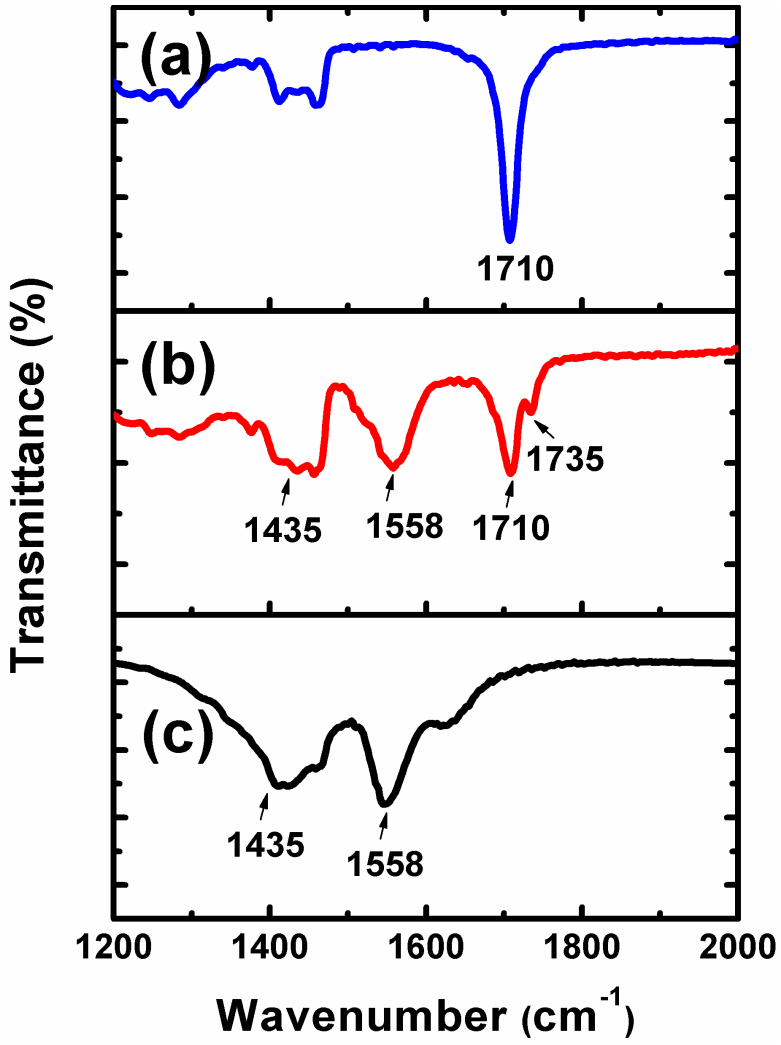

Figure 4.3: FTIR spectra of (a) pure oleic acid; (b) a mixture of oleic acid and $Ti(O^iPr)_4$ after treatment at 80 °C (Oleic acid/$Ti(O^iPr)_4$ = 6); (c) a methanol-wash precipitate from the same mixture after further TMAH treatment.

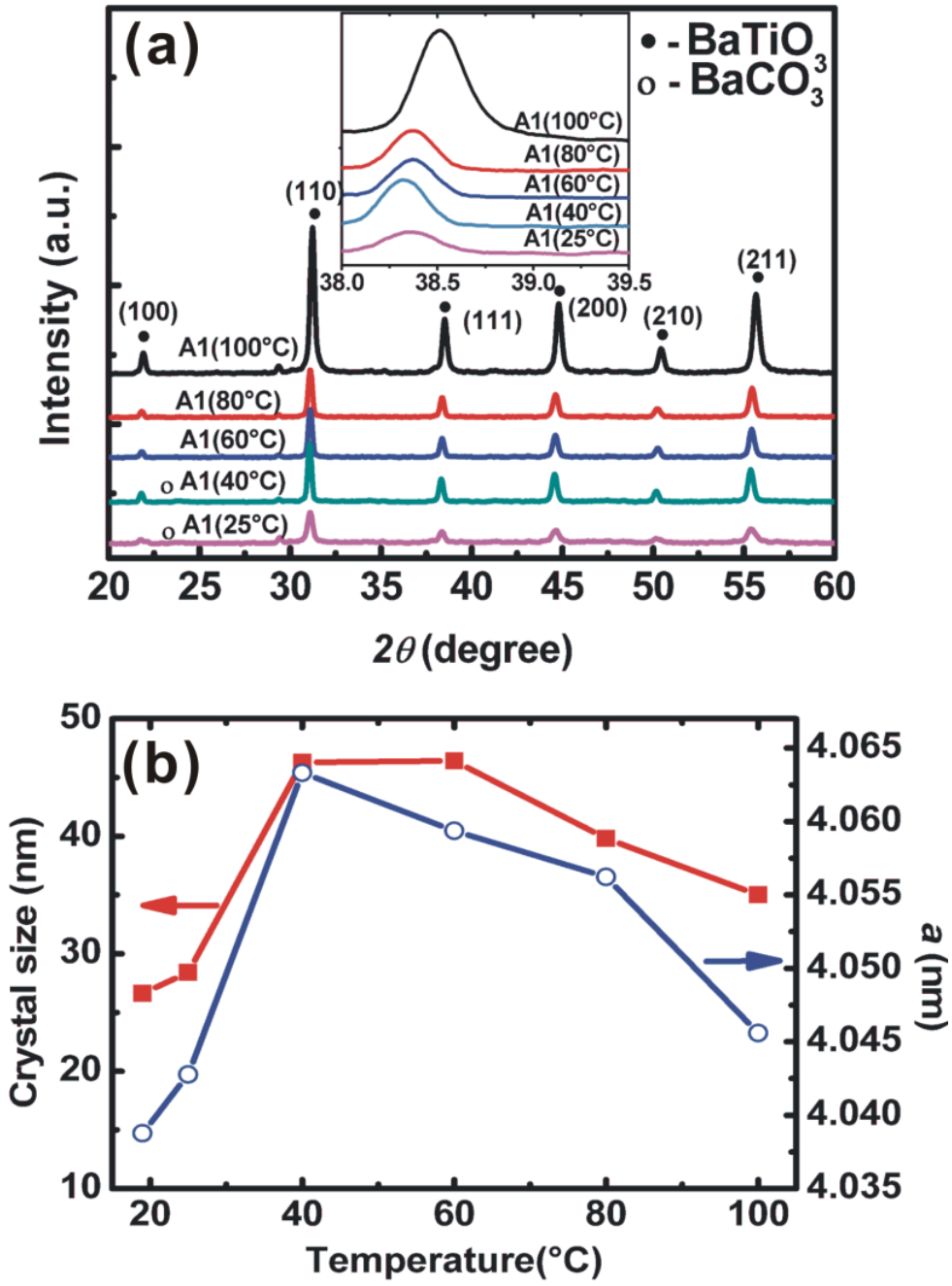

Figure 4.4: (a) XRD patterns of A1(25 °C), A1(40 °C), A1(60 °C), A1(80 °C), and A1(100 °C) samples (Inset: wide-angle XRD patterns for $BaTiO_3$ (111) peaks), and (b) crystal size and lattice parameter vs. the reaction temperature.

ultrafine $BaTiO_3$, the defects are likely to strongly affect the measured cubic lattice parameter. Reducing such kind of defects in the lattice remains a challenge in our $BaTiO_3$ synthesis. A second explanation can be found in an increased influence of surface tension on the lattice parameter for nano-sized particles [153]. A high contractive surface tension will lead to a compressive hydrostatic pressure and thus to a reduced lattice constant independent of the chemical route and temperature treatment that leads to grain formation [154].

The as-prepared $BaTiO_3$ nanoparticles are directly coated with oleic acid after synthesis. The hydrophobic tails of oleic acid are directed outward, thereby forming oleophilic layers that greatly enhance the dispersion of $BaTiO_3$ nanoparticles in organic solvents such as tetrahydrofuran, chlorobenzene, and n-octane. In order to understand the adsorption mechanism of the oleic acid on the surface of $BaTiO_3$ nanoparticles, FT-IR measurements were carried out on the oleate and as-prepared $BaTiO_3$ nanoparticles (Figure 4.5 (c)). In the infrared spectrum of the oleate the two sharp bands observed at 2924 and 2853 cm^{-1} are attributed to the C-H symmetric and asymmetric stretch vibrations of the $-CH_2-$ and $-CH_3$ groups in the hydrophobic chains of the oleic acid molecules. As mentioned previously, the C=O stretch band of the carboxyl group, which is present at 1710 cm^{-1} in the spectrum of the pure liquid oleic acid, is absent in the oleate. At the same time, two new bands appear at 1407 and 1545 cm^{-1}, which are characteristic of the COO^- symmetric (ν_s (COO^-)) and asymmetric stretch (ν_{as} (COO^-)) vibrations. For the spectrum representing the as-prepared $BaTiO_3$ nanoparticles, the bands occur at 2923, 2853, 1424 and 1563 cm^{-1}, showing that oleate molecules are chemically bound to the surface of the $BaTiO_3$ nanoparticles. The difference between ν_{as} (COO^-) and ν_s (COO^-) is 138 cm^{-1}, which is smaller than the difference between them for free carboxylate ions (ca. 188 cm^{-1}) [145, 148]. Therefore we conclude that the oleate is bonded to the $BaTiO_3$ nanoparticles through chelating bidentate-type bonding.

4.4.2 Powder Characterization

In addition to the investigation of the $BaTiO_3$ nanopowders prepared at different reaction temperatures, the effects of washing and/or calcination on the particle properties, such as particle size distribution, particle shape, and/or specific surface area were studied. In particular, the sample A1 (25 °C) was treated by calcinations and/or by a two-step process of acid-treatment and subsequent calcination. The treated samples were denoted as A2, A3, B1, B2, and B3, respectively:

A1 (25 °C): BTO prepared at 25 °C,
A2 (550 °C): sample A1 calcined at 550 °C,
A3 (1050 °C): sample A1 calcined at 1050 °C;

B1: washed sample A1,

B2 (550 °C): sample B1 calcined at 550 °C,

B3 (1200 °C): sample B1 calcined at 1200 °C.

Some properties of as-prepared $BaTiO_3$ and treated $BaTiO_3$ powders are given in Table 4.1. Parameters of XRD patterns, and IR and Raman spectra are summarized in Table 4.2. The typical XRD patterns of the sample A1 (25 °C) and sample B1 are shown in Figure 4.5 (a). All the diffraction peaks can be indexed to the cubic perovskite structure of BTO in good agreement with the literature value (cubic, JCPDS No.31-174). Strong and sharp peaks suggest that BTO is highly crystalline. Besides, two small peaks corresponding to $BaCO_3$ phase (orthorhombic, JCPDS No. 5-378) were observed at 24 ° and 29 ° in the as-prepared powders. XRD data reveal that the washing of the as-prepared samples in diluted acetic acid solution results in the pure $BaTiO_3$ phase. According to the EDX measurements the Ba/Ti molar ratio is ~ 1.07 and 0.80 in sample A1 and B1, respectively. The barium deficiency is caused by the acetic acid treatments. At the same time, the lattice parameter (~ 4.04 $\AA$) and FWHM of the (200)-peak (~ 4.7×10^{-3} rad) obtained from XRD data are the same before and after the acetic acid washing. These results suggest that only Ba^{2+} ions near the surface of the particles were lost by the acetic acid washing treatment.

The structure and particle size of B1 and B2 samples were also investigated by HRTEM (Figures 4.6 and 4.7). Figure 4.6 (a) shows $BaTiO_3$ nanocrystals with size around 13 nm. The corresponding fast Fourier transform (FFT) patterns (Figures 4.6 (b, c)) could be indexed according to the cubic $BaTiO_3$ structure. The observed lattice spacing of 0.284 nm can be assigned to the (011) series, which gives the cubic unit cell size a = 4.02 $\AA$. This value is in good agreement with a = 4.04 $\AA$ determined by XRD (Table 4.1). Moreover, corresponding electron diffraction shows a distinct ring pattern and can be completely indexed in the $BaTiO_3$ cubic *Pm*3*m* space group (Figures 4.6 (d) and 4.7 (d)). For the powder calcined at 550 °C HRTEM shows $BaTiO_3$ nanocrystals of about 50 nm in diameter (Figure 4.7 (a)). As can be seen from HRTEM and HAADF-STEM (High-Angular Annular Dark Field-Scanning Transmission Electron Microscopy) images of sample B2 (Figure 4.7 (b, c)) the particles are polycrystalline and consist of small native particles combined into small agglomerates. This was also confirmed by SEM studies (Figure 4.8). To investigate the thermal behaviour of the as-prepared $BaTiO_3$ nanoparticles TGA-DSC measurements were performed. Representative results are shown in Figure 4.6 (b). The total weight loss recorded between 25 and 1100 °C was ~ 57 wt %. It consists of three main steps. The first step (up to 300 °C) can be attributed to the endothermic desorption of physically adsorbed water as well as solvents. The second step between 300 and 480 °C is characterized by the strongest weight loss and is due to the

Sample	Ba:Ti molar ratio	$[Na^+]$	[C]	Average particle size [nm]		Lattice parameters [$\AA$]		FWHM (200) [10^{-3} rad]	Shape Control	
				d_{SEM}	d_{XRD}	a	c			
A1(25 °C) (as-prepared BTO)	1.07	31%	37.2%	–	26.6	4.04		4.74		–
A2 (550 °C)	0.96	8.6%	5.2%	53	44.6	4.01		5.49	Very good	Spherical
A3 (1050 °C)	1.03	0.1%	No	488	–	3.99	4.03	–		Cubic
B1 (washed BTO)	0.8	No	No	19.5	29.5	4.04		4.78	Not good	Spherical
B2 (550 °C)	0.83			100	46.6	4.02		5.01		Irregular
B3 (1200 °C)	0.95			175	–	4.00	4.03	–		Irregular

Table 4.1: Structural Properties of the $BaTiO_3$ powders.

Method	A1 (25 °C)	B1		Assignments	Ref.
IR	Wavenumber in cm^{-1}			Vibrational modes	
	572	572		Ti–O	[155]
	694	694	Very weak	$\nu(CO_3^{2-})$	[155]
	858	859			
	1059	1059			
	1639	1631			
	1445	1441			
	1424	1423		$\nu(COO^-)$	[145, 149]
	1563	1562			
	2853	2852		$\nu(CH_2)$	[145, 149]
	2923	2922			
	3434	3434		$\nu(OH^-)$	[156, 157]
XRD	2θ in degrees			Main peak	
	24	No		(111) assigned to $BaCO_3$	Orthorhombic[a]
	31	31		(110) assigned to $BaTiO_3$	Cubic[b] $Pm\bar{3}m$
Raman	Raman shift in cm^{-1}			Mode symmetries	
	-	183		A_1(TO), E(LO)	Tetragonal $Pm4m$ [158]
		301		B_1, E(TO + LO)	
		520		A_1, E(TO)	
		725		A_1, E(LO)	
		1060		$BaCO_3$	[155, 159]

[a] JCPDS no. 5-378. [b] JCPDS no.31-174.

Table 4.2: Some characteristic features of IR, XRD, and Raman-spectra of the $BaTiO_3$ nanopowders.

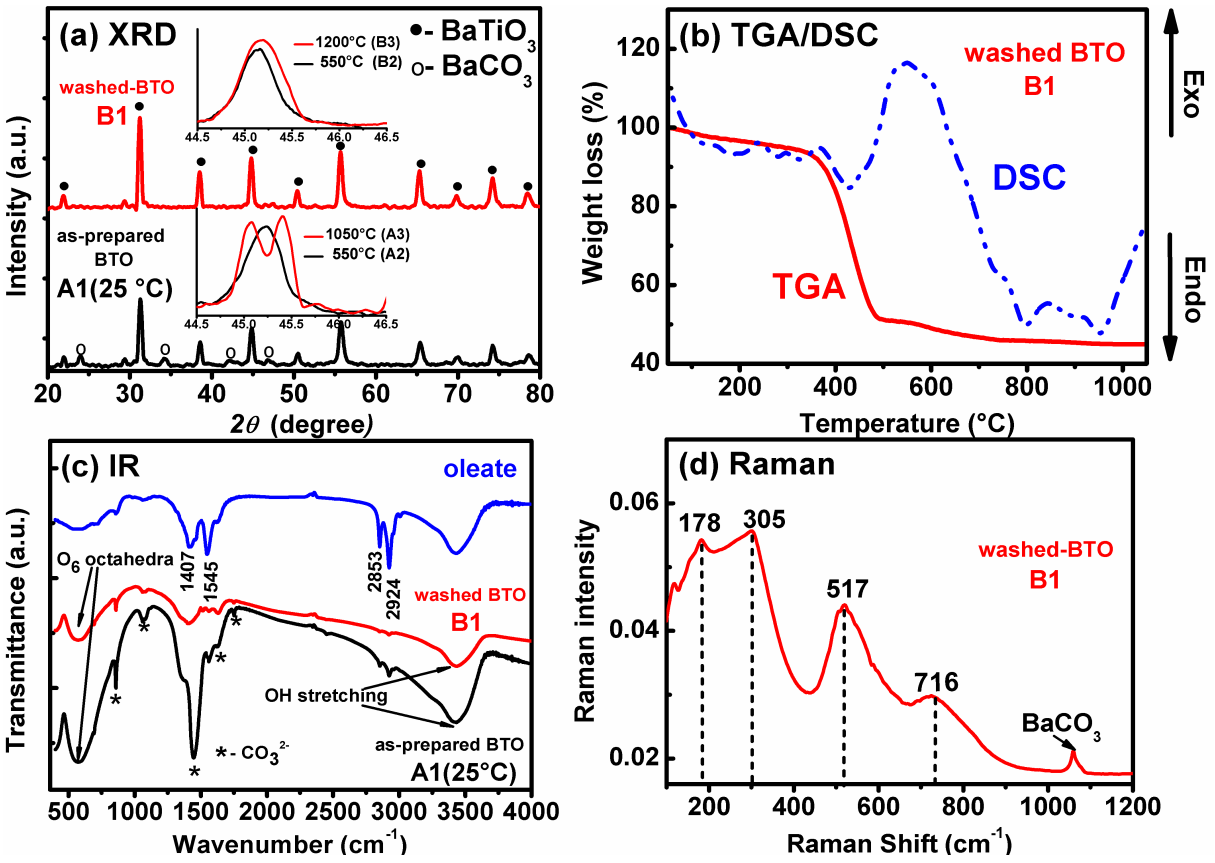

Figure 4.5: (a) XRD spectra, (b) TGA/DSC measurements, (c) FTIR, and (d) Raman spectra of as-prepared A1 and washed B1 samples. Inset to (a) shows the (200) XRD peak of the $BaTiO_3$ powders directly calcined at 550 and 1050 °C (the upper panel) and washed and calcined at 550 and 1200 °C (the bottom panel).

burning out of the oleate attached to the particles surface. The third step, for 480-800 °C, can be attributed to the loss of chemically bonded OH- groups as well as partially to the loss of carbonic residues [160, 161]. This interpretation is supported by the presence of a broad exothermic peak between 410 °C and 800 °C in the DSC curve indicating the combustion of organic residues in at least one exothermic reaction. Finally, the weight loss above 800 °C indicates CO_2 release during the endothermic decomposition of the $BaCO_3$ by-product.

The presence of the internal OH^- defects mentioned above and impurity $BaCO_3$ in as-prepared $BaTiO_3$ nanoparticles was verified by FT-IR studies (Figure 4.5 (c)), which are consistent with the results of TGA-DSC analysis. A broad band in the IR spectra ranging from 2700 to 3600 cm^{-1} suggests the presence of considerable amounts of H_2O and OH^- in the particles [156, 157]. While a sharp band at 1445 cm^{-1} corresponds to the stretching vibration of CO_3^{2-}, which comes from the impurity phase of $BaCO_3$ [156]. The sharp band observed at 572 cm^{-1} is assigned to the Ti-O vibration of $BaTiO_3$. For the washed powder (B1) the bands representing CO_3^{2-} groups and organic species decreased significantly and were almost invisible in the IR spectrum. Thus, according to the FT-IR data washing of as-prepared $BaTiO_3$ in dilute acetic acid leads to the liberation of the impurities from the $BaTiO_3$ nanoparticles.

In comparison to XRD, Raman spectroscopy is a more sensitive technique to probe the small tetragonal distortion in the local crystal structure. Figure 4.5 (d) gives a Raman spectrum of the washed $BaTiO_3$ sample at room temperature. The peak centred at 1060 cm^{-1} corresponds to residual $BaCO_3$ phase [155, 159] in agreement with the IR data. Even though a perfect cubic symmetry forbids any Raman activity, the Raman spectrum in the paraelectric phase of bulk $BaTiO_3$ with broad bands centred at ~ 285 and 520 cm^{-1} has been reported at temperatures up to 570 K [162]. It is considered as an indication of a strong local disorder due to random displacement of Ti^{4+} ions at high temperatures. In our case, in addition to these modes, peaks around 178, 305, and 716 cm^{-1} are observed, which are typical for tetragonal $BaTiO_3$, but have also been reported for $BaTiO_3$ nanoparticles at room temperature [158]. This indicates an acentric local structure (i.e., the local tetragonal symmetry) for the nanoparticles of apparent macroscopic cubic structure according to XRD.

4.4.3 Calcination kinetics

SEM micrographs of as-prepared $BaTiO_3$ and treated $BaTiO_3$ nanoparticles are presented in Figure 4.8. It is clearly visible that the as-prepared powder mainly consists of agglomerates of primary particles with diameters of less than 20 nm which aggregate into polydispersed clusters. The micrographs of the washed as well as washed and calcined samples (Figure 4.8 B1-B3 and Figure 4.9 B3) also show strongly agglomerated irregular nanoparticles with neck formation and coalescence between the particles. However, the sample A1 (25 °C) di-

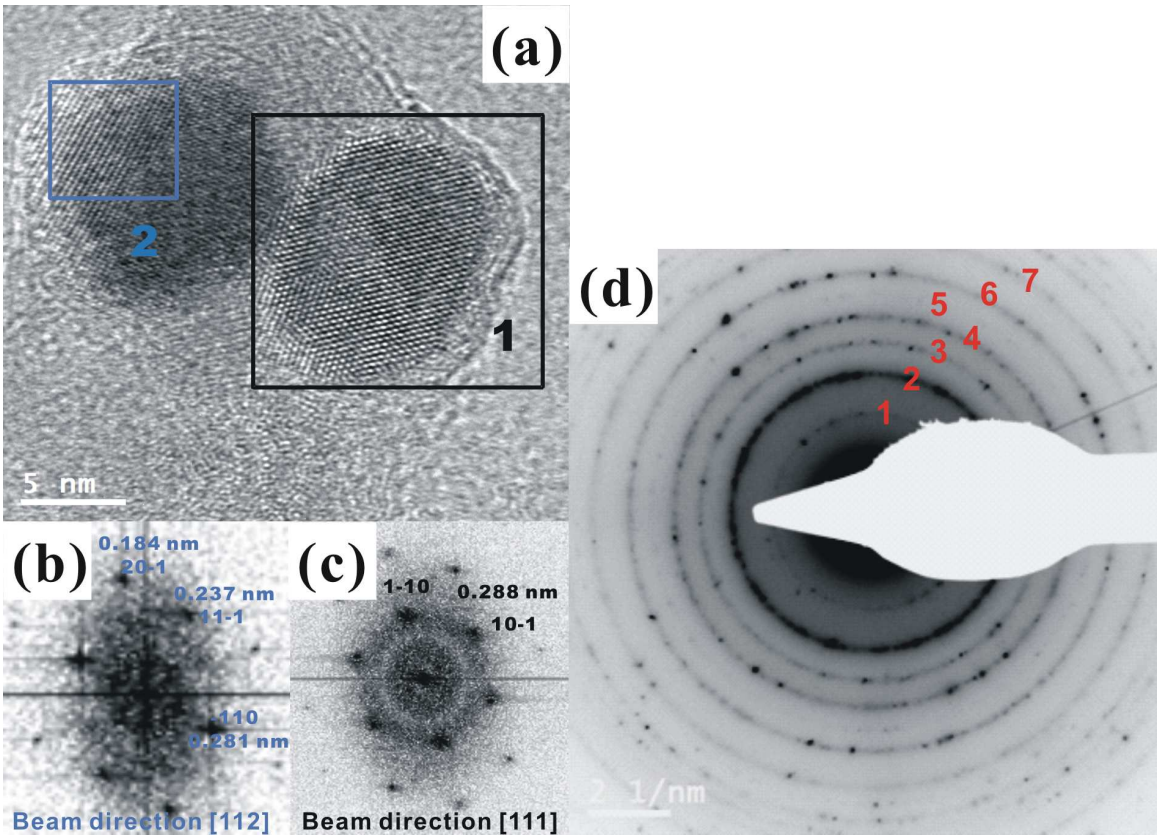

Figure 4.6: (a) A High-resolution TEM image of two isolated $BaTiO_3$ nanocrystals (sample B1) and the corresponding FFT patterns (b) and (c), showing the single cubic phase, and (d) the corresponding electron diffraction.

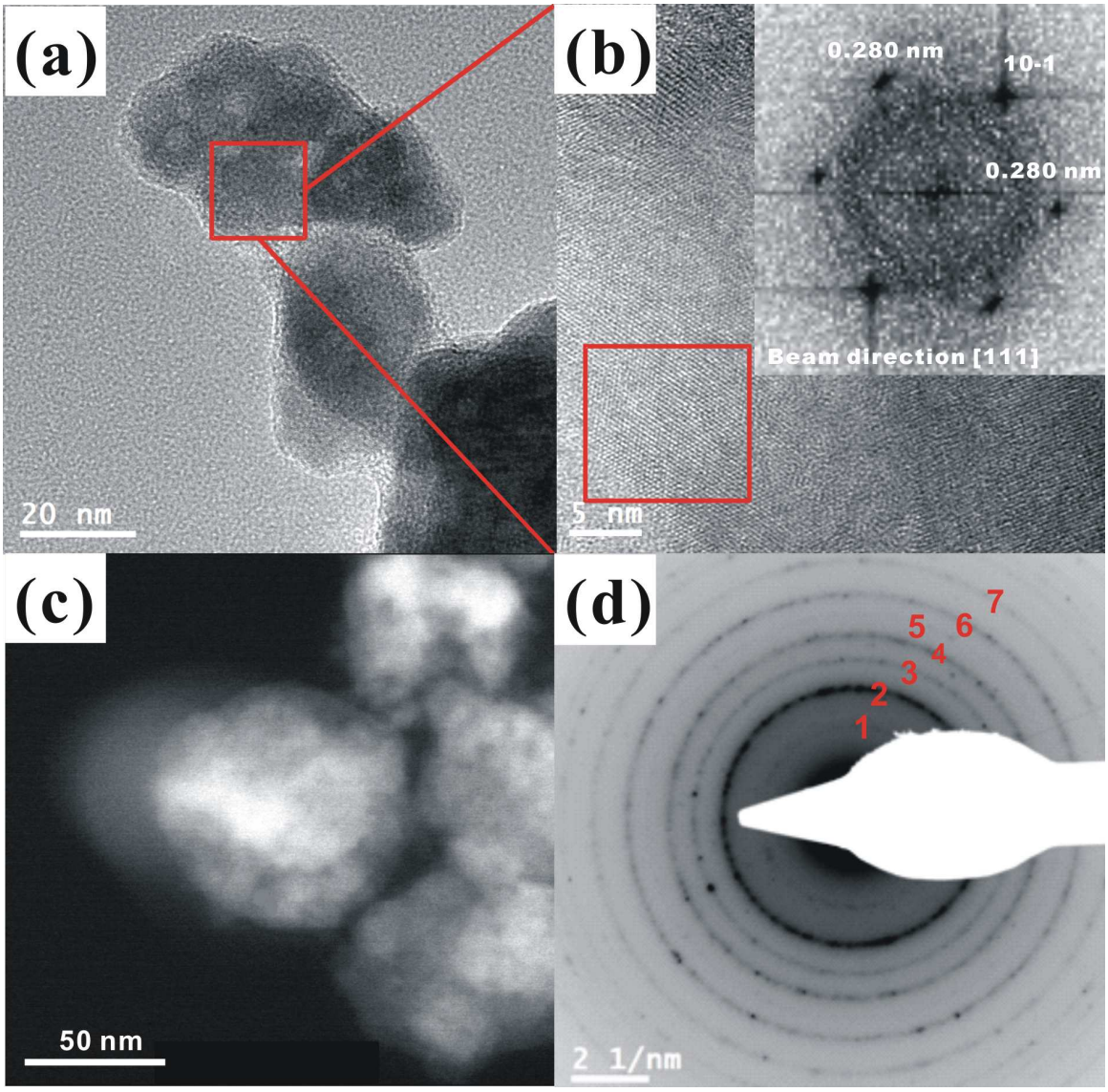

Figure 4.7: (a) High-resolution TEM images of sample B2 and (b) the corresponding FFT pattern, (c) HAADF-STEM (d) the corresponding electron diffraction.

rectly calcined at 550 °C exhibits quasi-spherical nearly monodisperse particles. Although the sample A2 showed a certain degree of agglomeration, no pronounced neck formation or coalescence phenomena were observed.

The SEM images reveal a reduction of the average particle size for the directly calcined sample A2 in comparison to that of the washed and calcined sample B2. Presence of carbon on the particle surfaces of the sample A2 is found in the EDX spectra. This carbon seems to originate from incomplete decomposition of oleate surfactants adsorbed on the $BaTiO_3$ nanoparticles. A decomposition of the organic citrate with formation of carbon species has often been observed for the synthesis of nanoparticles using organic percursors [163–165]. Such a layer encapsulates or isolates the nanoparticles and can prevent their growth [163]. Similarly in our case the carbon layers surrounding the $BaTiO_3$ particles reduce their growth and coalescence for the non-washed samples (Figure 4.2 (a)) yielding a smaller particle size and a narrower size distribution compared to the washed samples.

When the non-washed $BaTiO_3$ powder was calcined at 1050 °C (sample A3) both particle growth and the conversion of existing spheres to cubes occurred, resulting in the formation of significantly larger particles. The particles of cubic or brick shape with sizes of 1~2 μm were observed (Figures 4.8 & 4.9, A3). This is in agreement with XRD, where a well-defined splitting of the (002) and (200/020) peaks characteristic of tetragonal $BaTiO_3$ was observed (inset of Figure 4.5 (a)). This type of grain growth kinetics is significantly different from the "normal" as seen in Figures 4.8, 4.9 and 4.10. A cuboidal grain shape has been reported for thin film $BaTiO_3$ synthesis on metallic titanium substrates via the glycothermal route [166]. Apparently, the organic component on the grain surface facilitates cube formation. Thermodynamics and growth kinetics jointly determine the shape of a nanocrystal [47, 167, 168]. Different relative specific surface energies associated with the facets of the crystal yield the driving force for crystal growth while growth kinetics determine the final crystal shape. According to Refs. [167] and [169], the assembly of $[BO_6]$ growth units is different at the $\{001\}_{cub}$, $\{110\}_{cub}$ and $\{111\}_{cub}$ interfaces during crystal growth for the perovskite structure ABO_3. The washed samples (B-series) appear to exhibit regular crystal growth of approximately equal growth rates of $\{001\}_{cub}$, and $\{111\}_{cub}$ facets yielding close to spherical particles bounded by a corresponding crystal facet area. The residues of the organic synthesis process induce preferred growth of the {001}cub family of surfaces (A in Figure 4.10). The ledges (terminology according to Ref. [170]) of crystal growth (C in Figure 4.10) appear to lie along $<001>_{cub}$ directions. In the fully calcined non-washed samples $\{111\}_{cub}$ facets (B in Figure 4.10) are seldom found. At certain instances terraces of crystal growth are seen (D in Figure 4.10). As expected for a multigrain system growth conditions change during crystal growth yielding growth sectors of Figure 4.9, A3 illustrated in Figure 4.9 (b) [170].

The $\{111\}_{cub}$ and $\{001\}_{cub}$ faces of the perovskite structure differ significantly. The latter contain cations as well as anions in each layer of growth, namely alternating TiO_2 and BaO units. The layer is thus always charge neutral. The former displays alternating termination in charged layers, namely an oxide or a mixed cation layer. Thus, the chemical species adhering to these two types of faces may under certain circumstances be quite different. This apparently happens here in an organic environment during calcination. The exact chemistry of this process remains an open question at this point.

4.4.4 Nanorods

In the samples A2 nanorods with variable aspect ratios, nanowires, or the mixture of nanosheets, and nanorods which have smooth surface develop (Figure 4.11 (a)) beside the spherical $BaTiO_3$ particles. The volume fraction of these one-dimensional nanostructures estimated from SEM data was ~ 5 %. The diameters of the nanorods vary from 20 to 60 nm, while the lengths can reach several microns. According to Refs. [171] and [172] these nanorods can be associated with sodium titanate, $Na_2Ti_6O_{13}$. The EDS spectra (Figure 4.11 (b)) clearly show that the rods containe Na and Ti. The observed Ba peak might stem from nearby or underlying particles. Ba^{2+} ions could also be incorporated into the sodium titanate structure. The unwanted nanorods could be completely removed by diluted acetic acid.

4.4.5 Dispersion properties in organic solvents

Often commercial $BaTiO_3$ nanoparticles are aggregated and show poor dispersion capabilities in most organic media. This limits the use of low-cost, solution processing techniques, such as spin coating, spraying, and evaporative self assembly [173]. In order to identify the solventphilic properties of our pure $BaTiO_3$ nanoparticles which have been washed with 0.2 % acetic acid, the washed $BaTiO_3$ nanoparticles were dispersed in binary solvents of water and chlorobenzene. Note that chlorobenzene has a higher density and forms a bottom layer in a beaker, and that the water phase stays above chlorobenzene. Figure 4.12 (a) shows that the washed $BaTiO_3$ still remains stable in the organic phase. It is possible to create an amorphous inorganic titanium shell around $BaTiO_3$ core during washing [69, 174]. The washed $BaTiO_3$ still maintains the hydrophobic properties. In addition to chlorobenzene, organic solvents with low polarity such as benzyl alcohol, toluene, DMF and THF were also found to be good dispersion media for the washed $BaTiO_3$ nanoparticles (Figure 4.12 (b-f)). Although the dispersion stability of the washed $BaTiO_3$ nanoparticles is good in organic solvents, however, there are large difficulties in re-dispersing them into the original solvents near to their primary particle size once dried. The nanoparticles strongly aggregated when collected as dried powder.

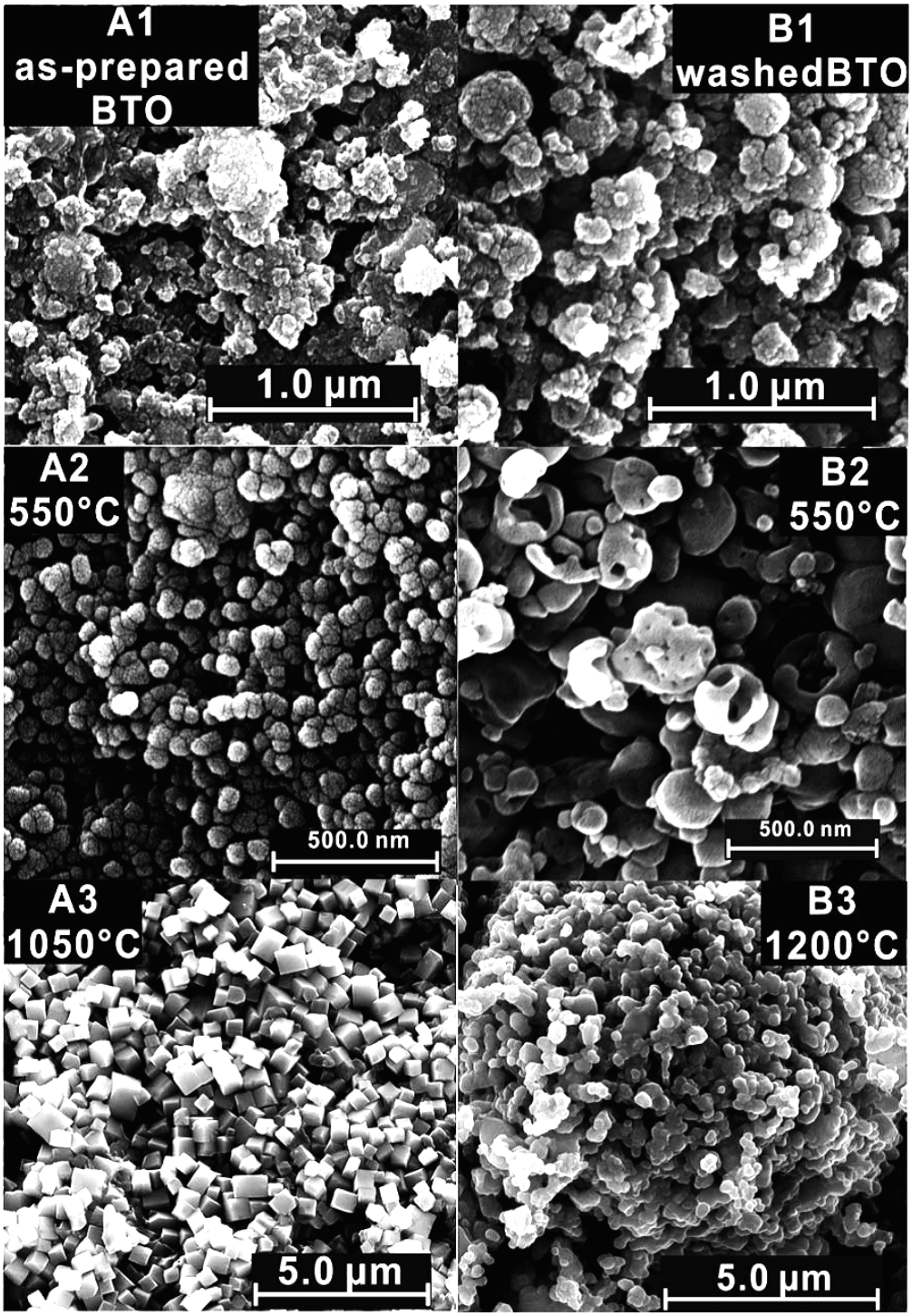

Figure 4.8: Effect of acid washing and thermal treatment on crystal morphology. SEM microphotographs from samples: A1 (25 °C), A2 (550 °C), and A3 (1050 °C); B1 (washed sample A1), B2 (washed and calcined at 550 °C), and B3 (washed and calcined at 1200 °C).

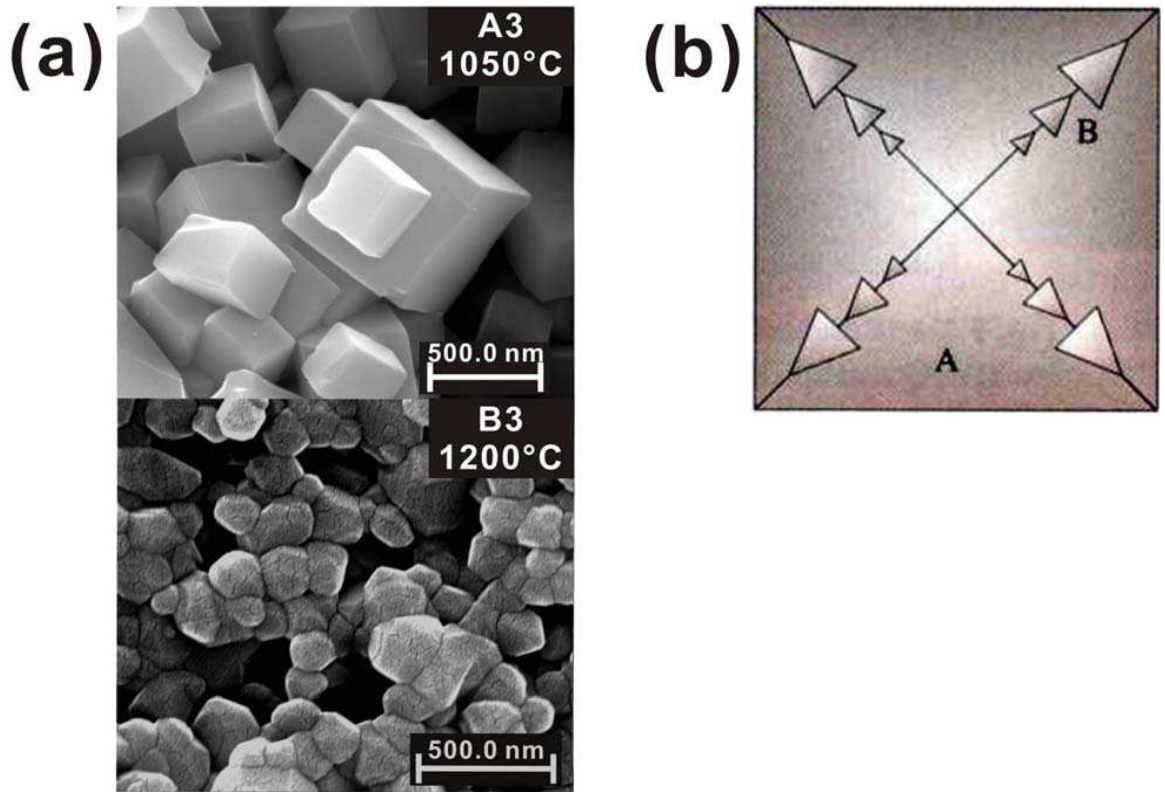

Figure 4.9: (a) SEM microphotographs from sample A3 (1050 °C) and B3 (1200 °C), (b) Illustration of intermittent growth sectors indicating repeated changes in growth conditions as visible on the cuboids of sample A3. ©Springer [28].

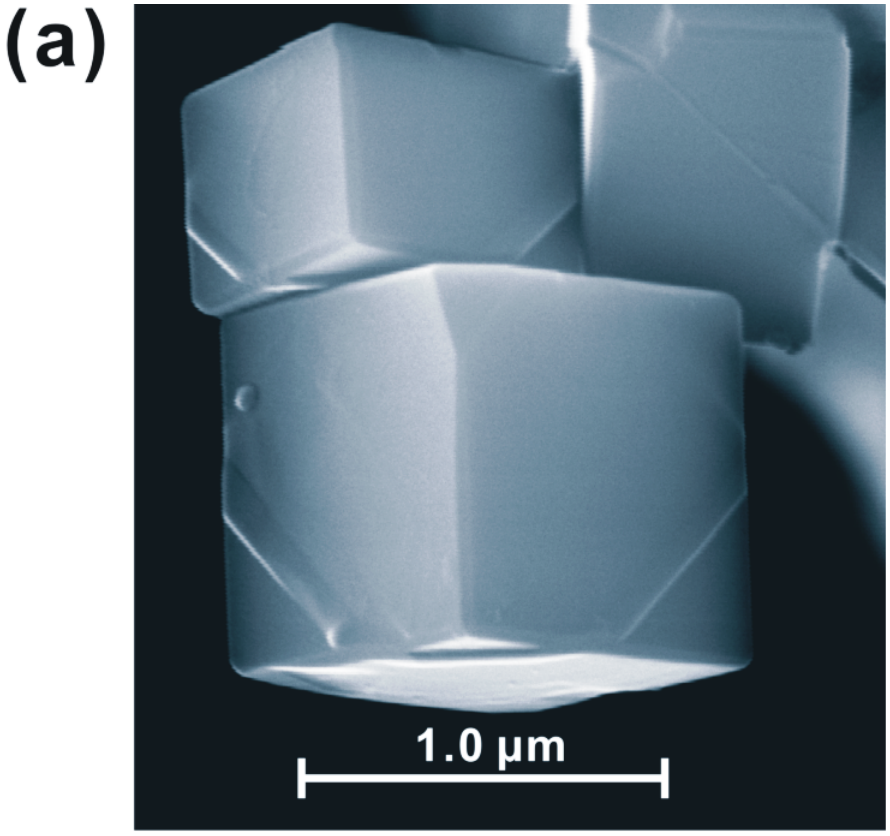

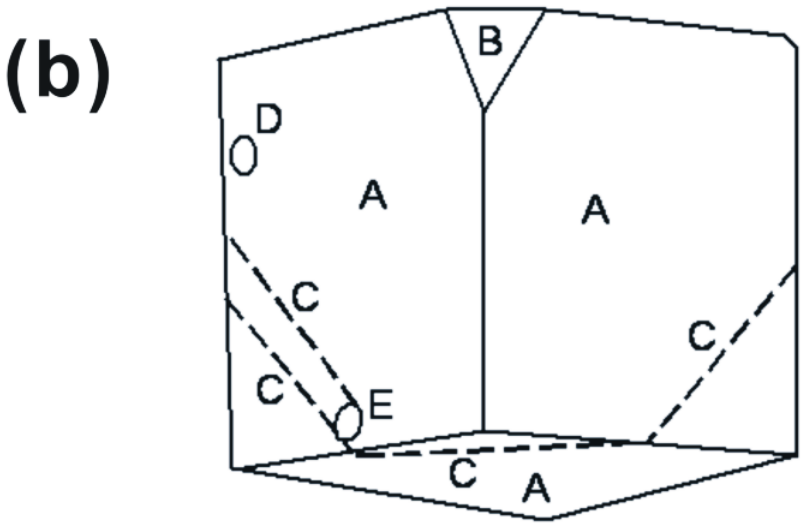

Figure 4.10: (a) SEM microphotograph of two grains in a sample A3 exhibiting growth marks, (b) corresponding sketch: A 100-face, B 111-face, C 110-groth ledge, D terrace seed, E terrace (or hole) stopping (or generating) growth ledges.

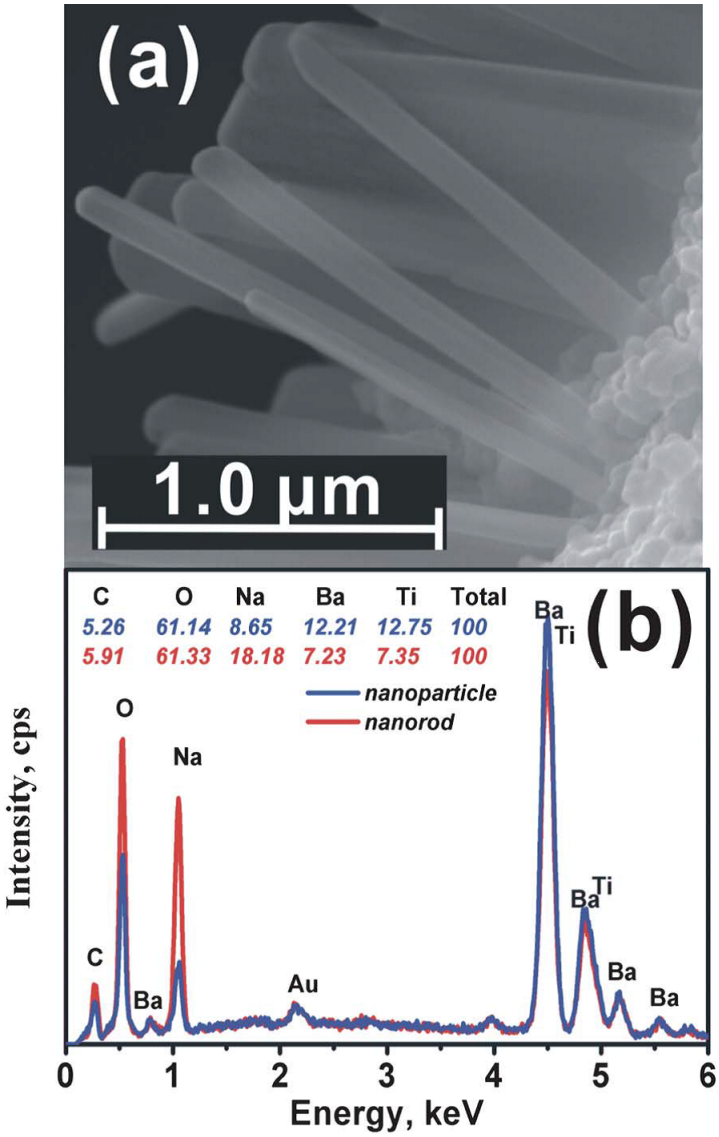

Figure 4.11: (a) SEM microphotograph of one-dimensional nanostructures in sample A2, (b) corresponding EDX spectra measured for spherical particles and nanorods.

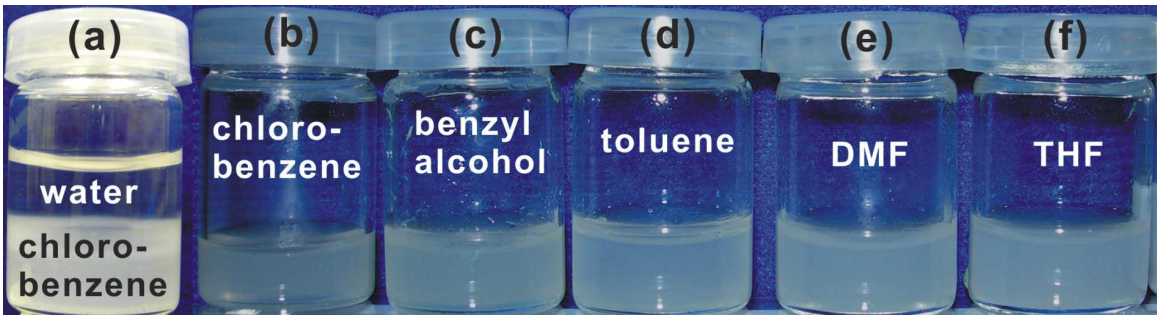

Figure 4.12: (a) Dispersion of washed $BaTiO_3$ nanoparticels in a two-phase solvent, the bottom layer of which is chlorobenzene and the upper layer is water. Good dispersion of washed $BaTiO_3$ nanoparticles in organic solvents: (b) chlorobenzene, (c) benzyl alcohol, (d) toluene, (e) dimethylformamide (DMF), (f) tetrahydrofuran (THF).

4.4.6 Dielectric properties

It is well known that measurement of the dielectric permittivity of powders is not straightforward. In particular, moisture absorption from ambient air makes test conditions hard to control. Several methods have been employed to characterize ultrafine $BaTiO_3$ particles, e.g. Wakino et al. reported on dielectric measurements of the powders using pressed compact bodies [175], and Wada et al. used powder dielectric measurements in suspension [176]. We used a modified pressed powder method employing an epoxy resin matrix.

Figure 4.13 (a) shows the frequency dependences of the dielectric permittivity and loss tangent measured at room temperature for two $BaTiO_3$ samples: the compacted powder and compacted powder filled with an epoxy resin. At a frequency of 1MHz both samples have comparable values of the dielectric permittivity $\varepsilon_{eff} \approx 30$ and $\tan\delta \approx 0.02$. As frequency decreases the barely compacted powder shows a substantially stronger increase of both dielectric permittivity and loss than the sample prepared with the epoxy. Such behavior is most probably related to larger contribution from the conductivity, which is inverse proportional to the probing frequency. Water from ambient air might enter the pressed powder providing overlapping water layers, which surrounds the nanoparticles and yields paths for charge carriers [177]. On the contrary, embedding the evacuated specimens in epoxy resin prevents absorption of moisture from the ambient. Comparing the density of the pressed samples with the theoretical density of $BaTiO_3$ we estimated the volume fraction of $BaTiO_3$ powder, $\alpha \sim 0.53$, which was calculated from the weight of the pressed $BaTiO_3$ powder disk, the theoretical density of $BaTiO_3$, and the geometry of the disk. Thus, we can consider our samples as composites consisting of $BaTiO_3$ nanoparticles and surrounding medium (air or epoxy). To evaluate the dielectric permittivity of $BaTiO_3$ nanoparticles from the measured effective permittivity, ε_{eff}, of the composites we apply several models, which are often used to calculated the dielectric

permittivity of heterogeneous dielectric:

Logarithm model:[178]

$$ln\varepsilon_{eff} = \alpha ln\varepsilon_1 + (1-\alpha)ln\varepsilon_2 \tag{4.6}$$

Maxwell-Garnett model:[179]

$$\frac{\varepsilon_{eff}-\varepsilon_1}{\varepsilon_{eff}+2\varepsilon_1} = (1-\alpha)\frac{\varepsilon_2-\varepsilon_1}{\varepsilon_2+2\varepsilon_1} \tag{4.7}$$

Bruggemann model:[180]

$$(1-\alpha)\frac{\varepsilon_{eff}-\varepsilon_2}{\varepsilon_2+2\varepsilon_{eff}} + \alpha\frac{\varepsilon_{eff}-\varepsilon_1}{\varepsilon_2+2\varepsilon_{eff}} = 0 \tag{4.8}$$

Here ε_1 and are ε_2 the dielectric permittivity of $BaTiO_3$ particles and medium (air or epoxy), respectively. The used epoxy resin has a dielectric permittivity ε_2 = 4.7 at 1 MHz and for air ε_2 = 1 was taken. Fig. 4.13 (b) shows values of ε_1 calculated according the aforementioned models. The logarithm model (Eq. 4.6) provides very different values for the samples with and without epoxy and seemingly is not applicable in our case. Maxwell-Garnett (Eq. 4.7) and Bruggemann (Eq. 4.8) models are more relevant yielding for the sample with epoxy ε_1 = 54 and 78, respectively. The values of the dielectric permittivity estimated from the pressed powder are 18-20 % larger. The discrepancy might be the result of an inaccurate estimation of sample volume, some compacting of the sample with epoxy resin during the de-aeration process. It may also indicate that the additional contribution from the conductivity into measured ε_{eff}, for the barely pressed powder is not negligible even at high frequencies.

4.5 Conclusions

In this study, we describe a relatively simple low-temperature synthesis route for the preparation of hydrophobic crystalline nanoparticles with size about 15 nm. The crystal structure of these $BaTiO_3$ particles was assigned to cubic $Pm3m$ by a conventional XRD measurement, whereas Raman spectra indicate that the tetragonal phase $BaTiO_3$ exists. SEM and HRTEM display as-prepared $BaTiO_3$ nanoparticles of spherical shape. Those directly calcined at 1050 °C have cubic and tetragonal shapes. The dielectric permittivity of as-prepared $BaTiO_3$ nanoparticles is about 70 at room temperature. Due to the simplicity and generalizability of the approach it is anticipated that this method can be extended to $SrTiO_3$, $PbTiO_3$,

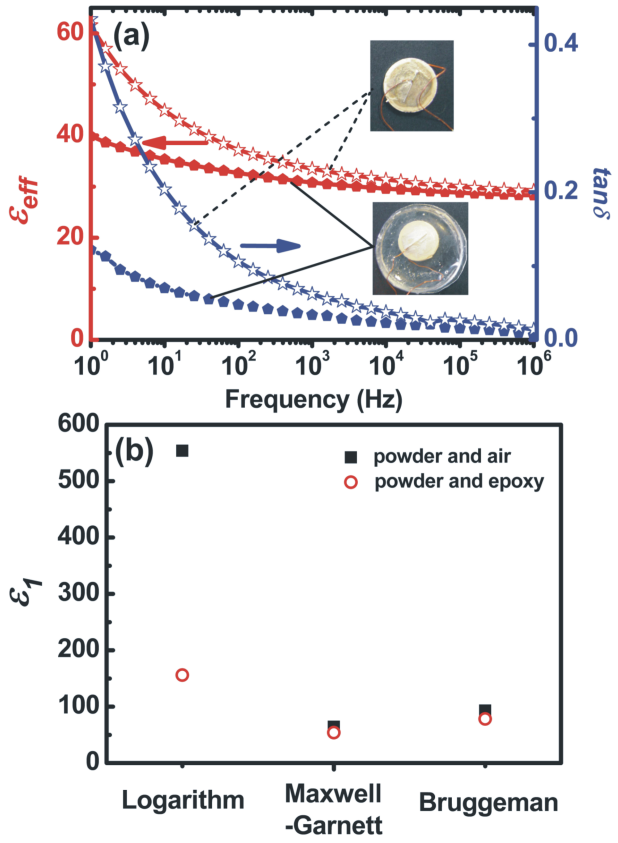

Figure 4.13: (a) Frequency dependences of the dielectric permittivity and loss tangent of air-pressed $BaTiO_3$ powder and epoxy-pressed $BaTiO_3$ powder at room temperature. (b) The dielectric permittivity of $BaTiO_3$ nanoparticles, ε_1, estimated using the Logarithm, Maxwell-Garnett and Bruggeman models.

$BaZrO_3$ and multi-component perovskite systems. Further work is progressing to incorporate these synthesized hydrophobic nanoparticles as nanodispersion into a photoconductive polymer matrix such as P3HT, CuPc with the aim of increasing the efficiency of organic solar cells by increasing the relative permittivity of polymer systems and hence the number of excitons converted into charge carriers.

4.6 Acknowledgments

I am thankful to Marlene Münch and Raphaela Schäper (Institute of Inorganic Chemistry, Faculty of Chemistry, University of Duisburg-Essen) for TGA/DSC and Raman measurements.

Chapter 5

Preparation of SiO_2-Encapsulated $BaTiO_3$ Nanoparticles with Tunable Shell Thickness by Reverse Microemulsion

5.1 Abstract

A reverse microemulsion (W/O) system was developed to coat ferroelectric nanoparticles with a dielectric silica shell. This approach was applied to hydrophobic $BaTiO_3$ nanoparticles and performed by hydrolysis and condensation of tetraethyl-orthosilicate (TEOS) using $BaTiO_3$ particles as seeds in a Triton X-100/n-hexanol/cyclohexane/water reverse microemulsion (W/O) system. The process was sufficiently controllable to allow us to target a shell thickness from 3 to 20 nm by choosing appropriate $BaTiO_3$ concentrations. The resulting coated $BaTiO_3$ particles were characterized by powder X-ray diffraction (XRD), high-resolution transmission electron microscopy (HRTEM), and Fourier transform infrared spectroscopy (FTIR) as well as charge titration via streaming potential.

5.2 Introduction

BaTiO $_3$ -based nanocomposites with other functional material components, such as polymers, metals, and/or ferromagnetic phases are currently being studied for ultrahigh dielectric constant materials, power storage, magnetoelectric, or photovoltaic applications [114, 181–185]. Even through numerous reports can be found on the synthesis of $BaTiO_3$ nanoparticles [53, 139, 186], there are only a few dealing with particle coatings and surface modification [109, 187–191]. In the present study, we describe the encapsulation of a ferroelectric

nanometer-scale $BaTiO_3$ core in a thin surrounding shell made of a non-ferroelectric amorphous silicon oxide, denoted as BTO@SiO_2. The study of the incorporation of $BaTiO_3$ particles into a silica matrix to obtain hybrid core@shell structures is very important, because of significant changes and/or improvements in the ferroelectric, dielectric, electric, and optical properties of the resulting products due to the coating by a silica layer [192, 193]. For example, the properties of nanosized-ferroelectrics extremely depend on boundary conditions [194] and temperature of the ferroelectric. Phase transformation in an array of electrically coupled small particles, for example, could be very different from that in isolated small particles [195]. On the other hand, this nanostructured core@shell system is efficient to decrease the dielectric losses of the final $BaTiO_3$-based ceramics [190, 196, 197] and also to achieve multifunctional nanoparticles in the coating [182, 198]. Huber et al. [190] observed a relationship between the dielectric loss and the thickness of a silica shell over $Ba_{1-x}Sr_xTiO_3$. As the silica shell thickness increases, the dielectric loss decreases and becomes more stable as a func tion of temperature when compared to the unmodified material.

In the case of coating oxide particles with silica, various synthetic routes among which the two most common routes are the Stöber method [76, 199, 200] and the microemulsion process [30, 201–204] have been investigated. So far, the Stöber method has already been applied to various inorganic compounds [205–211]. Although the method is relatively simple, it is difficult to achieve thickness control below 20 nm [212]. Multiple preparation steps are needed and nanoparticles with nonpolar ligands cannot be coated easily. The microemulsion method is an alternative to the Stöber method. Reverse microemulsion (water-in-oil microemulsion) has recently also been used for the production of magnetic oxide@silica nanoparticles with core@shell structure [213, 214]. Advantages of this method are that the resulting silica nanoparticles have "smooth" surfaces and display good monodispersity, and that nanoparticles with nonpolar ligands can be directly coated [214]. Using soft chemical routes, ferroelectric $BaTiO_3$ powders are nowadays produced on a large scale and at low cost. Our starting $BaTiO_3$ nanopowders with oleic acid ligands (BTO@OA) were directly prepared by the "Organosol" route, possessing excellent dispersibility in organic solvents [215]. Compared with the Stöber method, BTO@OA nanoparticles with good dispersion stability at high particle concentration in the microemulsion can lead to high coating levels of nanoparticles in the final nanocomposites, furthermore, the nanoparticles were encapsulated with SiO_2 by means of a microemulsion technique for phase transfer into aqueous dispersion or other polar solvents.

In the sections that follow, we present a detailed study of BTO@SiO_2 hybrid nanoparticles synthesized in a reverse microemulsion with a composition of Triton X-100/1-hexanol/cyclohexane/H_2O. The BTO@OA nanoparticles were phase transferred into polar solvents by means

of silica coating and the synthesized BTO@SiO_2 nanoparticles were fully characterized by a variety of techniques including transmission electron microscopy (TEM), high resolution TEM (HR-TEM), X-ray diffraction (XRD), and Fourier transform infrared (FT-IR) as well as charge titration via streaming potential. To the best of our knowledge, this is the first report of a direct silica coating of $BaTiO_3$ nanoparticles with hydrophobic surface ligands via the reverse microemulsion method. Through thickness control of the silica shell the separation between neighboring particles can be tuned so that the collective behavior of the particles within a nanostructure can be tailored. Besides, we believe that our methodology will ensure more functional groups over the core@shell nanoparticles to adopt them into the desired organic applications.

5.3 Experimental section

5.3.1 Materials

All reagents used in this study are commercially available. Oleic acid (OA, 90%), 1-hexanol anhydrous (99%), ammonia solution (NH_4OH, 28-30 wt% in water), Triton X-100, hexane (95%), cyclohexane (99.5%), tetraethoxysilane (TEOS, 99.999%) were purchased from Sigma-Aldrich Inc. Water purified with a Milli-Q system from Millipore was used for all experiments.

5.3.2 Synthesis of BTO@SiO_2 nanoparticles

For a typical reverse microemulsion synthesis, 2.5 mL of a cyclohexane dispersion of BTO@OA nanoparticles was rapidly added into a mixture of 8.85 g of Triton X-100, 8 mL of anhydrous 1-hexanol, and 35 mL of cyclohexane under a strong vortex for about 1 h. Depending on the desired SiO_2 shell thickness, the concentration of the $BaTiO_3$ dispersion was varied from 1 to 10 mg mL^{-1}. Next, 2.5 mL of ammonia solution (28-30% ammonia solution:water = 1:4) was added in the above solution and shaken for another 1 h. Finally, 125 μL of TEOS as the precursor of silica nanoparticles was added to the microemulsion, and the silica growth was completed after 24 h of stirring. The nanoparticles were isolated from the microemulsion using acetone and centrifuged, and the resultant precipitate of BTO@SiO_2 composite particles was washed with 1-propanol and ethanol to remove surfactant and oil, and collected by centrifugation.

5.3.3 Characterizations

The synthesis of core-shell BTO@OA particles was characterized by various analytical techniques. The morphologies of the nanoparticles and the shell thicknesses of the coated nanoparticles were characterized using a HR-TEM (FEI Tecnai F20, 200 kV) with scanning-mode TEM (STEM) imaging and energy-dispersive X-ray (EDS) mapping capabilities. The phase structure and composition analysis of the prepared BTO@SiO_2 composites were characterized by XRD (Siemens D5000, λ = 1.5418 Å (Cu$K\alpha$), kV = 40, mA = 40) and FT-IR spectroscopy analysis (Bruker Vertex 70) in the range of 4000-400 cm^{-1}. Charge titration via streaming potential was measured by using a Stabisizer® instrument (Particle Metrix GmbH, Stabisizer PMX 200C). 10 μL of the sample ($BaTiO_3$ or BTO@SiO_2) was dispersed into 10 ml of 10 mM KOH solution. The mixture was titrated with 5 mM HCl down to pH 2.

5.4 Results and discussion

5.4.1 FT-IR Spectroscopic Analysis

One of the most common methods of analyzing SiO_2 is based on the absorption of infrared light. When the frequency of a specific vibration is equal to the frequency of the IR radiation directed at the molecule, the molecule absorbs the radiation. The major types of molecular vibrations are stretching and bending. The various types of vibrations for SiO_2 are illustrated in Figure 5.1. In this study we will focus on the most frequently considered portion of the middle IR region, between 400 and 4000 cm^{-1}. Figure 5.2 shows the FT-IR absorption spectra of BTO@OA, BTO@SiO_2 (4 ± 1 nm) and BTO@SiO_2 (20 ± 0.7 nm) nanoparticles, respectively, where some vibrational modes of Si-O and hydrogen incorporated molecules are pointed. The peak at 594 cm^{-1} is the characteristic absorption of Ti-O bond and the peaks at 1465 and 1552 cm^{-1} can be attributed to the COOH group of oleic acid adsorbed on the $BaTiO_3$ surface. It is also found that the BTO@SiO_2 (4 ± 1 nm) and BTO@SiO_2 (20 ± 0.7 nm) nanoparticles exhibit a new set of peaks that belong to Si-O-Si and Si-OH at 468, 960 and 1091 cm^{-1}, respectively, which clearly indicates the presence of SiO_2. Additionally, such siloxane bonds increase in intensity as the thickness of the silica shell increases from 4 ± 1 to 20 ± 0.7 nm, while the vibration bands of Ti-O bond weakened with increasing silica coating amount finally disappearing. Thus, we can infer that SiO_2 shells originated from the hydrolysis and condensation of TEOS were successfully coated onto the $BaTiO_3$ surface.

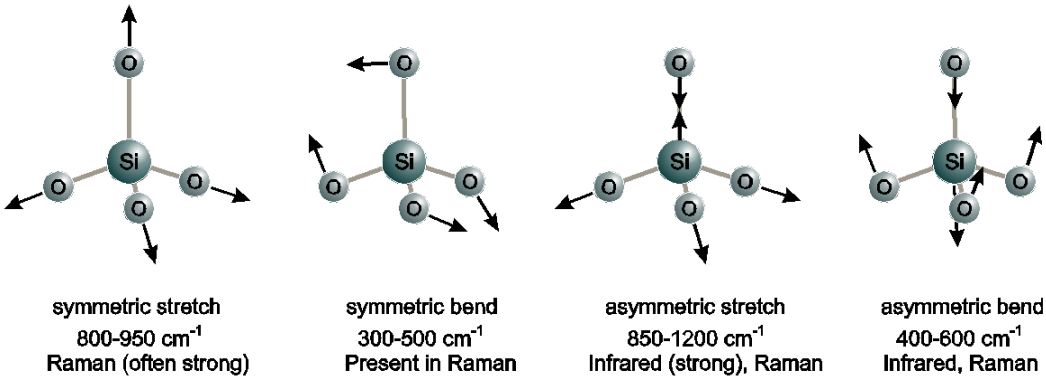

Figure 5.1: Major vibrational modes for a nonlinear group [29].

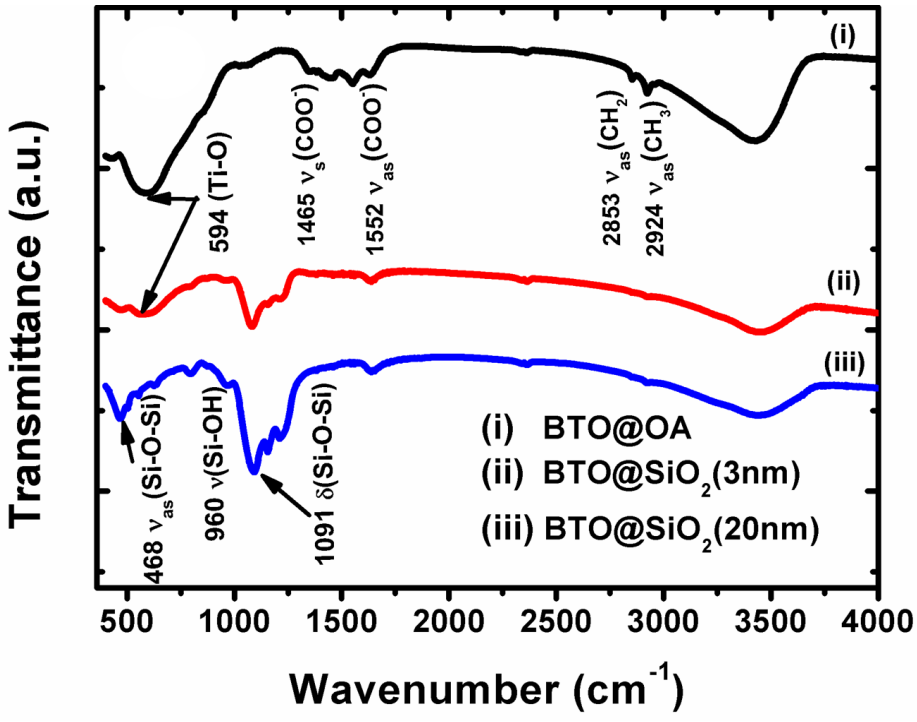

Figure 5.2: FT-IR spectra of core-shell $BaTiO_3$ particles, as a shell: i) oleic acid, ii) SiO_2 (4±1 nm), and iii) SiO_2 (20 ± 0.7 nm).

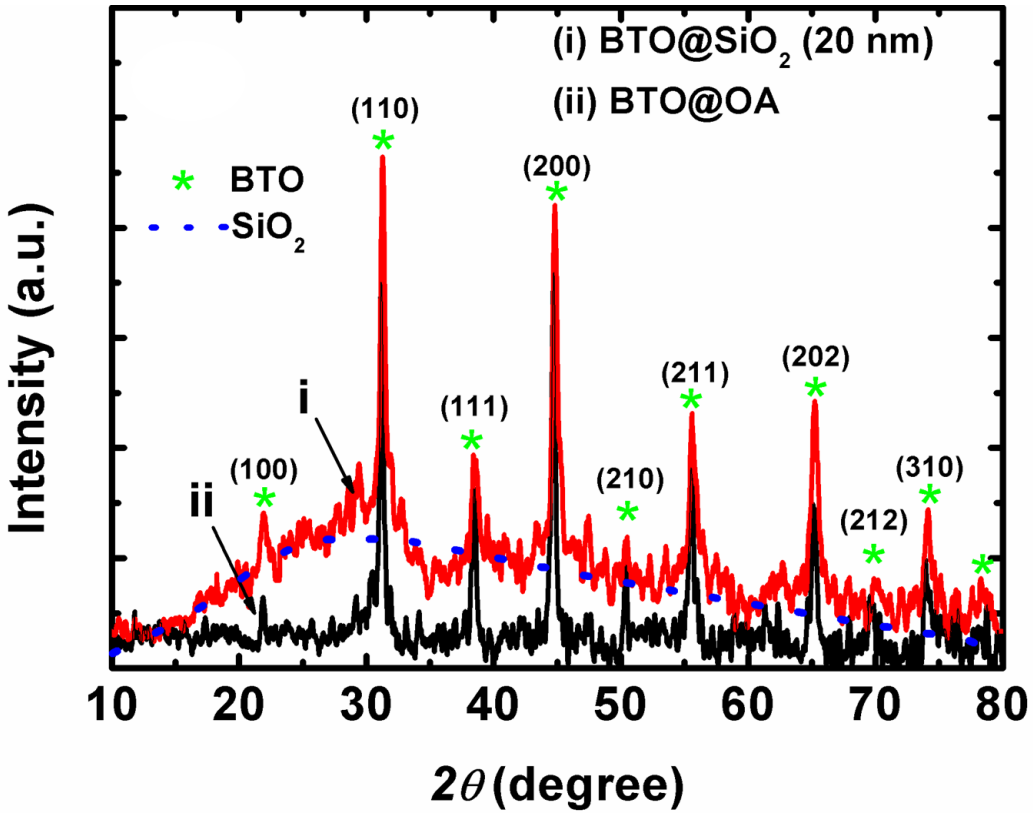

Figure 5.3: X-ray diffraction pattern of samples: i) BTO@SiO_2 particles and (ii) BTO@OA particles. $BaTiO_3$ is marked with asterisks.

5.4.2 XRD Analysis

The XRD spectra of BTO@OA and BTO@SiO_2 (20 ± 0.7 nm) nanoparticles are shown in Figure 5.3. From Figure 5.3 (ii), a series of characteristic peaks is observed and indexed in accordance with the cubic perovskite structure of $BaTiO_3$ (JPCDS No. 31-174). After modifying with a SiO_2 shell layer, the characteristic peaks of samples are still in accordance with the cubic perovskite phase of $BaTiO_3$ (see Figure 5.3 (i)), indicating that the SiO_2 does not influence the crystalline structure of the core. Additionally, there is a broadened peak located in the range of ca. 22°, which is the characteristic of amorphous SiO_2. A similar report on Fe_2O_3@SiO_2 core-shell nanoparticles also showed a diffuse peak at about 20° of SiO_2 shell in the XRD pattern [208].

5.4.3 Surface properties of nanoparticles (Surface charge & Solubility)

The surface coating of nanoparticles is crucial to determining their physicochemical surface properties, such as hydrophilicity/hydrophobicity and zeta potential as well as dispersibility

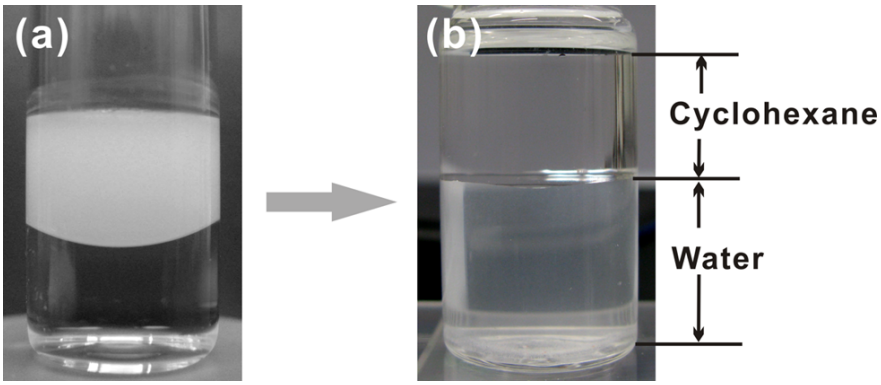

Figure 5.4: Dispersion of powders in a two-phase solvent, the bottom layer of which is water and the upper layer is cyclohexane: (a) BTO@OA and (b) BTO@SiO_2.

in solution. Due to the hydrophobic surface ligands, oleic aicd-stabilized $BaTiO_3$ particles showed a much higher solubility in apolar solvents than in polar solvents (Figure 5.4 (a)). The success of silica coating was also indicated by the change in the solubility of the silica-coated $BaTiO_3$ particles, which became highly soluble in polar solvents such as water instead of apolar solvents (Figure 5.4 (b)).

The surface charge of the nanoparticles is an essential factor in colloidal systems. It is related to the streaming potential of the suspended particles inside a narrow capillary [216]. The streaming potential reveals changes in the surface charge, if the surface is functionalized with different functional groups. Therefore, after successful SiO_2 shell synthesis, streaming potential measurements of the resulting particles inside a Teflon capillary were performed. Figure 5.5 shows the influence of pH on the streaming potential measured on $BaTiO_3$ and BTO@SiO_2 particles. The streaming potential of $BaTiO_3$ and BTO@SiO_2 with respect to diffe rent pH and the isoelectric points (IEP), defined as the condition when the zeta-potential value is zero, are consistent with the zeta potential measurement reported in literature. The streaming potentials were found to be similar for both samples BTO@SiO_2(20 nm) and BTO@SiO_2(3 nm) as they have their IEP below pH 2. It was already noted that the electrokinetic behavior of the SiO_2 surface is dominated by surface Si-OH species, thus explaining the relatively low IEP value [217–219]. Because the IEP of SiO_2 is below 2.0, its surfaces are highly negatively charged even at a pH of 3. $BaTiO_3$ shows variable electrophoretic behaviour, depending on the BaO : TiO_2 balance at the particle surface. Lewis listed the IEP of $BaTiO_3$ as being between pH 5 and 6, while Vamvakaki et al. [220] reported a value of 3, although these authors note that a wide range of values have been reported, a result of either residual barium carbonate on the surface or TiO_2-rich surfaces. Our $BaTiO_3$ nanoparticles showed a distinctly different behavior compared to SiO_2 and have an IEP at around pH 5. This result suggests that, in acidic solutions, our $BaTiO_3$ powder behaves more comparably to colloidal TiO_2, because of the

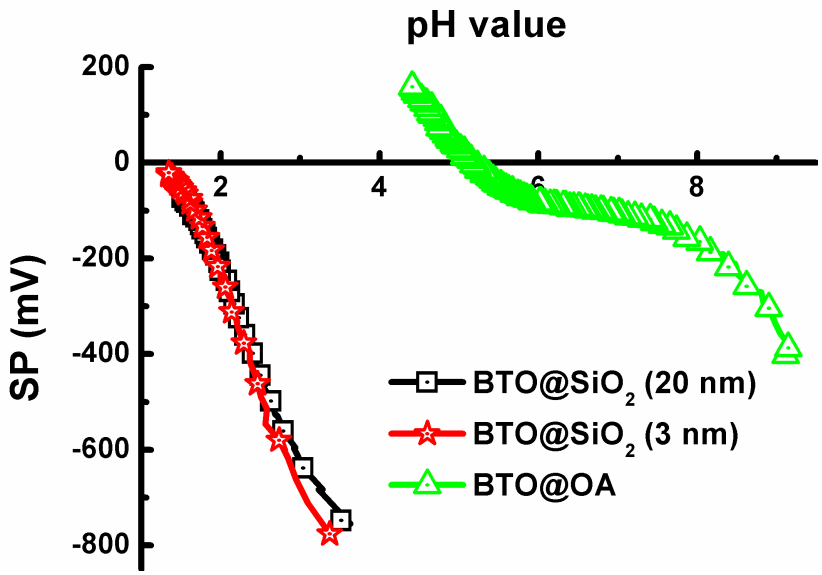

Figure 5.5: Streaming potential (SP) curves of $BaTiO_3$ and BTO@SiO_2 particles.

surface dissolution of Ba^{2+} ions.

5.4.4 TEM and EDS Analysis

TEM was used to observe core-shell BTO@SiO_2 nanoparticles. HR-TEM images demonstrate that the nanoparticles have a core-shell structure with light contrast silica shells and dark contrast cores of $BaTiO_3$, implying that the hydrophobic $BaTiO_3$ nanoparticles were successfully coated by a silica shell. As shown in Figure 5.6, 5.7, 5.8, we found that the silica layer thickness dramatically decreased from 20 ± 0.7 to 4 ± 1 nm upon an increase in concentration of $BaTiO_3$ from 1 to 10 mg mL^{-1}: In the first case, the reverse microemulsion contains a cyclohexane dispersion of 1 mg mL^{-1} $BaTiO_3$ nanoparticles, after addition of 125 μL TEOS, silica shells are finally formed with a homogeneous thickness of at least 20 nm. Most of the TEOS is polymerized on the $BaTiO_3$ particle surface, but small $BaTiO_3$-free silica particles are formed as well, as shown in Figure 5.7. Furthermore, TEM and HRTEM images (Figure 5.6 (a, b)) clearly show the crystallinity of the $BaTiO_3$ core and the amorphous nature of the silica shell and their interface. From the EDS elemental mapping images, there is also strong evidence of the BTO@SiO_2 core-shell structure showing that Ba (Figure 5.6 (c)) is localized in a core area in HAADF-STEM, while Si (Figure 5.6 (d)) is localized in a shell configuration. By overlapping the two maps (Figure 5.6 (e)), it is observed that $BaTiO_3$ is located inside the silica shell. In addition, we have also carried out EDS line scans across the region of the individual core-shell particle for the respective elements (Figure 5.6 (g)). While nanoparticles could reproducibly be coated with thick silica shells, synthesis of thinner shells was not

straightforward. We studied the effect of using a highly concentrated $BaTiO_3$ cyclohexane dispersion (10 mg mL^{-1}) and the same amount of TEOS (125 μL). We expected this would lead to the formation of thinner shells and no small, free silica particles, as the deposition of silica would be divided over a larger number of particles. We found that the silica layer was not perfectly homogeneous, but practically the entire surface of all the $BaTiO_3$ particles appeared to be coated and no second nucleation was formed, as shown in Figure 5.8 (a, b). At the same time, we can see that a thin shell (3-5 nm) is present on the surface of the $BaTiO_3$ (Figure 5.8 (c)) and its crystalline phase with lattice fringes can be seen more clearly (Figure 5.8 (d)). Such a thin silica layer is a notable result, because the average thickness of silica layers previously prepared by reverse microemulsion has been reported as 10-70 nm [201, 221].

5.4.5 Mechanism of core-shell particle formation

Understanding the mechanism through which the process is taking place allowed us to precisely control the synthesis and obtain very good reproducibility. Previously published work on nanocomposites through reverse microemulsion methods first by Darbandi et al. [30] and more recently by Kool et al. [201] have proposed a ligand exchange mechanism on hydrophobic quantum dots in silica spheres. According to our results obtained by XRD, Fourier transform infrared (FTIR) spectroscopy, and HR-TEM of the synthesized BTO@SiO_2 nanoparticles, we here suggest that the formation mechanism of silica shell on hydrophobic $BaTiO_3$ can be described as follows: Step I: In the initial stage, the formation of the inverse microemulsion and stabilization of water droplets by n-hexanol and Triton X-100 takes place. The BTO@OA nanoparticles are easily dispersible in the cyclohexane oil phase. Step II: A ligand exchange occurs at the surface of the $BaTiO_3$ where hydrophobic ligands are replaced by TEOS that is able to hydrolyze at the water-oil interface. Step III: On addition of the ammonia catalyst that is constrained in the water droplets, the continuous association of the hydrolyzed TEOS molecules in excess from the oil phase creates the condensation and growth of silica shells on the surface of the water phase-transferred $BaTiO_3$ (schematically depicted in Figure 5.9). According to the mechanism above, the ligand exchange Step II is believed to be the most crucial one to ensure homogeneous shell growth. This indicates that the inhomogeneity in thin silica shells is likely connected with the lack of complete coverage of TEOS on the $BaTiO_3$ surfaces, because when the concentration of $BaTiO_3$ is increased and the molar ratio of TEOS/$BaTiO_3$ is reduced from 56:1 to 5.6:1. In conclusion, more investigation is required to fully understand the formation mechanism of the thin coating layers, but deposition of very thin layers has been proven to be well feasible by the microemulsion technique. Furthermore, the preparation of highly stable ultrathin silica layers and the investigation of their stability are an important challenge in future research, because ultrathin silica layers are likely to be

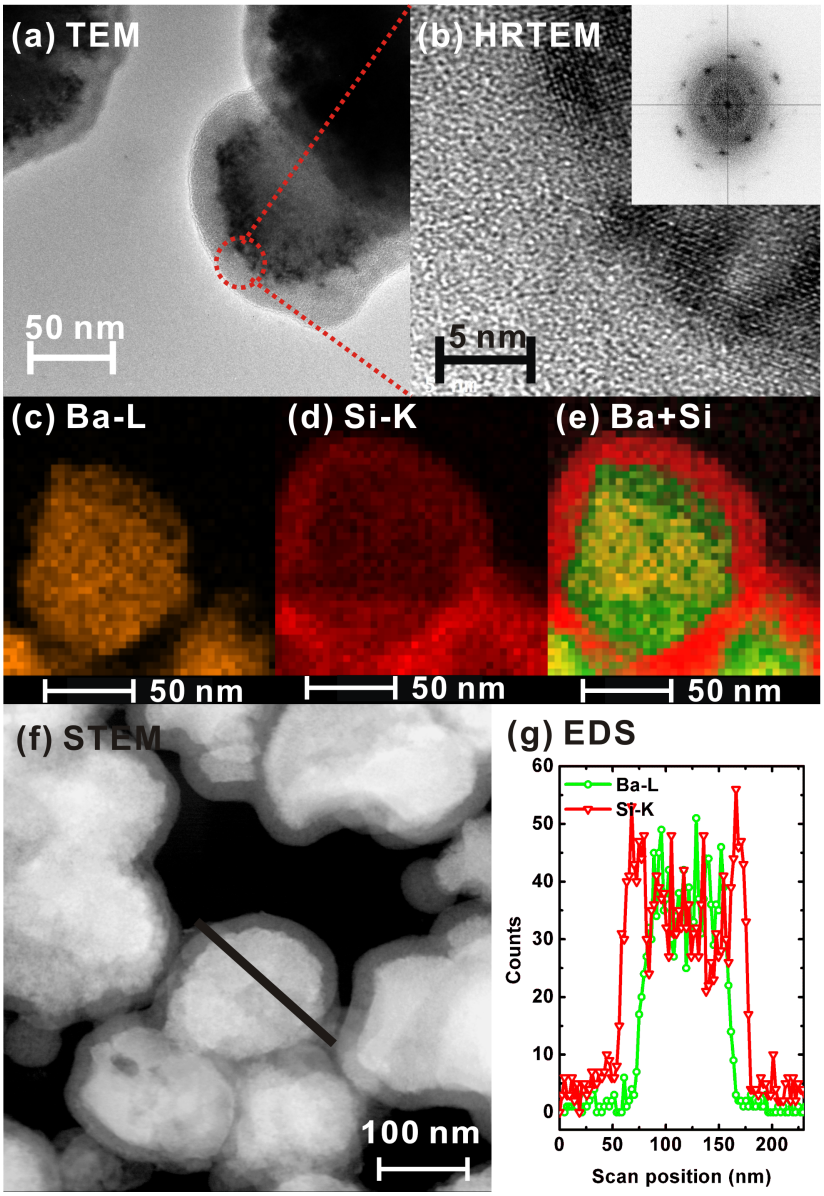

Figure 5.6: Imaging core-shell nanostructures in BTO@SiO_2 (20 ± 0.7 nm), added 125 μL of TEOS solution into a reverse microemulsion containing a concentration of 1 mg mL^{-1} $BaTiO_3$ dispersion: a) TEM image and b) HRTEM image of the interface between the crystalline core and amorphous shell. The inset of (b) shows the FFT pattern. c-e,g) Elemental mapping images of a BTO@SiO_2 core-shell nanostructure and EDS line scan and f) STEM image of several BTO@SiO_2 core-shell nanoparticles.

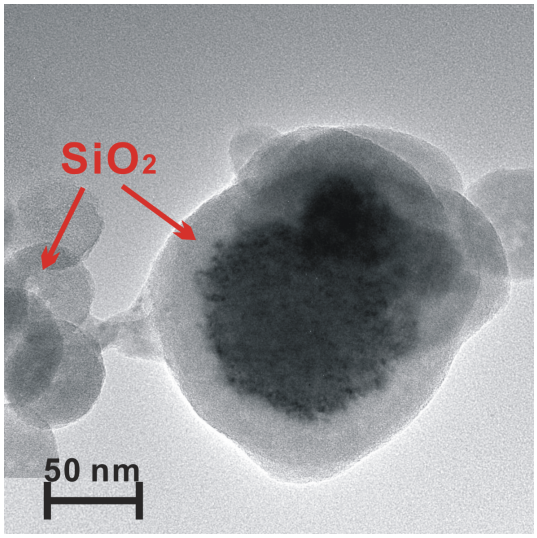

Figure 5.7: TEM image of $BaTiO_3$ core@SiO_2 shell particles and free SiO_2 particles.

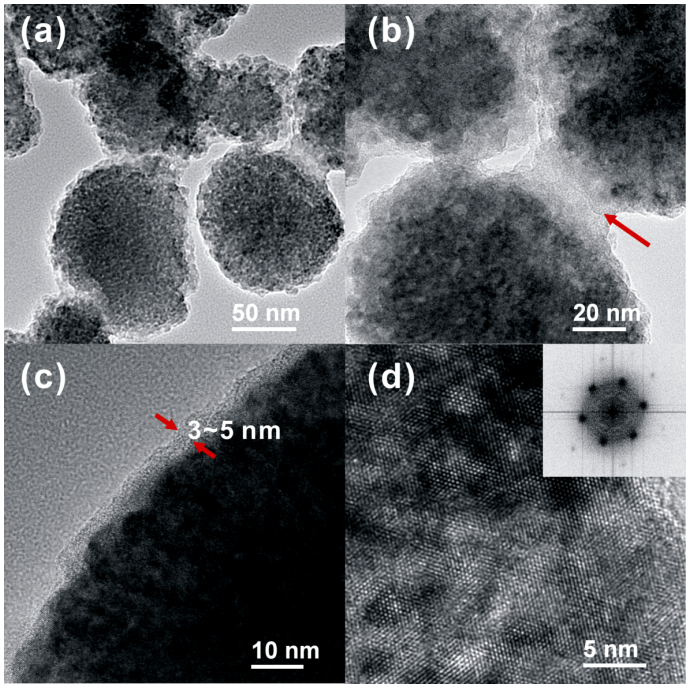

Figure 5.8: a-c) TEM images of core-shell nanostructures in BTO@SiO_2 (4 ± 1 nm), added 125 μL of TEOS solution into a reverse microemulsion containing a high concentration of 10 mg mL^{-1} $BaTiO_3$ dispersion. In (b) the arrow indicates neck formation. c) An interface where a thin amorphous SiO_2 layer (3-5 nm) was inhomogeneously formed and d) HRTEM image of crystalline $BaTiO_3$ core. The inset of (d) shows the FFT pattern (zone axis [111]).

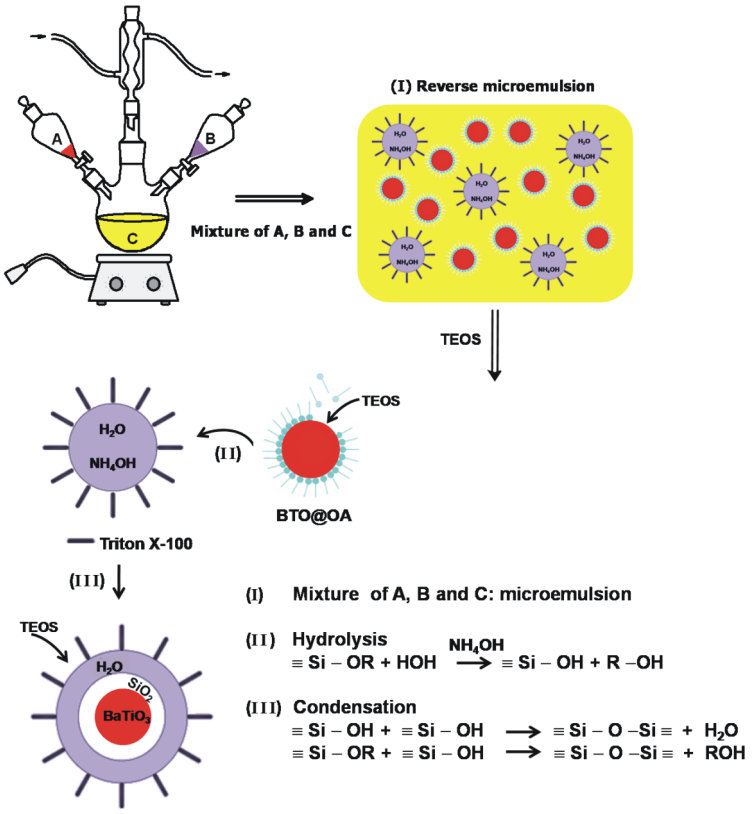

Figure 5.9: Schematic of the $BaTiO_3$ core@silica shell nanoparticle formation after Darbandi et al. [30]. Reaction mechanism in reverse microemulsion system. Step I: mixing of reactants A, B, and C. Step II: hydrolysis reaction (nucleation stage (a)). Step III: the condensation reaction (growth stage (b)) of primary SiO_2: A) BTO@OA in cyclohexane; B) ammonia water; C) mixture of cyclohexane, surfactant Triton X-100 and co-surfactant 1-hexanol.

unstable and re-dissolve in the solvent with time. All of our powders were finally dry powders not so eligible to re-dissolution.

5.5 Conclusions

In this study we demonstrate the possibility of formation of nanoparticles of $BaTiO_3$ covered with a silica shell using a Triton X-100/n-hexanol/cyclohexane/water reverse microemulsion (W/O), which employs nucleation in water-in-oil (W/O) microemulsion and shell coating through hydrolysis and condensation of silane in W/O microemulsion. That $BaTiO_3$ nanoparticles with partially hydrolyzed TEOS transfer from the oil phase to the water phase of the microemulsion is essential for the formation of the silica shell on the $BaTiO_3$ core. Further hydrolyzation of TEOS contributes to the increase in the shell thickness and the formation of a smooth surface. It is crucial to control the concentrations of both TEOS and $BaTiO_3$ to tune

the thickness of the silica shell and suppress the development of secondary silica nuclei which is always a side effect in coating processes.

5.6 Acknowledgements

I would like to thank V. V. Shvartsman of the Institute for Materials Science, University of Duisburg-Essen for helpful comments on the manuscript, Inge Danielzik of the Institute of Technical Chemistry, University of Duisburg-Essen for Zeta potential measurements and the Institute of Inorganic Chemistry, Faculty of Chemistry, University of Duisburg-Essen for use of the IR measurement setup.

Chapter 6

Core@shell Ag@$BaTiO_3$ Plasmonic Absorber Systems Synthesized via the "Organosol" Route

6.1 Abstract

In this work, core@shell structure Ag@$BaTiO_3$ composite nanopowders with tunable optical properties were synthesized in two steps that include the formation of the Ag core in first and second step is the coating with $BaTiO_3$. A stable Ag "organosol" was prepared by the thermal reduction of silver oleate in oleic acid and followed by its incorporation with $BaTiO_3$ "organosol" precursor at different Ag/Ba molar ratios a controllable nanolayer of $BaTiO_3$ on the surface of Ag was formed. This combination of two processes gave us a great inspiration to fabricate metal-ceramic composites. Due to the Ag content obtained nanocomposites possess important valuable properties. First, one is that these Ag@$BaTiO_3$ composites have higher dielectric permittivities compared to the pure $BaTiO_3$, which can be attributed to the interfacial polarization phenomenon that takes place at the Ag-$BaTiO_3$ interfaces and the percolation effect. Besides, another of these important properties deals with the light absorption by the composite. In the case of Ag nanoparticles coated by an ultrathin dielectric $BaTiO_3$ shell with a thickness less than 5 nm, we find that it is an ideal plasmonic blackbody that absorbs all light that falls onto it. Because of that, such core@shell structure nanoparticles can be used to trap light in organic solar cells to increase optical absorption, which will open up opportunities for the development of the future thermo-photovoltaic energy conversion devices, light harvesting for solar cells and storage technologies.

6.2 Introduction

Photovoltaics is emerging as an important technology for the future energy production. To fully realize this potential it is necessary to generate a high conversion efficiency for the solar cells. In recent years, surface plasmons are taken as one of the best solutions to achieve this object [222–225]. Surface plasmon resonance (SPR) can be interpreted as the collection of electrons at the metallic surface, induced by the electromagnetic wave, and these collected electrons vibrate together in a particular way. Due to their evanescent nature, surface plasmons are able to give rise to peculiar interaction with light, leading to effective light localization and concentration. In 1908 Mie [226] proposed a solution of Maxwell's equations for spherical particles interacting with plane electromagnetic waves, which explains the origin of SPR in the extinction spectra and colouration of metal colloids.

During the last century optical properties of nanoparticles have extensively been studied and metal-dielectric nanocomposites have found many novel properties unattainable in single nanostructures and various applications in diff erent fields of science and technology. Particularly, core@shell metal-dielectric composite nanostructures are extremely important in plasmonics because they realize highly tunable and designable optical properties. Since the optical properties of metal nanoparticles are governed by SPR, they are strongly dependent on the nanoparticles' size, shape, concentration and spatial distribution as well as on the properties of the surrounding medium which the nanoparticles are embedded in [92, 227, 228]. Control over these parameters enables such metal-dielectric nanocomposites to become promising media for the development of novel non-linear materials, nanodevices and optical elements.

There are two main classes of core@shell metal-dielectric composite nanostructures: dielectric core@metal shell nanostructures and metal core@dielectric shell nanostructures. Dielectric core@metal shell nanoparticles (called nanoshells in some papers) are obtained by coating a metal layer onto dielectric nanoparticles. The optical resonances of such composite nanostructures can be tuned within the visible to near infrared (NIR) spectral range by controlling the ratio of the core diameter and the shell thickness [229]. For such structures plasmon hybridization theory was developed [230–232]. It allows to design materials to match the required wavelength for a particular application in the visible or near infrared regions. But, in this case, existence of optical losses of metals prevents them from successful application in photonics so far, moreover, the pure formed metal nanoparticles are very activated and unstable due to easy agglomeration, oxidation in air, and dissolution in acid, which complicates their use in the development of photovoltaic devices, sensors and other optical instruments. In contrast to dielectric core@metal shell nanoparticles, the opposite core@shell nanostructure with metal core and dielectric shell can overcome these problems. The dielectric layer onto metal nanoparticles can most typically be formed from at least one of SiO_2, TiO_2, and

Al_2O_3, with refractive indices of 1.5, 2.5 and 1.63, respectively [233]. Coating the metal nanoparticles with a dielectric layer will prevent direct contact between the surfaces of neighboring metal nanoparticles and improve their chemical stabilities. $BaTiO_3$ was chosen as the alternative dielectric shell, because it has good chemical stability, high dielectric constant and refractive index values (2.5 at wavelength 500 nm). However, when these metal core-oxide shell nanoparticles are prepared, there are problems in that the oxide coated onto the surface of the metal core is amorphous in nature, and thus has reduced chemical and mechanical properties compared to crystalline oxides. For example, Seung Ho Choi et al. prepared core@shell structure Ag@$BaTiO_3$ composite powders directly by flame spray pyrolysis, but the formed $BaTiO_3$ shell is amorphous [234]. On the other hand, although monodisperse metal nanoparticles have been produced by many reported methods, metal/oxide composite nanopowders had still problem in uniform dispersion of metal in the oxide because of the aggregation behavior of the metal nanoparticles.

In the present work, we describe the preparation of the plasmonic nanocomposites with a Ag core and a dielectric crystalline $BaTiO_3$ shell using combination of thermal reduction and organosol methods. Thermal reduction has great advantages for large-scale synthesis at the industrial level and offers the advantage of producing essentially clean Ag nanoparticles. Successful nanoscale coatings require freedom from agglomeration and surface control. Oleate was used to modify the surface of Ag nanoparticels to allow attachment of $BaTiO_3$ organosol precursor to their surface. After that, crystalline $BaTiO_3$ shell-covered Ag was synthesized by using the previous organosol technique [215]. Afterward characterization of the resultant structure has been performed by means of X-ray diraction (XRD), transmission electron microscopy (TEM), Scanning Electron Microscopy (SEM), Fourier transform infrared (FTIR) spectroscopy, ultraviolet-visible (UV-Vis) spectroscopy, and impedance analysis. We found that the ultrathin dielectric $BaTiO_3$ shell (less than 5 nm) in the composite could result in almost complete absorption of light in a broad spectrum. This excellent property has motivated us to study this core@shell structure Ag@$BaTiO_3$composite with the aim to design a perfect absorber (plasmonic blackbody), which can be profitably used for the development of organic photovoltaic devices and our results represent a promising first step for subsequent investigations on their applicability in organic solar cells [235–238]. In the following, we describe the whole process of making core@shell Ag@$BaTiO_3$ nanotructures and provide detailed characterization of these materials.

6.3 Experimental Details

6.3.1 Materials

The synthesis and decomposition experiments were performed using the following chemicals: Ag acetate (CH_3COOAg, Merck KGaA, Darmstadt, Germany), barium acetate ($Ba(CH_3COO)_2$, 99%, Sigma-Aldrich, Steinheim, Germany), titanium isopropoxides ($Ti(OCH(CH)_2)_4$, 97%, Sigma-Aldrich, Steinheim, Germany), and oleic acid (OA, 65-88%, Sigma-Aldrich, Steinheim, Germany) were purchased from Sigma-Aldrich and used without further purification. All chemicals were used as received.

6.3.2 Characterization Methods and Instruments

X-ray diffraction (XRD) analysis of the synthesized powder was studied at room temperature using a diffractometer (Siemens D5000, Germany) in the range of Bragg angle ($20^o \leq 2\theta \leq 80^o$) on being irradiated by using Cu$K\alpha$ (1.5405 $\mathring{A}$) with an angular step of 0.01 at 1 s per step. The surface morphology or microstructure (i.e., grain size, grain-distribution and core/shell structure) of the nanoparticles were recorded by scanning electron microscopy (SEM) (Quanta 400 FEG) and transmission electron microscopy (TEM) microscopy (Tecnai F20). The Surface plasmon resonance (SPR) of the sample was determined using a UV 2500 Schimadzu UV-visible spectrophotometer (Shimadzu, Osaka, Japan). All optical measurements were performed at room temperature using quantitative ethanol or 1,2-dichlorobenzene solutions. Moreover, the fourier transform infrared (FT-IR) spectra were recorded over the range of 400-4000 cm^{-1} utilizing a Bruker Vertex 70 FT-IR spectrophotometer. After the reactions, the sample was centrifuged by using a centrifuge machine (Heraeus Labofuge 400e). For electrical measurements, the powder was uniaxially cold pressed at 5 tons into pellets (diameter of 0.5 cm) with a minor addition of P(VDF-TrFE), 1.5 wt % as a binder. The disk surfaces were ground gently and electroded was with Pt/Pd using a sputter coater (Cressington 208HR). The ac conductivity and permittivity were measured from 300 to 420 K using a Solartron 1260 Impedance Analyser with a Solartron 1296 dielectric interface in the frequency range 0.1 Hz to 1 MHz and the applied voltage was 0.1 Vrms. The density of the tablets was measured by He-pycnometry (Porotec GmbH).

6.3.3 Preparation of Ag@$BaTiO_3$ nanoparticles

The synthesis of the Ag@$BaTiO_3$ nanoparticles was carried out in two steps: the synthesis of a Ag organosol, followed by its incorporation with $BaTiO_3$ "organosol" precursor to prepare Ag@$BaTiO_3$ nanoparticles.

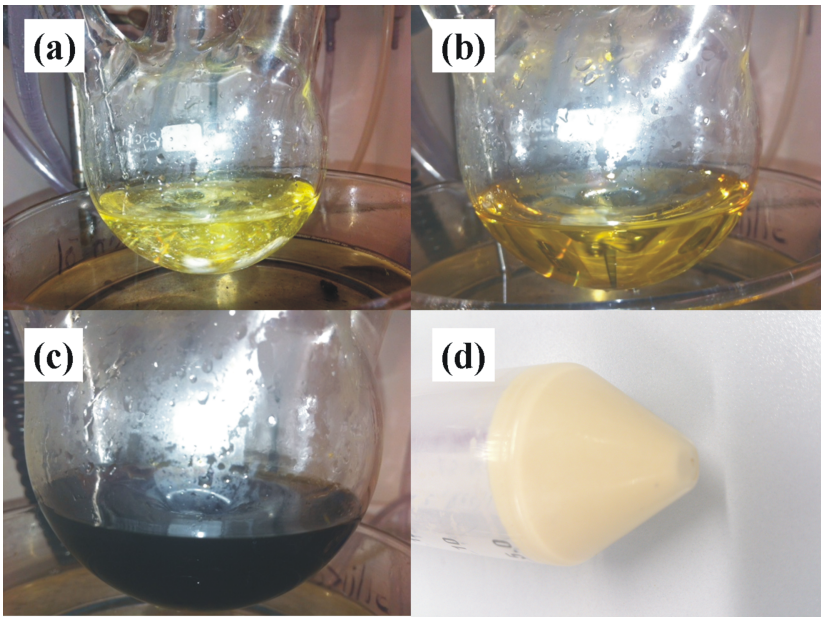

Figure 6.1: Photographs of Ag acetate in oleic acid after each step of a chemical procedure: (a), (b), (c), and (d) (see text). The Ag oleate precursor was prepared by the reaction of Ag acetate with oleic acid.

6.3.3.1 Preparation of Ag Organosols

Oleate capped Ag organosols were produced by an inexpensive, environmentally friendly process through the thermal reduction of a Ag oleate complex in oleic acid.

First, **preparation of the Ag oleate precursors**

In a typical procedure, as shown in Figure 6.1:

(a) Ag acetate (2 g) and oleic acid (60 ml) were added into a 250 ml three-neck round bottom flask.

(b) The reaction flask under nitrogen protection was firstly heated to 100 °C in an oil bath with stirring to make the Ag acetate dissolve.

(c) Then the flask was heated up to 150 °C, the Ag acetate/oleic acid solution became dark brown. By maintaining at this temperature for 10 min, we removed the flask from the heating device and let it cool to room temperature.

(d) The obtained products were centrifuged at 3000 r.p.m for 10 min after addition of methanol/toluene. The white-turbid precipitates were washed by centrifugation redispersion cycles with methanol/toluene mixture three times, and subsequently dried at room temperature.

In the next step, **preparation of Ag organosols**

The Ag nanoparticles were synthesized by the thermal reduction of the Ag oleate precursor

in oleic acid. The dried Ag oleate precipitates were dissolved in oleic acid to perform a thermal reduction reaction. The Ag oleate precursor solution was placed in an oil bath heated at ca. 180 °C. Heating the solution at that temperature for 4 hours caused gradual decomposition to produce a brown dispersion with metallic luster. After that, we removed the solution from the oil bath and let it cool to room temperature. The resultant dispersion was centrifuged for 15 min at 3000 rpm to separate the black Ag nanopowder. The separated Ag nanoparticles were washed by centrifugation redispersion cycles with alcohol three times and dried under vacuum. The obtained black Ag powder could be redispersed in various organic non-aqueous solvents for the purpose of further characterization.

The obtained black Ag nanoparticles were almost immediately redispersed in toluene or 1,2-dichlorobenzene to form a clear yellow organosol. This hydrophobic colloid is stable and the nanoparticles retain their integrity even after the solvent is evaporated and the dried deposit can be resuspended in a variety of other solvents.

6.3.3.2 Preparation of Ag@$BaTiO_3$ composite nanoparticles

A barium titanium oleate precursor was prepared by mixing barium acetate, titanium (IV)-isopropoxide and oleic acid. The total concentration of precursor was 0.2 M with a molar ratio of Ba : Ti of 1 : 0.93. More experimental details about the preparation method have been given in Chapter 4 [215]. For comparison, pure $BaTiO_3$ powders were also synthesized via this method.

The above $BaTiO_3$ "organosol" precursor mixed with Ag organosol was firstly heated to ~ 90 °C with stirring for 1 h. Then this mixture solution was mixed with 4 M NaOH solution. Immediately, a dark brown slurry was formed. The excess liquid was removed by vacuum filtration, and the dried slurry was kept in a vacuum drying oven at 100 °C for 12 hours for solidification and crystallization. A series of theses mixtures was prepared keeping the Ba/Ti precursor ratio at 1.1 for all samples while the Ag precursor content was varied to obtain final two different compositions, denoted as Ag_1@$BaTiO_3$ ($BaTiO_3$: 70 mol%-77 wt%) and Ag_2@$BaTiO_3$ ($BaTiO_3$: 20 mol%-27 wt%). The dried powders were washed with methanol while performing ultrasonic treatment for 30 minutes to get rid of the "free" oleates. Ethanol / 0.2 % acetic acid (v/v $\approx$ 1:1) mixtures were used for washing under ultrasonic treatment for 20 minutes in order to remove the remaining sodium ions, as well as $BaCO_3$ impurities from the Ag@$BaTiO_3$ powders. The washed Ag@$BaTiO_3$ nanoparticles could be well dispersed in organic solvents, e. g., toluene, 1, 2-dichlorobenzene with no additional surfactant in the solution.

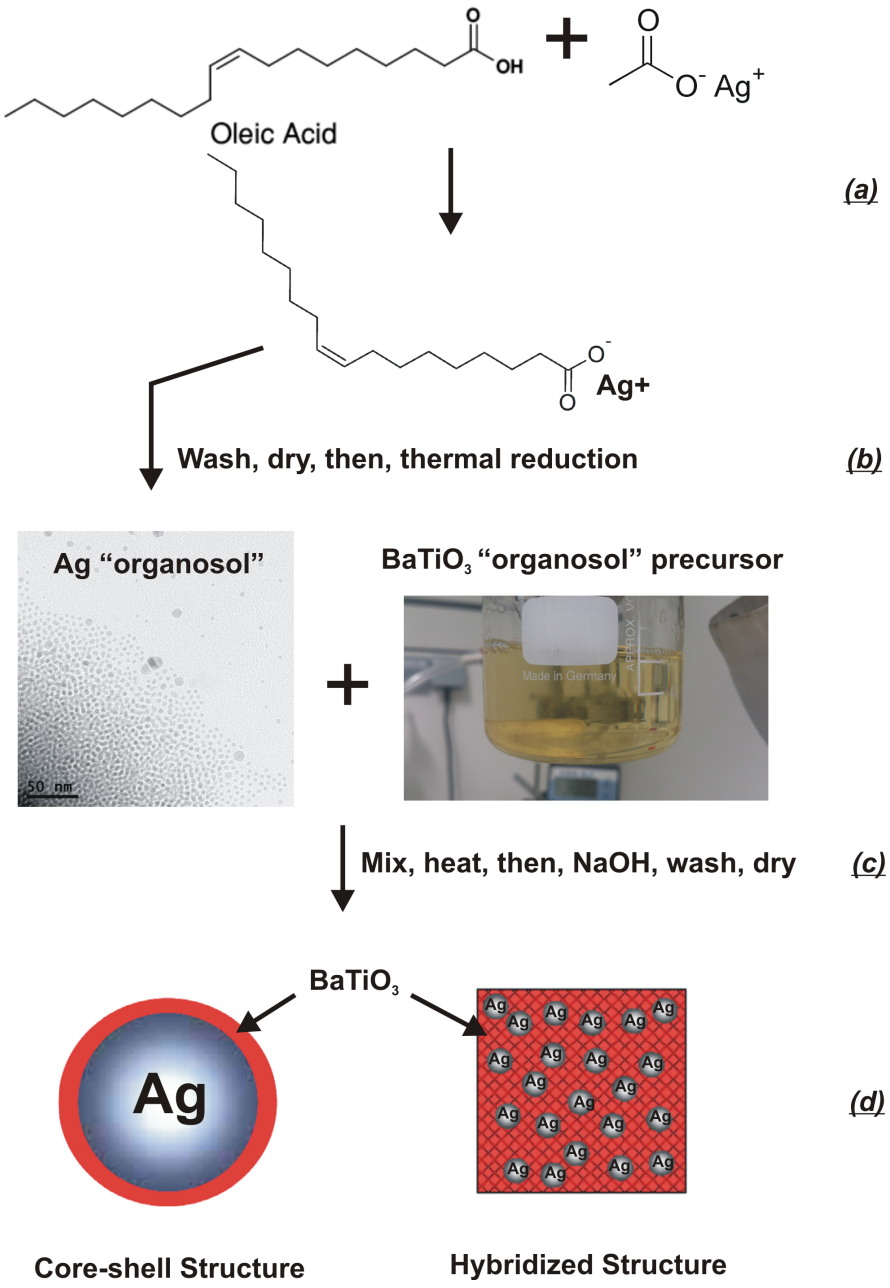

Figure 6.2: The Scheme of the preparation process of Ag@$BaTiO_3$ nanocomposites. (a) The Ag oleate precursor was prepared by the reaction of Ag acetate with oleic acid. (b) The thermal reduction of the Ag oleate precursor in oleic acid produced colloidal Ag nanoparticles. (c) The mix was heated and then added to the NaOH solution in order to create a slurry, and then drying. (d) Core-shell structure: coating of a Ag core with a dielectric $BaTiO_3$ shell. Hybridized structure: encapsulation of Ag nanoparticles within a dielectric $BaTiO_3$ matrix.

6.4 Results and discussion

We have successfully synthesized Ag organosols and Ag@$BaTiO_3$ composite nanoparticles based on the core-shell nanostructures comprising either a Ag core with a dielectric $BaTiO_3$ shell or a small amount of Ag cores dispersed in a continuous dielectric $BaTiO_3$ shell matrix, which depends on the amount of shell precursor to obtain the desired shell. The overall scheme for the synthesis route is depicted in Figure 6.2.

6.4.1 Ag organosols and their optical properties

In a typical synthesis of Ag nanoparticles, the pre-synthesized Ag oleate prepared by reacting Ag acetate and oleic acid was again added to oleic acid and dissolved at ~100 °C. When the solution was heated to 150 °C, the color of the solution changed from light yellow to dark yellow and to dark brown, indicating the formation and the concentration change of Ag nanoparticles, as indicated by the inset of Figure 6.3. Meanwhile, in order to determine the formation of Ag nanoparticles, the UV-Vis spectra were measured (Figure 6.3). At the beginning, the solution was taken after complete dissolution of Ag oleate in oleic acid. Later, when the formation of Ag nanoparticles starts, the spectra were measured.

In this way, the oleic acid acts as both the solvent to provide the thermal condition for the thermal reduction of the Ag oleate precursor, because of its relatively high boiling point and the surfactant to cap on the produced Ag nanoparticles. It can be summarized that carboxyl groups ($RCOO^-$) of oleic acid attract and encapsulate Ag ions and thus enhance the dissolution of Ag acetate in oleic acid by forming Ag oleate (See Eq. 6.1). The ionic bond between Ag^+ and $RCOO^-$ is weakened considerably by coordination between $RCOO^-$ and Ag^+. Thus, the Ag to oxygen bond energy was low enough to allow decomposition at ca. 150 °C within 4 hours [239]. The proposed mechanism of reaction could be expressed as follows:

$$RCOOH + AgC_2H_3O_2 \rightarrow RCOO^-Ag^+ + C_2H_4O_2 \uparrow \tag{6.1}$$

$$R - COO^- \rightarrow R + CO_2 \uparrow + e^- \tag{6.2}$$

$$Ag^+ + e^- \rightarrow Ag^0 \; E^0 = 0.799V \tag{6.3}$$

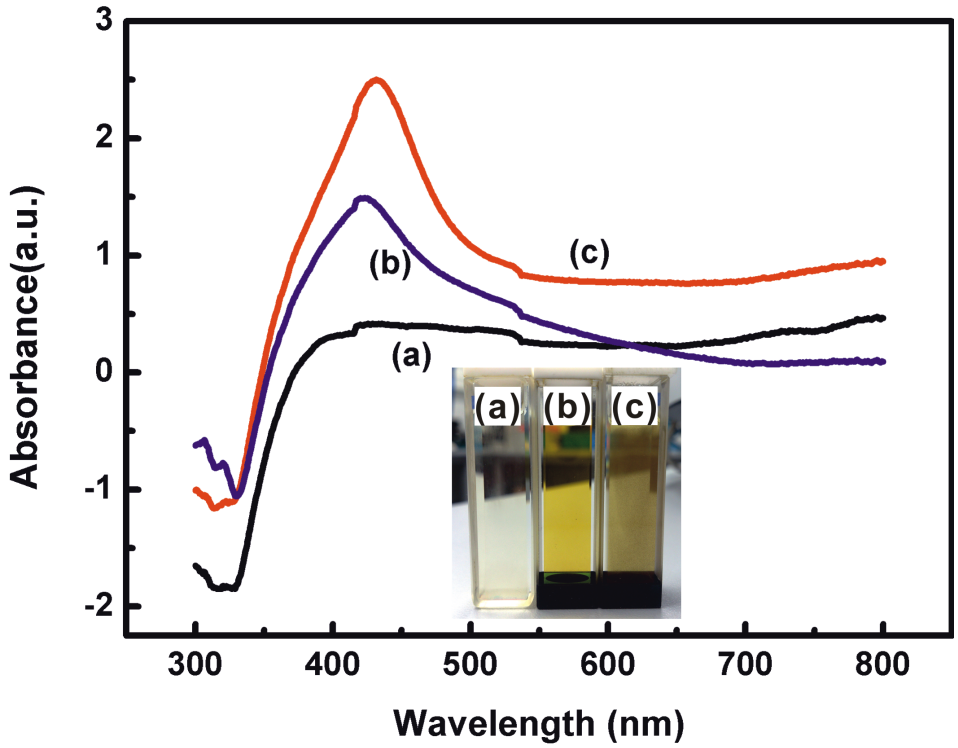

Figure 6.3: UV-Vis spectra: (a) initial components and (b), (c) evolution of absorbance spectra of oleic acid-stabilized Ag colloid. The surface plasmon band observed confirms the presence of Ag nanoparticles. The inset shows a digital image of the corresponding samples.

After the precursors decompose and react (Eq. 6.2 and Eq. 6.3), colloidal Ag nanocrystals are formed, which are stabilized in solution by the carboxylate group (COO^-) of the oleic acid coating to the surface. We utilized the XRD pattern and the UV-visible spectra as characterization criteria for the nature of the Ag colloids that form. We discuss the molecular arrangement of the oleate on the Ag surface on the basis of FTIR spectroscopy. Figure 6.4 (a) shows the XRD pattern of Ag nanoparticles. The presence of peaks at 2θ values 38.1, 44.09, 64.36 and 77.29 corresponds to (111), (200), (220), and (311) planes of Ag, respectively (JCPDS File No.: 01-1167) with the majority of particles showing (111) plane having face-centered cubic (fcc) structure. No peaks of the XRD pattern of Ag_2O and other substances appear. The UV-Vis spectrum shows a well defined surface plasmon band centered at around 420 nm (Figure 6.4 (b)). The SEM and TEM images (Figure 6.4 (d) and (e)) of this sample reveal that the majority of the sample is highly isolated Ag nanoparticles with size ranging between 10 to 20 nm.

A FTIR spectrum of the dried Ag nanoparticles is shown in Figure 6.4 (c). Bands at around 3407 cm^{-1} can be assigned as O-H stretching. The strong absorptions at 2849 and 2916 cm^{-1} are attributable to the symmetric and asymmetric C-H stretching in the aliphatic chain of the oleic acid coating, respectively. In addition, bands at 1637 and 1385 cm^{-1} can be assigned to be the assymmetric and symmetric stretching of the carboxylate group (COO^-) of the oleic acid coating, respectively. Thus, these Ag nanoparticles could be stably dispersed in organic solvents without aggregation. From Figure 6.4 (f) we can see that Ag nanoparticles in powder form show a black color, while the stable dispersion of isolated contact-free Ag nanoparticles in toluene shows a yellow color. However, in the case of water, Ag nanoparticles will aggregate to bigger clusters and then settle down on the bottom of the bottle.

6.4.2 Ag@$BaTiO_3$ nanocomposites with tailored plasmonic response

By the combination of thermal reduction and the "organosol" route core@shell Ag@$BaTiO_3$ nanostructures were successfully obtained. These core@shell Ag@$BaTiO_3$ composite nanoparticles exhibit improved physical and chemical properties arising from the combination of different chemical compositions on the nanoscale that are impossible from one component.

XRD patterns of the Ag_1@$BaTiO_3$ and Ag_2@$BaTiO_3$ composite powders are shown in Figure 6.5. The observed Bragg diffraction peaks were identified to belong either to $BaTiO_3$ (JCPDS 79-2263) or Ag (JCPDS 01-1167). From Figure 6.5, it is obvious that no other major phases than $BaTiO_3$ and Ag are present in the composite powders and the relative diffraction intensity of Ag metal increased with the addition of Ag.

For making sure that the synthesizd Ag@$BaTiO_3$ composite particles are core-shell particles, TEM and HRTEM images are shown in 6.6. There is a difference in contrast between the

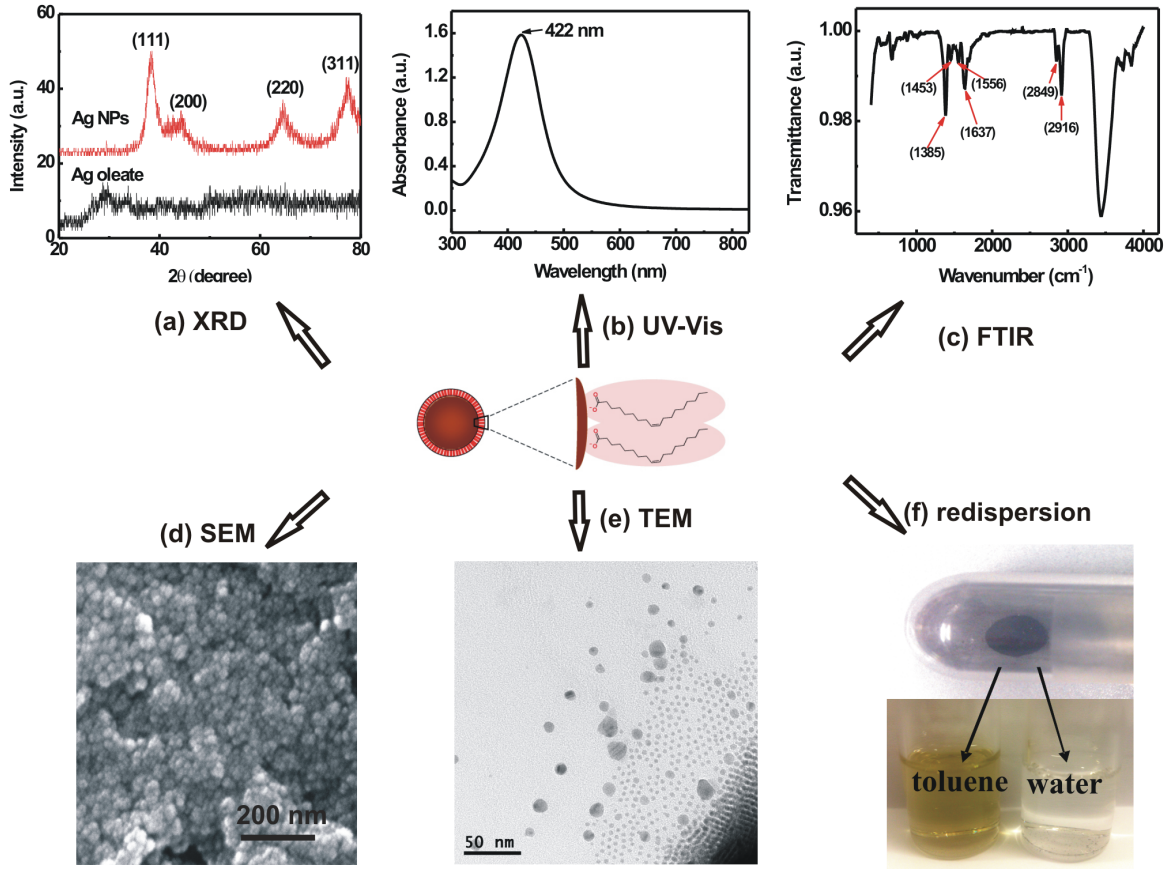

Figure 6.4: (a) XRD patterns of Ag oleate and Ag nanoparticles, (b) UV-Vis spectrum of Ag organosol in 1,2-dichlorobenzene (150 ppm), (c) FTIR spectrum, (d) SEM image and (e) TEM image of Ag nanoparticles, and (f) Ag nanoparticles in powder form and the redispersion of them in water and toluene.

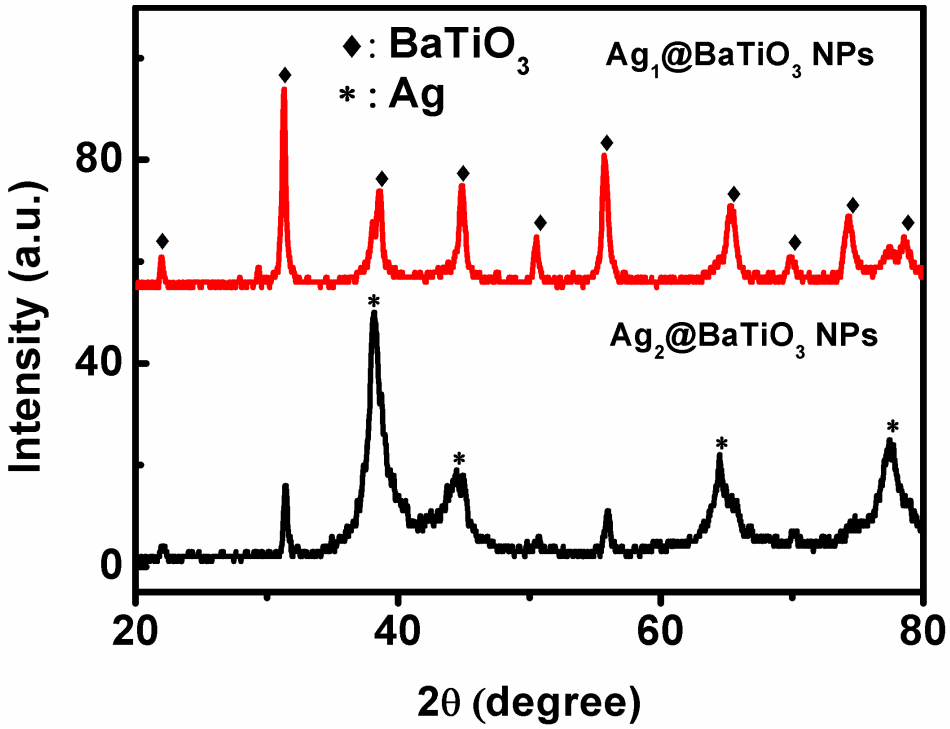

Figure 6.5: XRD patterns of Ag_1@$BaTiO_3$ and Ag_2@$BaTiO_3$ samples.

rim and the interior of the particles. From Figure 6.6 (c) it is clear that small Ag nanoparticles are embedded inside a dielectric $BaTiO_3$ matrix and Ag particles were mostly spherical in shape with an average diameter ~10 nm. For more detailed investigation of the structure, the HRTEM analysis was done. Representative images are shown in Figure 6.6 (b) and (d). The measured spacing between crystallographic planes in clearly resolved atomic lattice fringes in HRTEM images. Especially for very thin shells of less than 3 nm, HRTEM is required, as shown in Figure 6.6 (b). The core-shell structure can be further confirmed by the energy-dispersive X-ray spectrometry (EDS) analysis of an arbitrary single particle under the mode of scanning TEM (STEM), as illustrated in Figure 6.7 and 6.8. From the EDS spectrum shown in Figure 6.7 (c) and 6.8 (c), it is confirmed that the nanoparticles consist of mostly Ag, Ba, Ti and O. The presence of Cu is the contribution from the Cu grid. Here, a line-scan of the chemical compositions between the Ag core and $BaTiO_3$ shell for an individual nanoparticle was performed. As indicated in Figure 6.7 (b) and Figure 6.8 (b), the Ba L-line indicated by a Ba distribution was observed to reach a maximum at the edge of the particle, while the Ag L-line shows a maximum Ag concentration at the center of the particle. These observations demonstrate that Ag@$BaTiO_3$ exhibits a core-shell structure, in which Ag acts as the core, while $BaTiO_3$ is the shell or a small amount of Ag cores disperse in a continuous dielectric $BaTiO_3$ shell matrix.

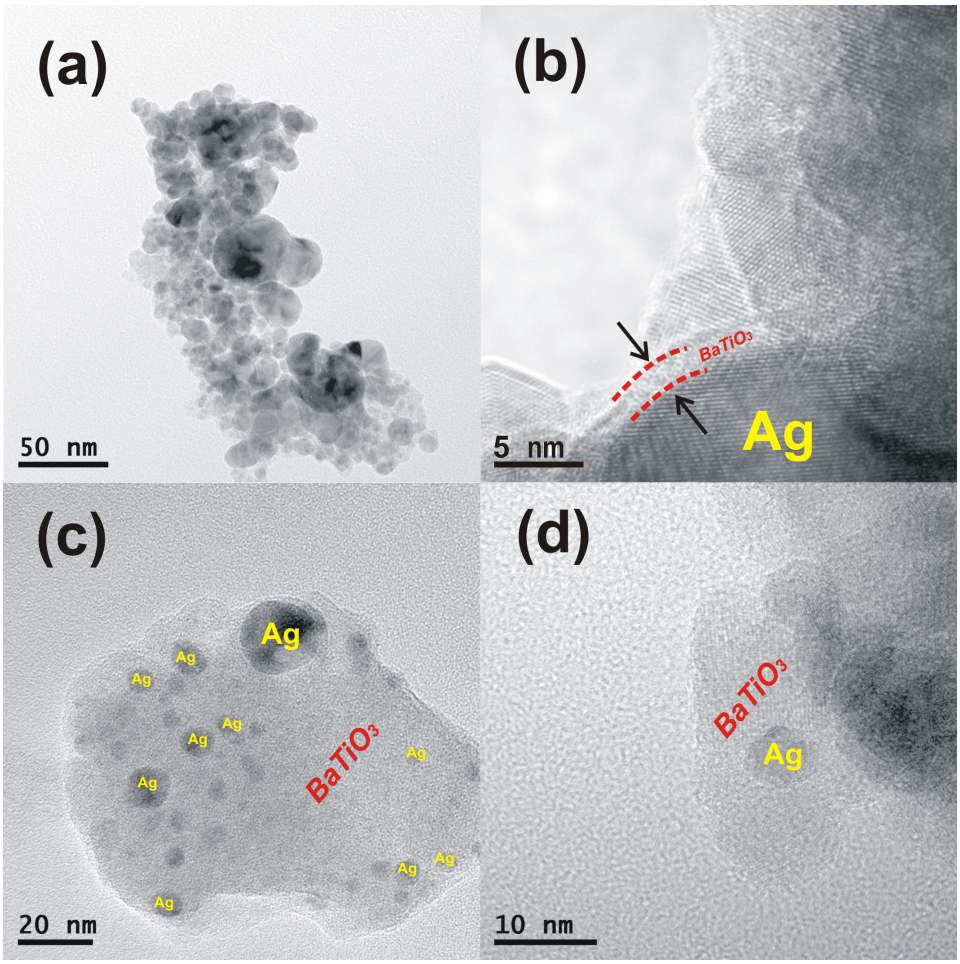

Figure 6.6: (a) TEM and (b) HRTEM images of Ag_2@$BaTiO_3$ nanocomposites, (c) TEM and (d) HRTEM images of Ag_1@$BaTiO_3$nanocomposites.

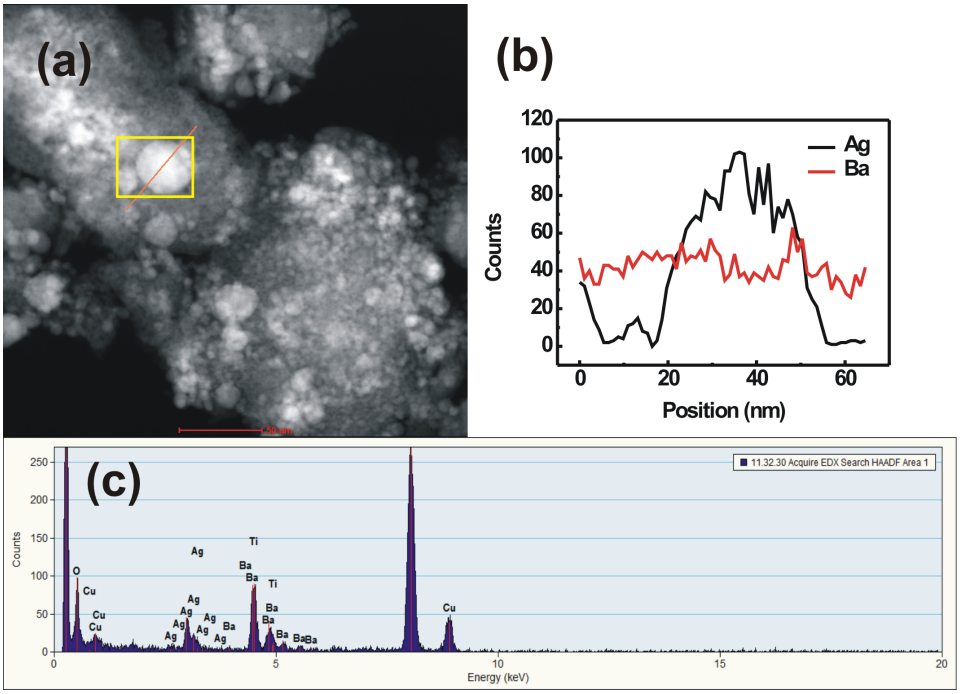

Figure 6.7: An EDS line scan of a core@shell particle. (a) STEM image of Ag_1@$BaTiO_3$ nanocomposites, (b) EDS line profile from a region marked by line in (a) showing the EDS signal intensity for Ag and Ba across the diameter of the particle, and (c) EDS spectrum of the particles. In the composition line profile, black and red represent Ag and Ba, respectively.

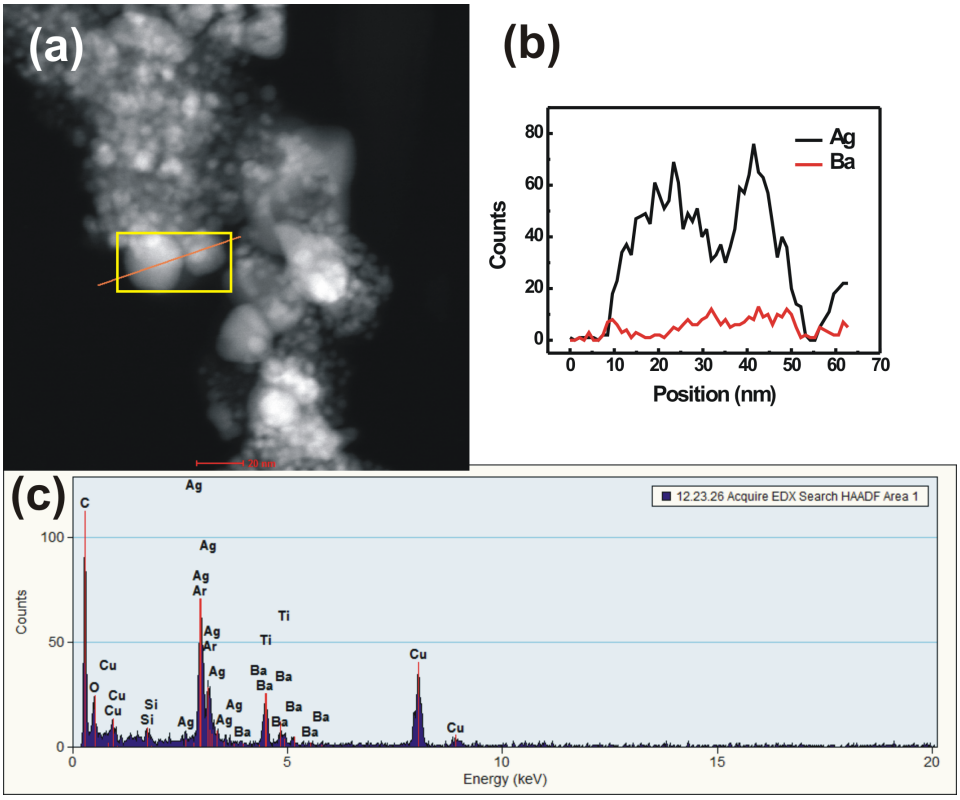

Figure 6.8: An EDS line scan of a core@shell particle. (a) STEM image of Ag_2@$BaTiO_3$ nanocomposites, (b) EDS line profile from a region marked by line in (a) showing the EDS signal intensity for Ag and Ba across the diameter of the particle, and (c) EDS spectrum of the particles taken on the region marked by box in (a). In the composition line profile, black and red represent Ag and Ba, respectively.

To evaluate how these carboxylate groups (COO^-) interact with the Ag and Ag@$BaTiO_3$ nanoparticles, FTIR spectra were recorded. The FTIR spectra of the Ag, Ag_2@$BaTiO_3$, Ag_1@$BaTiO_3$, and $BaTiO_3$ samples are displayed in Figure 6.9 (a). Infrared spectroscopy has been used to investigate the structure of long chain carboxylic acids adsorbed on oxide metal and metal surfaces [240]. In general, the COO^- groups interact directly with the nanoparticle surfaces, following Nakamoto's proposed structures for metal-carboxylate compounds [145]. According to Nakamoto, the COO^- groups interact directly with nanoparticle atoms, and the difference ($\triangle$) in wavenumbers between the asymmetric (ν_{as} (COO^-)) and symmetric (ν_s (COO^-)) bands could serve for estimating the mode of binding of carboxylate to the nanoparticle surfaces. The largest $\triangle$ values (200-320 cm^{-1}) were corresponding to a monodentate ligand and the smallest $\triangle$ values (<110 cm^{-1}) was for the chelating bidentate interaction. The medium range $\triangle$ values (140-190 cm^{-1}) were for the bridging bidentate interaction. Figure 6.9 (b) shows the peaks at around 1400 and 1600 cm^{-1} that are assigned to the symmetric ν_s (COO^-) stretch and asymmetric ν_{as} (COO^-) stretch vibrational modes, respectively. Figure 6.9 (c) shows schematic pictures of the possible adsorption models according to the values of $\triangle$. For Ag nanoparticles, the $\triangle$ value is determined to be ~ 250 cm^{-1} (1637 cm^{-1}-1387 cm^{-1}). Thus, monodentate interaction is the primary mechanism for binding COO^- groups to Ag nanoparticles. For $BaTiO_3$ nanoparticles, the $\triangle$ value (1558 cm^{-1}-1419 cm^{-1}) is ~ 139 cm^{-1}, characteristic of bridging coordination of the COO^- groups. Comparing with Ag and $BaTiO_3$ nanoparticles, both spectra of Ag_1@$BaTiO_3$ and Ag_2@$BaTiO_3$ show the characteristic of bridging coordination of the COO^- groups and the $\triangle$ values are ~ 154 cm^{-1} (1562 cm^{-1}-1408 cm^{-1}) and ~ 158 cm^{-1} (1562 cm^{-1}-1404 cm^{-1}), respectively.

The resonant frequency of a metal nanoparticle is known to be dependent on its size, shape, material properties, and surrounding medium. Particularly, the peak position of absorption in the plasmonic nanocomposite is altered by changing the matrix. As a dielectric layer covers the metallic nanoparticle, the induced screening charges on the metal-dielectric boundary reduce the plasmon excitation energy resulting in a red-shift of the resonance [241, 242]. In our cases, the core-shell geometry of the fabricated Ag@$BaTiO_3$ nanoparticles supports a SPR dependent upon Ag core size, $BaTiO_3$ shell layer thickness, and the dielectric properties of the core, shell, and refractive index of embedding medium. The UV-Vis absorption spectra of the dispersed Ag nanoparticles and the Ag@$BaTiO_3$ in 1,2-dichlorobenzene (with mean refractive index of 1.45) and ethanol (with mean refractive index of 1.36) were measured and shown in the Figure 6.10 and 6.11, respectively. The insets are the optical images of the samples. They show the corresponding change in color of the nanoparticles suspended in the 1-2 dichlorobenzene and ethanol with increasing shell layer thickness, respectively. From Figure 6.10 (a), the spectrum for the Ag nanoparticles suspended in 1,2-dichlorobenzene has a sur-

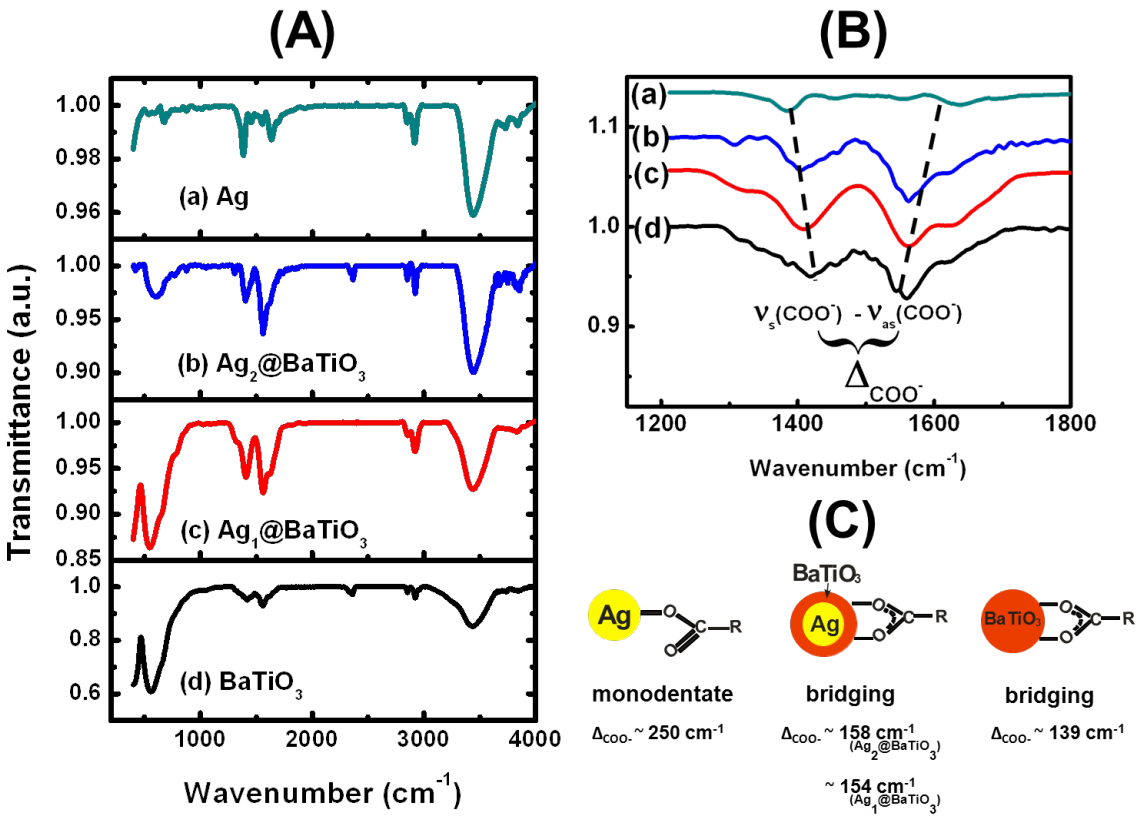

Figure 6.9: FTIR spectra of: (A) Ag (a), Ag_2@$BaTiO_3$ (b), Ag_1@$BaTiO_3$ (c), and $BaTiO_3$ (d) nanoparticles in the region between 200 - 4000 cm^{-1}. (B) FTIR spectra show details of IR bands in the 1100 - 1800 cm^{-1} spectral range. (C) Schematic pictures representing the two types of coordination of the COO^- groups to the (a-d) nanoparticles.

face plasmon absorption at 422 nm arising from the particles, and the color of the suspension was yellow, which corresponds to isolated and randomly oriented spherical Ag colloidal dispersions. In contrast, the absorbance of the Ag nanoparticles in ethanol is red-shifted from 422 to 469 nm, the peak decreases in intensity and shows a broad absorption in the region 400-600 nm, indicating aggregation of Ag nanoparticles due to low dispersion stability in ethanol [243, 244].

The suspension of Ag_1@$BaTiO_3$ nanoparticles exhibits an surface plasmon absorption peak centered at around 475 nm (Figure 6.10 (c)) and at around 456 nm (Figure 6.11 (c)), respectively, which is substantially red-shifted from that of pure Ag nanoparticles (about 420 nm). This shift can be understood in terms of the change in the refractive index of the surrounding medium. Based on Mie theory [245, 246] when the refractive index of the environment on the surface of the metal increases, a red shift will happen. The addition of the $BaTiO_3$ shell can be also thought of as a change in the effective refractive index of the medium ($BaTiO_3$, refractive index: 2.5) compared to Ag neighboring the liquid (1,2-dichlorobenzene, refractive index: 1.45; ethanol, refractive index: 1.36). Thus, the shell material and thickness of the shell affect the magnitude of the shift as has been recently shown also experimentally for many metal-oxide core-shell combinations [233]. In addition to the plasmon peak shifts, more remarkably, a significant broadening of the SPR in the Ag_2@$BaTiO_3$ nanoparticles was observed (Figure 6.10 (b) and Figure 6.11 (b)), which should be due to plasmon coupling between nanoparticles. The ensemble of nanoparticles, which are no more distant from each other than the diameter of each individual particle, could strongly trap the incident light in a sub-wavelength scale (gap between the nanoparticles) which could create a huge localized field. The spectrum of such groups of nanoparticles is determined by the interaction between the individual localized surface plasmon resonances (LSPR). The interaction between nanoparticles, e.g. dipole-dipole depends upon the separation between neighbouring particles. The thick coating leads to larger separation of the metal particles, whereas thin coating leads to lesser separation. In this case, $BaTiO_3$ shell acts as a barrier layer preventing the metal cores from direct contact. K.-H. Su et al. observed that the resonant peak had significantly red-shifted for short particle spacing indicating strong plasmon coupling, and the peak shift decayed rapidly with increasing particle spacing. If the particles are well separated (thick coating), the dipole-dipole coupling is fully suppressed and the plasmon band is located nearly at the same position as the individual metal particle bared [247, 248]. If the particles are densely packed so that the individual particles are electronically coupled to each other (thin coating), the SPR is drastically changed and results in complete absorption of light in a broad frequency range. Therefore, we can conclude that the sample Ag_2@$BaTiO_3$ is an ideal plasmonic blackbody that absorbs all light that falls onto it. Being a perfect absorber,

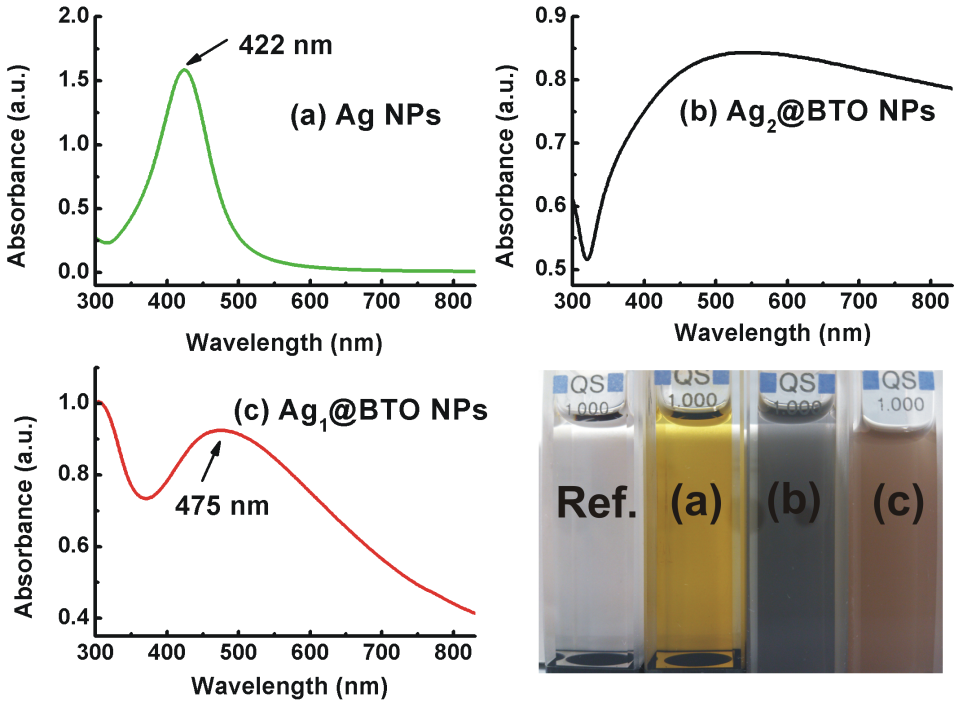

Figure 6.10: UV-vis absorption spectra in 1,2-dichlorobenzene of (a) Ag colloidal solution, characteristic SPR of $\lambda = 422$ nm, (b) $Ag_2@BaTiO_3$, (c) $Ag_1@BaTiO_3$, characteristic SPR of $\lambda = 475$ nm. The concentrations of the samples in these cases are 150 ppm. Optical resonances of gold shell-silica core nanoshells as a function of their core/shell ratio. The inset shows a digital image of the corresponding samples.

$Ag_2@BaTiO_3$nanoparticles could be valuable for many important applications, e.g., photodetection or collection of solar energy (photovoltaic cells).

In order to give the supporting experimental evidence of Ag cores embedded in $BaTiO_3$ matrix as the origin which gives rise to an enhancement in the relative permittivity of Ag-based two-phase composites, the electrical measurements were performed as a function of both frequency and temperature on the samples: pure $BaTiO_3$, $Ag_1@BaTiO_3$ and $Ag_2@BaTiO_3$. However, for the pressed $Ag_2@BaTiO_3$ powder, the negative value of dielectric permittivity was observed at all measurement frequencies. This phenomenon arises from a high electric conductivity, which goes beyond the measuring limit of the impedance analyzer, giving rise to meaningless data. The high electric conductivity also results in very high dielectric dissipation factor ($tan\delta$), as a result of an overflow of its value (above the measurement limit). Therefore the high electric conductivity of $Ag_2@BaTiO_3$ powder makes it impossible to characterize its dielectric permittivity even at the room temperature. As is well known, based on the mixture rules and percolation theory, beyond a certain volume fraction of the conducting phase the conducting particles start to form an electrically conducting network inside the composite,

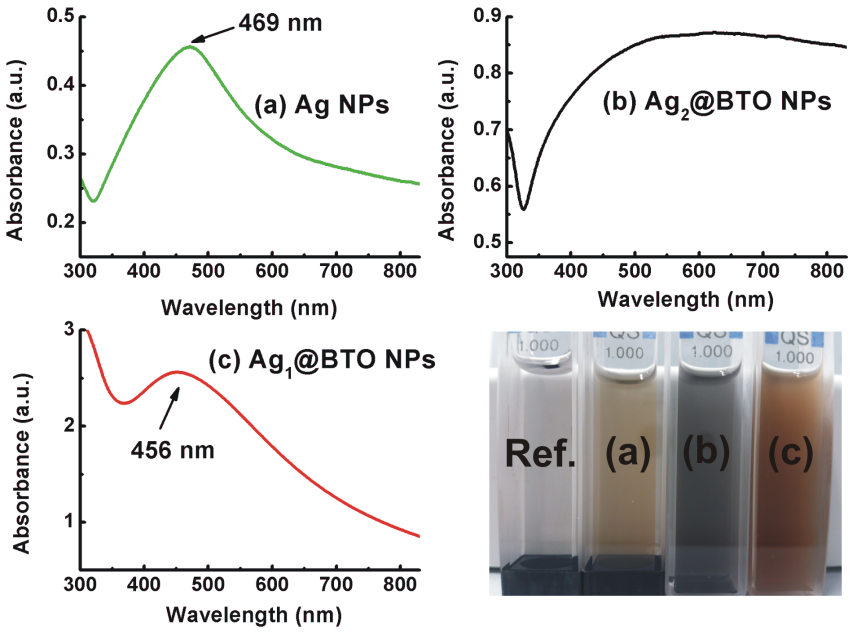

Figure 6.11: UV-vis absorption spectra in ethanol of (a) Ag colloidal solution, characteristic SPR of λ = 469 nm, and the broadening of peak indicated that the particles were polydispersed, (b) Ag_2@$BaTiO_3$, and (c) Ag_1@$BaTiO_3$, characteristic SPR of λ = 456 nm. The concentrations of the samples in these cases are 150 ppm. The inset shows a digital image of the corresponding samples.

and it undergoes a transition from an isolating to a conducting material. As shown in Figure 6.12, Ag_2@$BaTiO_3$ is a sample, which displays a temperature independent conductive behavior in its complex impedance with positive real and imaginary parts and both approach zero. Figure 6.13 (a) and (b) show the plot of imaginary part (Z") versus real part (Z') of complex impedance taken over the frequency range 0.1Hz - 1MHz at different temperatures 300 K $\leq$ T $\leq$ 420 K for the $BaTiO_3$ and Ag_1@$BaTiO_3$ samples. This type of electrical behavior can be interpreted as the result of a parallel combination of bulk resistance (RB) and bulk capacitance (CB) elements, where the non-zero intercept at high frequency provides an estimation of the resistance of the bulk of the grains (RB), which is approximately RB ($BaTiO_3$) ~ 206 Ω and RB (Ag_1@$BaTiO_3$) ~ 316 Ω, respectively (Figure 6.13 (c)). The intercept, RB, is not significantly affected by the temperature. However, the semicircle for the grain bulk is not observed, the only observable arc appears at the higher temperature ($\geq$ 360 K). At lower temperature ($\leq$ 340 K), there is a linear response in Z". This trend indicates the good insulating behavior in the sample.

The temperature and frequency dependences of dielectric permittivity (ε_{eff}) and dielectric loss ($tan\delta$) of the $BaTiO_3$ and Ag_1@$BaTiO_3$ samples are shown in Figure 6.14 (a-d). It is evident that the values of ε_{eff} and $tan\delta$ remain almost constant with increase in temperature at 100 kHz and weak frequency dependence at 300 K is also noticed for both the samples. As expected especially, an increase in ε_{eff} with the Ag content is observed at all temperatures and frequencies. Ag nanoparticles in the $BaTiO_3$ matrix act as polarizable dipoles and consequently enhance interfacial polarization.

In fact, the compacted powder is as an air-particle mixture or unsaturated medium, made up of surrounding air and solid nanoparticles. Several dielectric mixture equations for calculating the nanoparticle permittivity, $\varepsilon_{particle}$, from measured effective permittivity of compacted samples have been summarized by Nelson [249] as follows:

1. Complex Refractive Index (CRI) mixture equation:

$$\varepsilon_{particle} = \left(\frac{\sqrt{\varepsilon_{eff}} + \alpha_{particle} - 1}{\alpha_{particle}} \right)^2 \tag{6.4}$$

2. Landau and Lifshitz, Looyenga (LLL) equation:

$$\varepsilon_{particle} = \left(\frac{\varepsilon_{eff}^{\frac{1}{3}} + \alpha_{particle} - 1}{\alpha_{particle}} \right)^3 \tag{6.5}$$

3. Böttcher equation:

$$\varepsilon_{particle} = \frac{\varepsilon_{eff}\left(3\alpha_{particle} + 2\left(\varepsilon_{eff} - 1\right)\right)}{3\alpha_{eff}\varepsilon_{eff} - \left(\varepsilon_{eff} - 1\right)} \tag{6.6}$$

4. Bruggeman-Hanai equation:

$$\varepsilon_{particle} = \frac{1 - \alpha_{particle} - \varepsilon_{eff}^{\frac{2}{3}}}{1 - \alpha_{particle} - \varepsilon_{eff}^{-\frac{1}{3}}} \tag{6.7}$$

5. Rayleigh equation:

$$\varepsilon_{particle} = \frac{\alpha_{particle}\left(\varepsilon_{eff} + 2\right) + 2\left(\varepsilon_{eff} - 1\right)}{\alpha_{particle}\left(\varepsilon_{eff} + 2\right) - \left(\varepsilon_{eff} - 1\right)} \tag{6.8}$$

where ε_{eff} is the effective dielectric constant of the air-particle mixture; $\varepsilon_{particle}$ is taken as the dielectric constant of the particles; and $\alpha_{particle}$ is the volume fraction of the solid nanoparticles, then is given by $\frac{\rho_{mixture}}{\rho_{theory}}$. In the present case, the air-particle mixture density $\rho_{mixture}$ of the $BaTiO_3$ and Ag_1@$BaTiO_3$ powder in the compressed state was found to be 3.52 and 3.89 gcm^{-3}, respectively, and $\alpha_{particle}$ was calculated to be 0.59 and 0.58, respectively.

The measured frequency dependent ε_{eff} (Figure 6.14 (c)) and results of estimations for the nanoparticle permittivities calculated from different dielectric mixture equations are shown in Figure 6.15. Comparisons of the calculated and measured permittivities for the samples, the Böttcher, CRI and LLL mixture equations appear to be the most reliable equations for estimating solid material permittivities from measurements on these nanoparticle materials. The present values from the CRI Eq. 6.4 and Böttcher´ Eq. 6.6 are in excellent agreement with each other for both the samples, and the values from the LLL Eq. 6.5 show an increasing trend, for example, at 1MHz, the estimated Ag_1@$BaTiO_3$ permittivities are 121 (CRI), and 163 (LLL), respectively, whereas the Bruggeman-Hanai Eq. 6.7 and Rayleigh Eq. 6.8 give estimated negative values. Negative values have no physical meaning for ε_{eff} and are a mathematical artifact. These discrepancies might be the result of an inaccurate estimation of sample volume fraction. It may also indicate that the additional contribution from the conductivity into measured, ε_{eff}, for the pressed powder is not negligible even at high frequencies.

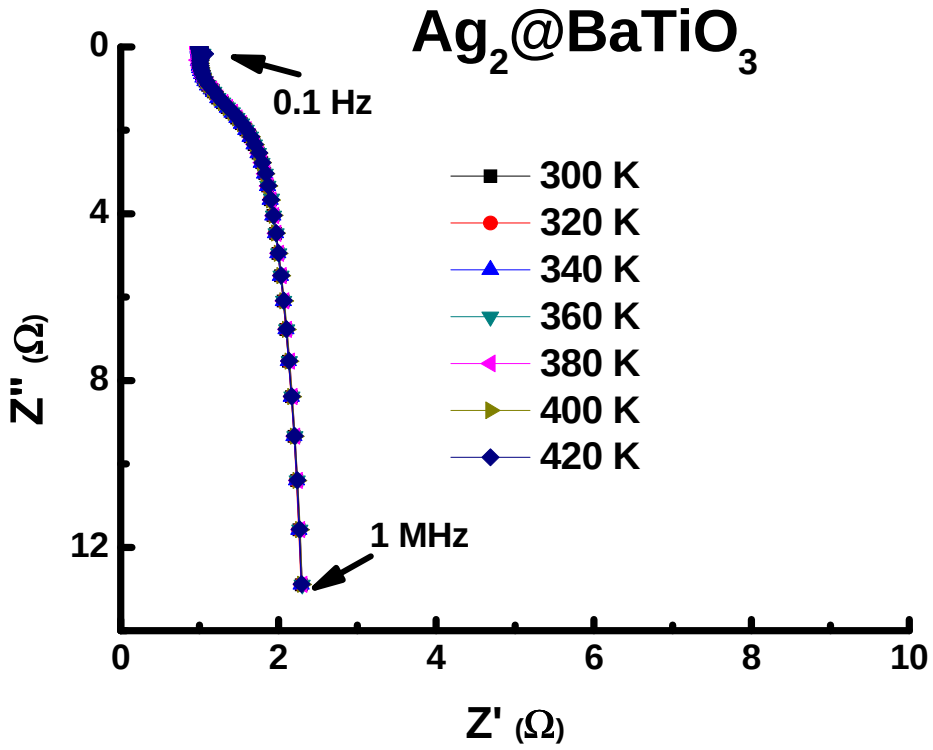

Figure 6.12: Represents complex impedance plots of Z" (Ω) vs. Z' (Ω) at various temperatures for a conducting sample of Ag_2@$BaTiO_3$.

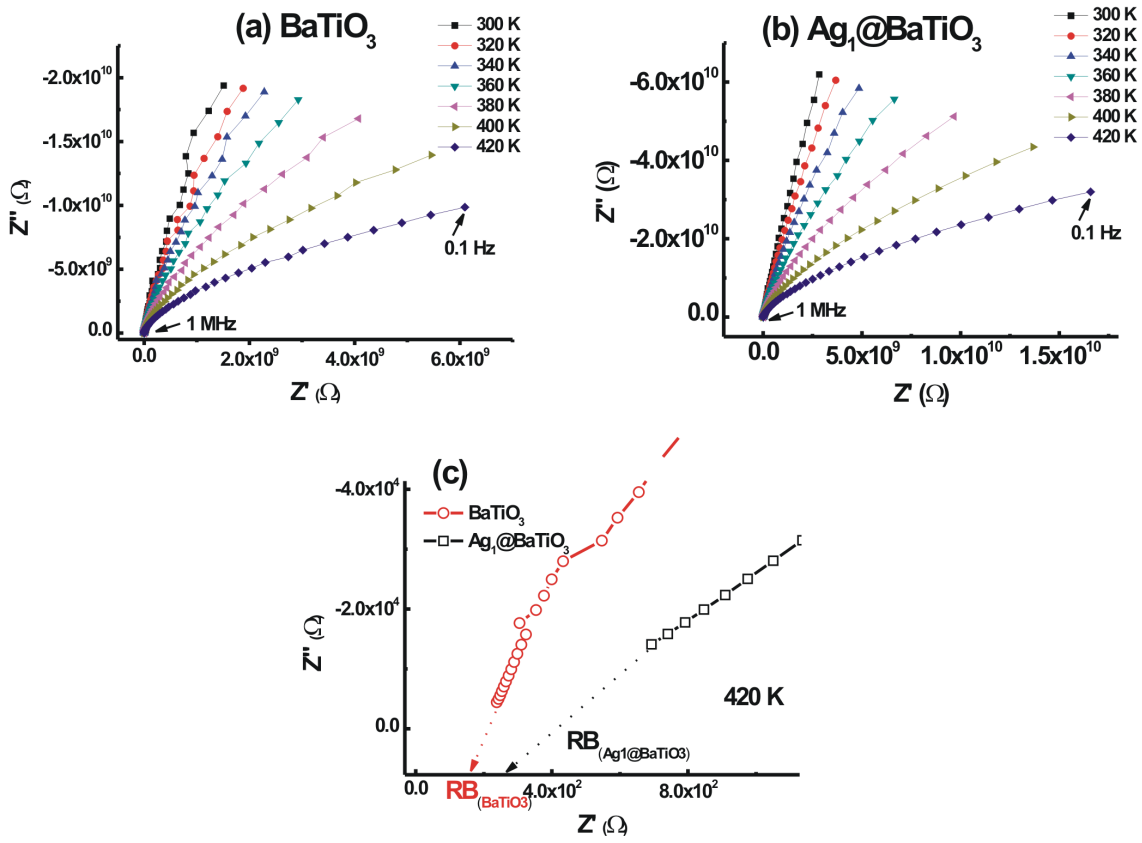

Figure 6.13: Complex impedance plots of Z" (Ω) vs. Z' (Ω) at various temperatures for (a) $BaTiO_3$ and (b) Ag_1@$BaTiO_3$, and (c) shows an expanded view of the high frequency data close to the origin.

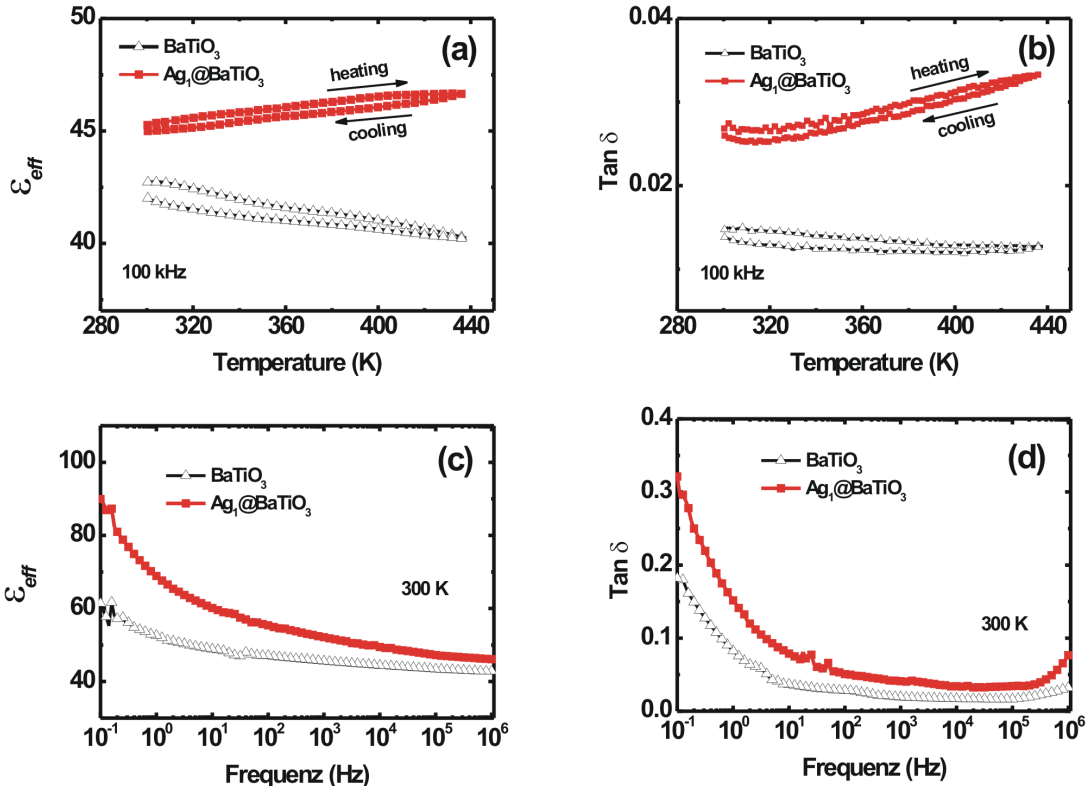

Figure 6.14: Temperature dependence of (a) the dielectric permittivity, ε_{eff}, and (b) loss, $tan\delta$, at 100 kHz, and frequency dependence of (c) the dielectric permittivity, ε_{eff}, and (d) loss, $tan\delta$, at 300 K for the $BaTiO_3$ and $Ag_1@BaTiO_3$ samples.

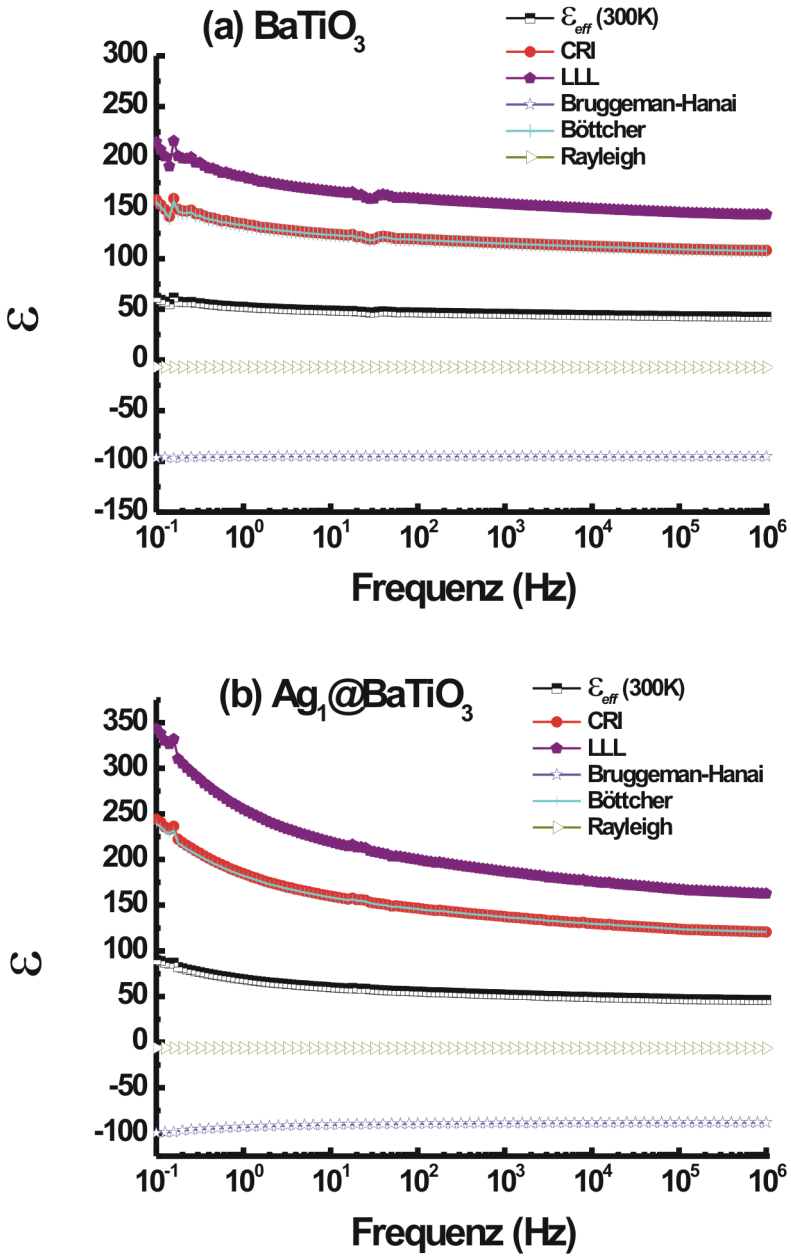

Figure 6.15: Comparisons of the measured ε_{eff} and calculated ε permittivities from the different dielectric mixture equations for the nanoparticles (a) $BaTiO_3$ and (b) Ag_1@$BaTiO_3$.

6.5 Conclusions

In summary, Ag nanoparticles were successfully synthesized via thermal reduction of a Ag^+-oleate complex, which was prepared by the reaction of Ag acetate and oleic acid, in the highly concentrated organic phase because oleic acid was used as both a dissolving solvent and a capping molecule. Also, the produced Ag nanopowders can be easily dispersed in various organic solvents. By the combination of the thermal reduction of silver ions to silver nanoparticles and the "organosol" route of barium titanate, we were developing a novel $Ag@BaTiO_3$ with tunable optical properties based on the core-shell nanostructure comprising either a Ag core with dielectric $BaTiO_3$ shell or a small amount of Ag cores dispersed in a continuous dielectric $BaTiO_3$ shell matrix, which depends on the amount of shell precursor to obtain the desired shell. With precise synthesis and coating, we are able to tune the SPR peak of the $Ag@BaTiO_3$ nanoparticles through adjustments of the core/shell ratio in the particle.

FT-IR results confirm that an organic layer exists and the carboxylic acids (COO^-) are thought to bind to Ag and $Ag@BaTiO_3$ nanoparticles through monodentate and bridging modes, respectively, based on the difference ($\triangle$) in wavenumbers between the asymmetric (ν_{as} (COO^-)) and symmetric (ν_s (COO^-)) bands. The UV-vis results reveal changes in the optical features of the Ag and $Ag@BaTiO_3$ composite nanoparticles corresponding to the medium where the nanoparticles are embedded in and the thickness of the $BaTiO_3$ shell. It was found that the ultrathin $BaTiO_3$ shell with a thickness less than 5 nm in composite significantly alters the optical response of the designed metamaterials and results in almost complete absorption of light in broad spectrum.

Chapter 7

Conclusion and Future Work

This chapter is divided into three main sections; the first section details the conclusions that can be drawn from the results presented in Chapters 4, 5, and 6 on the preparation of $BaTiO_3$, core@shell $BaTiO_3$@SiO_2 nanoparticles, and finally core@shell Ag@$BaTiO_3$ nanoparticles. Section 7.2 details potential improvements that could be made to this work. The final section outlines possible future work that could follow on from this work.

7.1 Main Conclusions

The main interest of this dissertation thesis relies on the synthesis and processing of core@shell nanostructured materials by using wet chemical method. The coating process can be used to stabilize nanoparticles with e. g. ferroelectric, magnetic, as well as optical properties, allowing us to develop new materials for use in microelectronic devices and magneto-optical sensors [250]. In the thesis, the first process to prepare the nanocrystalline $BaTiO_3$ nanoparticles was proposed using the "organosol" route. The resulting $BaTiO_3$ powders were characterized in terms of crystal structure, the crystallite and particle size, morphology, the lattice parameter *a*-axis, particle formation process, and dielectric properties. Further efforts were made in the designing and the controlled preparation of core-shell nanostructured particles with as-prepared $BaTiO_3$ that was able to be used both as the core and the shell material according to different purposes. Two types of core-shell nanoparticles have been investigated, namely: $BaTiO_3$ crystalline core@SiO_2 amorphous nanoshell and Ag crystalline core@$BaTiO_3$ crystalline nanoshell composite nanoparticles. Typical core-shell structure of the nanoparticles was revealed by HRTEM analysis. The UV absorption spectra of core-shell nanostructure clearly indicate the variation in the electronic structure due to the surface modifcation. Based on the results and discussion presented in this thesis, the following summaries or conclusions can be drawn:

1. As-prepared $BaTiO_3$ powders with a particle size ca.10~15 nm and high content of cubic phase could be successfully synthesized in oleic acid solution with the "organosol" route process. Oleic acid was employed as both solvent and capping agent in the process. This resulted in nanoparticles with a hydrophobic coating since the polar end groups were attached to the surface, thus, they formed a protective monolayer, which is necessary for making monodisperse and highly uniform nanoparticles.

2. Results from XRD showed both the crystallite size and the lattice parameter of the $BaTiO_3$ powders first expand as the reaction temperature is increased to 40 °C and then shrink with increasing reaction temperatures up to 100 °C. One possible explanation of the findings is assumed to result from lattice defects, due to OH^- incorporation in the unit cell. A second explanation can be found in an increased influence of surface tension on the lattice parameter for nano-sized particles.

3. Both $BaTiO_3$ particle growth and the conversion of existing spheres to cubes occurred, resulting in the formation of significantly larger particles in an organic environment during calcination, meanwhile, their structures were changed to the tetragonal phase, which is ferroelectric. However, the particles of cubic or brick shape with sizes of 1~2 μm were observed, the exact chemistry reason of this process remains an open question at this point.

4. Core@shell $BaTiO_3$@SiO_2 nanostructures were successfully synthesized in a reverse microemulsion with a composition of Triton X-100/1-hexanol/cyclohexane/H_2O in which $BaTiO_3$ can be functionalized with uniform SiO_2 shell. To our knowledge, this is the first time that the SiO_2 nanoshells coated $BaTiO_3$ have been experimentally synthesized using a reverse microemulsion method. Furthermore, we could easily control the SiO_2 thickness in the range from 3 to 20 nm with just changing the molar ratio of TEOS/ $BaTiO_3$ from 56:1 to 5.6:1. SiO_2 as a shell material can further contribute to the fabrication of a high-performance core-shell catalyst that has the combined advantages of different materials.

5. In the core@shell $BaTiO_3$@SiO_2, amorphous SiO_2 shells have surfaces decorated with OH groups that renders intrinsically hydrophilic. The hydrophilic surfaces easily adhere to each other through hydrogen bonding and form irregular agglomerations. In order to decrease these agglomerations of particles, the surface of the silica shell should be modified with the coupling agents, such as vinyltriethoxysilane.

6. The synthesis of the core@shell Ag@$BaTiO_3$ nanoparticles was carried out in two steps: the synthesis of a Ag organosol, followed by its incorporation with $BaTiO_3$ "organosol"

precursor to prepare Ag@$BaTiO_3$ nanoparticles. Other products were not detected, according to XRD results.

7. $BaTiO_3$ was used as a shell material in order to tune the surface features of Ag nanoparticles with the aim to achieve strong light absorption in a broad spectral region, which can be achieved by fabricating the $BaTiO_3$ shell as thin as possible. These core@shell materials could be used in photovoltaic applications because they can both absorb sunlight and separate photogenerated excitons into free charges. These combined properties could make these new materials more efficient at first trapping and then utilizing more of the solar spectrum than previous components of solar conversion devices.

Overall, this dissertation provides insights to novel colloidal preparation routes to synthesize nanomaterials of discrete sizes, high surface area, different elemental composition and specific core-shell geometric structures.

7.2 Improvements

There are a number of ways in which the work carried out here could be improved. Firstly, by using materials of higher quality, for example, in this work oleic acid of 65-88% purity was used, but oleic acid of 99% purity is available. When using reagents of lower purity, the synthesis results may be erratic and the fine control over the absolute size and shape of the nanoparticles was lost. Because of compositional differences between the oleic acid of different purity, there is e. g. a possibility that the low-grade oleic acid contain fatty acids of varying chain lengths, that result in barium-titanium oleate precursors with different chemical properties. However, using the purity of the reagents this could potentially offer an good control in the particle size and shape and enable the particle shape to be tuned in a reproducible manner, from spheres to cubes during calcination. Secondly, the dispersion of dry particles in liquids is usually used to prepare zetal potential, TEM or UV-Vis measurements. To make stable dispersions it is necessary to disperse the large agglomerates that form the initial dry powder into primary particles. In this work, ultrasonic bath was used to disperse nanoparticles. However, heat is a natural byproduct when operating an ultrasonic bath because ultrasonic energy is transformed into heat. In this case ultrasonic bath should be cooled, because bath temperature plays a key role in the quality nanoparticle dispersion. The dispersed nanoparticles have a tendency to re-agglomerate with rising temperatures. The ultrasonic equipment -Elmasonic S units offered by Tovatech is ready to help solve this problem through an optional cooling coil containing tap water and connected to a temperature regulating device used to maintain the optimum ultrasonic bath temperature.

7.3 Future Work

We believe that the research pursued in this dissertation project lays the groundwork for other work in the field of nanomaterial synthesis and applications. In future the following work can be done,

1. The valuable insights gained from the preparation of $BaTiO_3$ nanoparticles with precise control of size can be extended to synthesize other perovskite oxides nanoparticles, such as $SrTiO_3$, $PbTiO_3$, $PbZrO_3$, as well as (Ba,Sr)TiO_3.

2. In the core@shell $BaTiO_3$@SiO_2, it is necessary to optimize the reaction conditions to improve the thickness and quality of the SiO_2 coatings on the $BaTiO_3$ nanoparticles. Furthermore, the dielectric permittivity of core@shell $BaTiO_3$@SiO_2 nanoparticles with different shell thickness will be studied. Additionally, effects of SiO_2 coating on sintering behavior and microstructural properties of $BaTiO_3$ nanopowders will also be continuously discussed and investigated.

3. Other shell materials can be used to coat the $BaTiO_3$ nanoparticles where SiO_2 is replaced by a different material, like Al_2O_3, TiO_2 or ZrO_2. Techniques developed for TiO_2 nanoshell can be expanded to fabricate new material composites containing TiO_2 coatings with high surface area. These coatings can be used to not only enhance the material properties but also to diversify the applications of the resulting composites. For example, a crystalline, ultrathin TiO_2 shell layer encapsulates $BaTiO_3$ nanoparticles. Significant effects of this ultrathin TiO_2 shell on the resulting dielectric behaviors and energy density of the nanocomposite were observed [251]. In addition, the stable crystalline TiO_2 ultrathin shell showed strong interaction with the polymer matrix and the $BaTiO_3$ nanoparticles, which enhanced the dispensability of particles in the polymer matrix.

4. Further investigations are incorporating the $BaTiO_3$-based composite nanoparticles (e. g. $BaTiO_3$@TiO_2, $BaTiO_3$@SiO_2, or Ag@$BaTiO_3$) into polymer matrix followed by dip coating, spin coating, or solvent casting into thin films. In general, dielectrics with stable and adjustable dielectric properties of high dielectric constant and low leakage current are always desired. It is well known that blending high dielectric inorganic ceramic materials into polymers can lead to higher effective dielectric constants and thus increase the energy density. For our investigations we will choose PVDF trifluoroethylene (P(VDF-TrFE)) of VDF to TrFE molar ratio 70/30 as the matrix material. P(VDF-TrFE) is the most useful polymer because of the low poling field required to

give ferroelectric behavior and high dielectric permittivity, compared with other ferroelectric polymers. Another important point is that this copolymer does not require any mechanical stretching before the poling process. The relative permittivity (ε_r) of the $BaTiO_3$ based nanoparticles/(P(VDF-TrFE)) composites will increase prominently with the increase of nanoparticles loading amount, which still results in low dielectric loss and low leakage current, as already reported by [252–255].

5. The last but most important part of the future research is developing nanomaterials that combine plasmons and ferroelectric properties, which could make these materials a better choice for various technological applications. As mentioned in chapter 6, $Ag@BaTiO_3$ composite nanoparticles may be a potential promising alternative material for future photovoltaic applications. Black and coworkers have demonstrated the the benefit of adding ferroelectric nanoparticles such as $SrTiO_3$ or $BaTiO_3$ to the active layer to overcome coulomb attraction between opposite charge carriers and to achieve their full dissociation for achieving higher power conversion efficiency [256]. Therefore, we are anticipating that $Ag@BaTiO_3$ composite nanoparticles may also offer one route towards the efficient organic photovoltaic devices. The following research is implementing $Ag@BaTiO_3$ nanoparticles with varied Ag content or $BaTiO_3$ shell thickness within the photoactive layer, P3HT:PCBM based organic solar cells, and the improvement in the efficiency of the device is expected through the optimization of the nanoparticle content in comparison with the same blend without these nanoparticles.

References

[1] Frank Wei and Ian Burn. Core-shell structured dielectric particles for use in multilayer ceramic capacitors, November 6 2008. US Patent App. 12/291,153.

[2] Jin Dai, Fei Ye, Yiting Chen, Mamoun Muhammed, Min Qiu, and Min Yan. Light absorber based on nano-spheres on a substrate reflector. *Optics express*, 21(6):6697–6706, 2013.

[3] Xiaohua Liu. *Synthesis, fabrication and characterization of magnetic and dielectric nanoparticles and nanocomposite films*. PhD thesis, CITY UNIVERSITY OF NEW YORK, 2014.

[4] Anthony J Moulson and John M Herbert. *Electroceramics: materials, properties, applications*. John Wiley & Sons, 2003.

[5] Pradeep P Phule and Subhash H Risbud. Low-temperature synthesis and processing of electronic materials in the BaO-TiO_2 system. *Journal of materials science*, 25(2):1169–1183, 1990.

[6] Shinn-Jen Chang, Wei-Sheng Liao, Ci-Jin Ciou, Jyh-Tsung Lee, and Chia-Chen Li. An efficient approach to derive hydroxyl groups on the surface of barium titanate nanoparticles to improve its chemical modification ability. *Journal of colloid and interface science*, 329(2):300–305, 2009.

[7] Sumio Sakka. *Handbook of sol-gel science and technology. 1. Sol-gel processing*, volume 1. Springer, 2005.

[8] Horacio E Bergna and William O Roberts. *Colloidal silica: fundamentals and applications*. CRC Press, 2005.

[9] Kathryn ML Taylor-Pashow, Joseph Della Rocca, Rachel C Huxford, and Wenbin Lin. Hybrid nanomaterials for biomedical applications. *Chemical Communications*, 46(32):5832–5849, 2010.

[10] RK Iller. The chemistry of silica: solubility, polymerization, colloid and surface properties, and biochemistry. *New York, Cap*, 1(2), 1979.

[11] K Lance Kelly, Eduardo Coronado, Lin Lin Zhao, and George C Schatz. The optical properties of metal nanoparticles: the influence of size, shape, and dielectric environment. *The Journal of Physical Chemistry B*, 107(3):668–677, 2003.

[12] Aoife C Power, Anthony J Betts, and John F Cassidy. Non aggregated colloidal silver nanoparticles for surface enhanced resonance raman spectroscopy. *Analyst*, 136(13):2794–2801, 2011.

[13] A. Ben-Yakar and R.K. Harrison. Methods and compositions related to dielectric coated metal nanoparticles in thin-film opto-electronic conversion devices, February 5 2015. US Patent App. 14/449,751.

[14] Bala Krishna Juluri, Jun Huang, and Lasse Jensen. Extinction, scattering and absorption efficiencies of single and multilayer nanoparticles, Jan 2010.

[15] Shekhar Agnihotri, Soumyo Mukherji, and Suparna Mukherji. Size-controlled silver nanoparticles synthesized over the range 5–100 nm using the same protocol and their antibacterial efficacy. *RSC Advances*, 4(8):3974–3983, 2014.

[16] Zhengxia Xu and Guoxin Hu. Simple and green synthesis of monodisperse silver nanoparticles and surface-enhanced raman scattering activity. *RSC Advances*, 2(30):11404–11409, 2012.

[17] Dieter Vollath. Bifunctional nanocomposites with magnetic and luminescence properties. *Advanced Materials*, 22(39):4410–4415, 2010.

[18] Ahmad Bayat, Mehdi Shakourian-Fard, Nona Ehyaei, and Mohammad Mahmoodi Hashemi. A magnetic supported iron complex for selective oxidation of sulfides to sulfoxides using 30% hydrogen peroxide at room temperature. *RSC Advances*, 4(83):44274–44281, 2014.

[19] Xiaofeng Su, Brian C Riggs, Minoru Tomozawa, J Keith Nelson, and Douglas B Chrisey. Preparation of $BaTiO_3$/low melting glass core–shell nanoparticles for energy storage capacitor applications. *Journal of Materials Chemistry A*, 2(42):18087–18096, 2014.

[20] Xiaoqing Zhang, Yihua Zhu, Xiaoling Yang, Siwen Wang, Jianhua Shen, Babao Lin, and Chunzhong Li. Enhanced visible light photocatalytic activity of interlayer-isolated triplex ag@ SiO_2@ TiO_2 core–shell nanoparticles. *Nanoscale*, 5(8):3359–3366, 2013.

[21] Elmira FarrokhTakin, Gianni Ciofani, Mauro Gemmi, Vincenzo Piazza, Barbara Mazzolai, and Virgilio Mattoli. Synthesis and characterization of new barium titanate core–gold shell nanoparticles. *Colloids and Surfaces A: Physicochemical and Engineering Aspects*, 415:247–254, 2012.

[22] Armin Kargol, Leszek Malkinski, and Gabriel Caruntu. Biomedical applications of multiferroic nanoparticles. *Edited by Leszek Malkinski*, page 89, 2012.

[23] Rongzheng Liu, Yuzhen Zhao, Rongxia Huang, Yongjie Zhao, and Heping Zhou. Multiferroic ferrite/perovskite oxide core/shell nanostructures. *Journal of Materials Chemistry*, 20(47):10665–10670, 2010.

[24] Kourosh Kalantar-zadeh and Benjamin Fry. *Nanotechnology-enabled sensors*. Springer Science & Business Media, 2007.

[25] Myscope. <http://www.ammrf.org.au/myscope/analysis/eds/xraygeneration/>. 2013.

[26] D Crespo, A Gedanken, Amilcar Labarta Rodríguez, J Llorca, T Pradell, and Ecaterina Valerica Vasilescu. Silver nanostructures: chemical synthesis of colloids and composite nanoparticles, plamon resonance properties and silver nanoparticle monolayer films prepared by spin-coating. 2011.

[27] D Fairhurst and RW Lee. The zeta potential and its use in pharmaceutical applications-part 1: charged interfaces in polar and non-polar media and the concept of zeta potential. *Drug Dev Deliv*, 11:60–4, 2011.

[28] Ichiro Sunagawa. Single crystals grown under unconstrained conditions. In Govindhan Dhanaraj, Kullaiah Byrappa, Vishwanath Prasad, and Michael Dudley, editors, *Springer Handbook of Crystal Growth*, pages 133–157. Springer Berlin Heidelberg, 2010.

[29] Robert M Silverstein, G Clayton Bassler, and TC Morrill. Spectroscopic identification of organic compounds john willey and sons. *New York*, pages 261–264, 1981.

[30] Masih Darbandi, Ralf Thomann, and Thomas Nann. Single quantum dots in silica spheres by microemulsion synthesis. *Chemistry of materials*, 17(23):5720–5725, 2005.

[31] J.H. Adair and E. Suvaci. Submicron electroceramic powder by hydrothermal synthesis. In M.C. Flemings B. Ilschner E.J. Kramer K.H.J. Buschow, R.W. Cahn and S. Mahajanl, editors, *Encyclopedia of Materials: Science and Technology*, page 8933. Elsevier Science Ltd., 2001.

[32] Victor E Borisenko and Stefano Ossicini. *What is what in the Nanoworld: A Handbook on Nanoscience and Nanotechnology*. John Wiley & Sons, 2013.

[33] Mickaël Lallart. *Ferroelectrics-Material Aspects*. InTech, 2011.

[34] BS Rawal, M Kahn, and WR Buessem. Grain core-grain shell structure in barium titanate-based dielectrics. *Advances in ceramics*, 1:172–88, 1981.

[35] Hong-Yang Lu, Jong-Shing Bow, and Wen-How Deng. Core-shell structures in ZrO_2-modified $BaTiO_3$ ceramic. *Journal of the American Ceramic Society*, 73(12):3562–3568, 1990.

[36] Laurel Sheppard. Progress continues in capacitor technology. *American Ceramic Society Bulletin*, 72(3):44–44, 1993.

[37] DE Rase and Rustum Roy. Phase equilibria in the system $BaTiO_3$-SiO_2. *Journal of the American Ceramic Society*, 38(11):389–395, 1955.

[38] Detlev FK Hennings, Rolf Janssen, and Piet JL Reynen. Control of liquid-phase-enhanced discontinuous grain growth in barium titanate. *Journal of the American Ceramic Society*, 70(1):23–27, 1987.

[39] Y Nakano. Microstructure and related phenomena of multilayer ceramic capacitors with ni-electrode. Technical report, DTIC Document, 1993.

[40] Woodrow Wilson Center. http://www.nanotechproject.org/cpi/. 2011.

[41] David Richerson. *Modern ceramic engineering: properties, processing, and use in design*. CRC press, 2005.

[42] Christian Pithan, Detlev Hennings, and Rainer Waser. Progress in the synthesis of nanocrystalline $BaTiO_3$ powders for mlcc. *International Journal of Applied Ceramic Technology*, 2(1):1–14, 2005.

[43] A Beauger, JC Mutin, and JC Niepce. Synthesis reaction of metatitanate $BaTiO_3$. *Journal of materials science*, 18(10):3041–3046, 1983.

[44] Mike SH Chu and Alan WIM Rae. Manufacturing dielectric powders. *American Ceramic Society Bulletin*, 74(6):69–72, 1995.

[45] Matthew H Frey and David A Payne. Synthesis and processing of barium titanate ceramics from alkoxide solutions and monolithic gels. *Chemistry of materials*, 7(1):123–129, 1995.

[46] Hirokazu Shimooka and Makoto Kuwabara. Crystallinity and stoichiometry of nanostructured sol-gel-derived $BaTiO_3$ monolithic gels. *Journal of the American Ceramic Society*, 79(11):2983–2985, 1996.

[47] Burtrand Lee and Jianping Zhang. Preparation, structure evolution and dielectric properties of $BaTiO_3$ thin films and powders by an aqueous sol–gel process. *Thin solid films*, 388(1):107–113, 2001.

[48] R Vivekanandan and TRN Kutty. Characterization of barium titanate fine powders formed from hydrothermal crystallization. *Powder Technology*, 57(3):181–192, 1989.

[49] Chang-Tai Xia, Er-Wei Shi, Wei-Zhuo Zhong, and Jing-Kun Guo. Preparation of $BaTiO_3$ by the hydrothermal method. *Journal of the European Ceramic Society*, 15(12):1171–1176, 1995.

[50] Prabir K Dutta, Reza Asiaie, Sheikh A Akbar, and Weidong Zhu. Hydrothermal synthesis and dielectric properties of tetragonal $BaTiO_3$. *Chemistry of materials*, 6(9):1542–1548, 1994.

[51] Song Wei Lu, Burtrand I Lee, Zhong Lin Wang, and William D Samuels. Hydrothermal synthesis and structural characterization of $BaTiO_3$ nanocrystals. *Journal of Crystal Growth*, 219(3):269–276, 2000.

[52] M Viviani, J Lemaitre, MT Buscaglia, and P Nanni. Low-temperature aqueous synthesis (ltas) of $BaTiO_3$: a statistical design of experiment approach. *Journal of the European Ceramic Society*, 20(3):315–320, 2000.

[53] S Wada, T Tsurumi, H Chikamori, T Noma, and T Suzuki. Preparation of nm-sized $BaTiO_3$ crystallites by a ltds method using a highly concentrated aqueous solution. *Journal of crystal growth*, 229(1):433–439, 2001.

[54] X Wang, BI Lee, MZ Hu, EA Payzant, and DA Blom. Synthesis of nanocrystalline $BaTiO_3$ by solvent refluxing method. *Journal of materials science letters*, 22(7):557–559, 2003.

[55] Andrea R Tao, Krisztian Niesz, and Daniel E Morse. Bio-inspired nanofabrication of barium titanate. *Journal of Materials Chemistry*, 20(37):7916–7923, 2010.

[56] Yoshihiro Hirata and Mitsunori Kawabata. Dispersion and consolidation of ultrafine $BaTiO_3$ powder in non-aqueous solutions. *Materials Letters*, 16(4):175–180, 1993.

[57] D Khastgir and K Adachi. Rheological and dielectric studies of aggregation of barium titanate particles suspended in polydimethylsiloxane. *Polymer*, 41(16):6403–6413, 2000.

[58] Ungyu Paik, Vincent A Hackley, Sung-Churl Choi, and Yeon-Gil Jung. The effect of electrostatic repulsive forces on the stability of $BaTiO_3$ particles suspended in non-aqueous media. *Colloids and Surfaces A: Physicochemical and Engineering Aspects*, 135(1):77–88, 1998.

[59] Lennart Bergstrm, Kazuo Shinozaki, Hiroyuki Tomiyama, and Nobuyasu Mizutani. Colloidal processing of a very fine $BaTiO_3$ powder-effect of particle interactions on the suspension properties, consolidation, and sintering behavior. *Journal of the American Ceramic Society*, 80(2):291–300, 1997.

[60] Wenjea J Tseng and Chun-Liang Lin. Effect of dispersants on rheological behavior of $BaTiO_3$ powders in ethanol–isopropanol mixtures. *Materials chemistry and physics*, 80(1):232–238, 2003.

[61] Carlos Gómez-Yáñez, Heberto Balmori-Ramırez, and Froylán Martınez. Colloidal processing of $BaTiO_3$ using ammonium polyacrylate as dispersant. *Ceramics international*, 26(6):609–616, 2000.

[62] Xinyu Wang, Burtrand I Lee, and Larry Mann. Dispersion of barium titanate with polyaspartic acid in aqueous media. *Colloids and Surfaces A: Physicochemical and Engineering Aspects*, 202(1):71–80, 2002.

[63] Jau-Ho Jean and Hong-Ren Wang. Dispersion of aqueous barium titanate suspensions with ammonium salt of poly (methacrylic acid). *Journal of the American Ceramic Society*, 81(6):1589–1599, 1998.

[64] Wenjea J Tseng and Shiun-Yu Li. Rheology of colloidal $BaTiO_3$ suspension with ammonium polyacrylate as a dispersant. *Materials Science and Engineering: A*, 333(1):314–319, 2002.

[65] Jau-Ho Jean and Hong-Ren Wang. Effects of solids loading, ph, and polyelectrolyte addition on the stabilization of concentrated aqueous $BaTiO_3$ suspensions. *Journal of the American Ceramic Society*, 83(2):277–280, 2000.

[66] Zhi-Gang Shen, Jian-Feng Chen, Hai-kui Zou, and Jimmy Yun. Dispersion of nano-sized aqueous suspensions of barium titanate with ammonium polyacrylate. *Journal of colloid and interface science*, 275(1):158–164, 2004.

[67] S Bhattacharjee, MK Paria, and Himadri Sekhar Maiti. Polyvinyl butyral as a dispersant for barium titanate in a non-aqueous suspension. *Journal of materials science*, 28(23):6490–6495, 1993.

[68] Chia-Wen Chiang and Jau-Ho Jean. Effects of barium dissolution on dispersing aqueous barium titanate suspensions. *Materials chemistry and physics*, 80(3):647–655, 2003.

[69] Dang-Hyok Yoon, Burtrand I Lee, Prerak Badheka, and Xinyu Wang. Barium ion leaching from barium titanate powder in water. *Journal of Materials Science: Materials in Electronics*, 14(3):165–169, 2003.

[70] MC Blanco-Lopez, Brian Rand, and Frank L Riley. The properties of aqueous phase suspensions of barium titanate. *Journal of the European Ceramic Society*, 17(2):281–287, 1997.

[71] AWM De Laat and WPT Derks. Colloidal stabilization of $BaTiO_3$ with poly (vinyl alcohol) in water. *Colloids and Surfaces A: Physicochemical and Engineering Aspects*, 71(2):147–153, 1993.

[72] LS Wang and RY Hong. *Synthesis, surface modification and characterisation of nanoparticles*. INTECH Open Access Publisher, 2011.

[73] Qin Jia Cai, Ye Gan, Mary B Chan-Park, Hong Bin Yang, Zhi Song Lu, Chang Ming Li, Jun Guo, and Zhi Li Dong. Solution-processable barium titanate and strontium titanate nanoparticle dielectrics for low-voltage organic thin-film transistors. *Chemistry of Materials*, 21(14):3153–3161, 2009.

[74] Pengfei Yu, Bin Cui, and Qizhen Shi. Preparation and characterization of $BaTiO_3$ powders and ceramics by sol–gel process using oleic acid as surfactant. *Materials Science and Engineering: A*, 473(1):34–41, 2008.

[75] Ling-xiang Gao, Li Li, Xiao-rong Qi, Wen-xin Wei, Jin-ling Hai, Wei-qing Gao, and Zi-wei Gao. Enhancement on electric responses of $BaTiO_3$ particles with polymer-coating. *Polymer Composites*, 34(6):897–903, 2013.

[76] Werner Stöber, Arthur Fink, and Ernst Bohn. Controlled growth of monodisperse silica spheres in the micron size range. *Journal of colloid and interface science*, 26(1):62–69, 1968.

[77] Lorenz Ratke and Peter W Voorhees. *Growth and coarsening: Ostwald ripening in material processing*. Springer Science & Business Media, 2002.

[78] T Okubo, T Miyamoto, K Umemura, and K Kobayashi. Seed polymerization of tetraethyl orthosilicate in the presence of colloidal silica spheres. *Colloid and Polymer Science*, 279(12):1236–1240, 2001.

[79] Weihong Tan, Kemin Wang, Xiaoxiao He, Xiaojun Julia Zhao, Timothy Drake, Lin Wang, and Rahul P Bagwe. Bionanotechnology based on silica nanoparticles. *Medicinal research reviews*, 24(5):621–638, 2004.

[80] Bidyut K Paul and Satya P Moulik. Uses and applications of microemulsions. *CURRENT SCIENCE-BANGALORE-*, 80(8):990–1001, 2001.

[81] Chia-Lu Chang and H Scott Fogler. Controlled formation of silica particles from tetraethyl orthosilicate in nonionic water-in-oil microemulsions. *Langmuir*, 13(13):3295–3307, 1997.

[82] Chia-Lu Chang and H Scott Fogler. Kinetics of silica particle formation in nonionic w/o microemulsions from teos. *AIChE journal*, 42(11):3153–3163, 1996.

[83] G Gillberg, H Lehtinen, and S Friberg. Nmr and ir investigation of the conditions determining the stability of microemulsions. *Journal of Colloid and Interface Science*, 33(1):40–53, 1970.

[84] TP Hoar and JH Schulman. Transparent water-in-oil dispersions: the oleopathic hydromicelle. *Nature*, 152:102–103, 1943.

[85] Yanling Gao, Anna Elsukova, and Doru C Lupascu. Preparation of SiO_2-encapsulated $BaTiO_3$ nanoparticles with tunable shell thickness by reverse microemulsion. *Particle & Particle Systems Characterization*, 30(10):832–836, 2013.

[86] P Prema. Chemical mediated synthesis of silver nanoparticles and its potential antibacterial application. 2011.

[87] Hairen Tan, Rudi Santbergen, Arno HM Smets, and Miro Zeman. Plasmonic light trapping in thin-film silicon solar cells with improved self-assembled silver nanoparticles. *Nano letters*, 12(8):4070–4076, 2012.

[88] Xi Chen, Baohua Jia, Jhantu K Saha, Boyuan Cai, Nicholas Stokes, Qi Qiao, Yongqian Wang, Zhengrong Shi, and Min Gu. Broadband enhancement in thin-film amorphous silicon solar cells enabled by nucleated silver nanoparticles. *Nano letters*, 12(5):2187–2192, 2012.

[89] Jorge García-Barrasa, José M López-de Luzuriaga, and Miguel Monge. Silver nanoparticles: synthesis through chemical methods in solution and biomedical applications. *Central European Journal of Chemistry*, 9(1):7–19, 2011.

[90] Isabel Pastoriza-Santos and Luis M Liz-Marzán. Colloidal silver nanoplates. state of the art and future challenges. *Journal of Materials Chemistry*, 18(15):1724–1737, 2008.

[91] Pasquale Morvillo, Anna De Girolamo Del Mauro, Giuseppe Nenna, Rosita Diana, Rosa Ricciardi, and Carla Minarini. Ito-free anode with plasmonic silver nanoparticles for high efficient polymer solar cells. *Energy Procedia*, 60:13–22, 2014.

[92] Uwe Kreibig and Michael Vollmer. Optical properties of metal clusters. 1995.

[93] Craig F Bohren and Donald R Huffman. *Absorption and scattering of light by small particles*. John Wiley & Sons, 2008.

[94] Stephan Link and Mostafa A El-Sayed. Optical properties and ultrafast dynamics of metallic nanocrystals. *Annual review of physical chemistry*, 54(1):331–366, 2003.

[95] Yu A Krutyakov, Alexei Aleksandrovich Kudrinskiy, A Yu Olenin, and Georgii Vasilevich Lisichkin. Synthesis and properties of silver nanoparticles: advances and prospects. *Russian Chemical Reviews*, 77(3):233, 2008.

[96] Quang Huy Tran, Anh-Tuan Le, et al. Silver nanoparticles: synthesis, properties, toxicology, applications and perspectives. *Advances in Natural Sciences: Nanoscience and Nanotechnology*, 4(3):033001, 2013.

[97] Lanlan Sun, Yonghai Song, Li Wang, Cunlan Guo, Yujing Sun, Zhelin Liu, and Zhuang Li. Ethanol-induced formation of silver nanoparticle aggregates for highly active sers substrates and application in dna detection. *The Journal of Physical Chemistry C*, 112(5):1415–1422, 2008.

[98] Doowon Seo, Wonjung Yoon, Sangjoon Park, Jihyeon Kim, and Jongsung Kim. The preparation of hydrophobic silver nanoparticles via solvent exchange method. *Colloids and Surfaces A: Physicochemical and Engineering Aspects*, 313:158–161, 2008.

[99] GA Martinez-Castanon, N Nino-Martinez, F Martinez-Gutierrez, JR Martinez-Mendoza, and Facundo Ruiz. Synthesis and antibacterial activity of silver nanoparticles with different sizes. *Journal of Nanoparticle Research*, 10(8):1343–1348, 2008.

[100] Stephan T Dubas and Vimolvan Pimpan. Humic acid assisted synthesis of silver nanoparticles and its application to herbicide detection. *Materials Letters*, 62(17):2661–2663, 2008.

[101] Ming Chen, WenHua Ding, Yang Kong, and GuoWang Diao. Conversion of the surface property of oleic acid stabilized silver nanoparticles from hydrophobic to hydrophilic based on host-guest binding interaction. *Langmuir*, 24(7):3471–3478, 2008.

[102] Hui Wei, Jing Li, Yuling Wang, and Erkang Wang. Silver nanoparticles coated with adenine: preparation, self-assembly and application in surface-enhanced raman scattering. *Nanotechnology*, 18(17):175610, 2007.

[103] Sudhir Kapoor. Preparation, characterization, and surface modification of silver particles. *Langmuir*, 14(5):1021–1025, 1998.

[104] CH Munro, WE Smith, M Garner, JWPC Clarkson, and PC White. Characterization of the surface of a citrate-reduced colloid optimized for use as a substrate for surface-enhanced resonance raman scattering. *Langmuir*, 11(10):3712–3720, 1995.

[105] Helmut Bönnemann and Ryan M Richards. Nanoscopic metal particles- synthetic methods and potential applications. *European Journal of Inorganic Chemistry*, 2001(10):2455–2480, 2001.

[106] Rafique Ullah, Biplob Kumer Deb, and Mohammad Yousuf Ali Mollah. Synthesis and characterization of silica coated iron-oxide composites of different ratios. 2014.

[107] Changzi Jin, Yanjie Wang, Haisheng Wei, Hailian Tang, Xin Liu, Ting Lu, and Junhu Wang. Magnetic iron oxide nanoparticles coated by hierarchically structural silica: highly stable nanocomposite system and ideal catalyst supports. *Journal of Materials Chemistry A*, 2014.

[108] Farzad Zamani and Elham Izadi. Polyvinyl amine coated Fe_3O_4@SiO_2 magnetic microspheres for knoevenagel condensation. *Chinese Journal of Catalysis*, 35(1):21 – 27, 2014.

[109] Jae Sung Park and Young Ho Han. Nano size $BaTiO_3$ powder coated with silica. *Ceramics international*, 31(6):777–782, 2005.

[110] RenZheng Chen, AiLi Cui, XiaoHui Wang, ZhiLun Gui, and LongTu Li. Structure, sintering behavior and dielectric properties of silica-coated $BaTiO_3$. *Materials Letters*, 54(4):314–317, 2002.

[111] Marie-Christine Daniel and Didier Astruc. Gold nanoparticles: assembly, supramolecular chemistry, quantum-size-related properties, and applications toward biology, catalysis, and nanotechnology. *Chemical reviews*, 104(1):293–346, 2004.

[112] J van den Boomgaard, AMJG Van Run, and J Van Suchtelen. Piezoelectric-piezomagnetic composites with magnetoelectric effect. *Ferroelectrics*, 14(1):727–728, 1976.

[113] Jungho Ryu, Shashank Priya, Kenji Uchino, and Hyoun-Ee Kim. Magnetoelectric effect in composites of magnetostrictive and piezoelectric materials. *Journal of Electroceramics*, 8(2):107–119, 2002.

[114] Maria Teresa Buscaglia, Vincenzo Buscaglia, Lavinia Curecheriu, Petronel Postolache, Liliana Mitoseriu, Adelina C Ianculescu, Bogdan S Vasile, Zhao Zhe, and Paolo Nanni. Fe_2O_3@$BaTiO_3$ core- shell particles as reactive precursors for the preparation of multifunctional composites containing different magnetic phases. *Chemistry of Materials*, 22(16):4740–4748, 2010.

[115] Lavinia P Curecheriu, Maria T Buscaglia, Vincenzo Buscaglia, Liliana Mitoseriu, Petronel Postolache, A Ianculescu, and Paolo Nanni. Functional properties of $BaTiO_3$-$Ni_{0.5}Zn_{0.5}Fe_2O_4$ magnetoelectric ceramics prepared from powders with core-shell structure. *Journal of Applied Physics*, 107(10):104106, 2010.

[116] Jens Als-Nielsen and Des McMorrow. *Elements of modern X-ray physics*. John Wiley & Sons, 2011.

[117] Ron Jenkins and Robert Snyder. *Introduction to X-ray powder diffractometry*, volume 267. John Wiley & Sons, 2012.

[118] Lyle H Schwartz. *Diffraction from materials*. Elsevier, 2012.

[119] Joseph I Goldstein, Dale E Newbury, Patrick Echlin, David C Joy, Charles Fiori, Eric Lifshin, et al. *Scanning electron microscopy and X-ray microanalysis. A text for biologists, materials scientists, and geologists*. Plenum Publishing Corporation, 1981.

[120] SJ Pennycook, AR Lupini, M Varela, A Borisevich, Y Peng, MP Oxley, K Van Benthem, and MF Chisholm. Scanning transmission electron microscopy for nanostructure characterization. In *Scanning Microscopy for Nanotechnology*, pages 152–191. Springer, 2007.

[121] Paul D Brown. Transmission electron microscopy-a textbook for materials science, 1999.

[122] Brent Fultz and James Howe. *Transmission electron microscopy and diffractometry of materials*. Springer, 2012.

[123] David B Williams and C Barry Carter. *The Transmission Electron Microscope*. Springer, 1996.

[124] Challa SSR Kumar. *UV-VIS and Photoluminescence Spectroscopy for Nanomaterials Characterization*. Springer, 2013.

[125] John R Ferraro. *Practical Fourier transform infrared spectroscopy: industrial and laboratory chemical analysis*. Elsevier, 2012.

[126] Robert J Hunter. *Zeta potential in colloid science: principles and applications*. Academic press, 2013.

[127] Particle Metrix Particle Metrix GmbH. <http://www.particle-metrix.de/en/home.html>. 2014.

[128] D Yoon. Tetragonality of barium titanate powder for a ceramic capacitor application. *Journal of Ceramic Processing Research*, 7(4):343, 2006.

[129] Hiroshi Kishi, Youichi Mizuno, and Hirokazu Chazono. Base-metal electrode-multilayer ceramic capacitors: past, present and future perspectives. *Japanese journal of applied physics*, 42(1R):1, 2003.

[130] Detlev FK Hennings, B Seriyati Schreinemacher, and Herbert Schreinemacher. Solid-state preparation of $BaTiO_3$-based dielectrics, using ultrafine raw materials. *Journal of the American Ceramic Society*, 84(12):2777–2782, 2001.

[131] R Allen Kimel, Vladimir Ganine, and James H Adair. Double injection synthesis and dispersion of submicrometer barium titanyl oxalate tetrahydrate. *Journal of the American Ceramic Society*, 84(5):1172–1174, 2001.

[132] Byoung-Kyu Kim, Dae-Young Lim, Richard E Riman, Jun-Seok Nho, and Seung-Beom Cho. A new glycothermal process for barium titanate nanoparticle synthesis. *Journal of the American Ceramic Society*, 86(10):1793–1796, 2003.

[133] Hidehiro Kamiya, Kenjiro Gomi, Yuichi Iida, Kenji Tanaka, Takashi Yoshiyasu, and Toshihito Kakiuchi. Preparation of highly dispersed ultrafine barium titanate powder by using microbial-derived surfactant. *Journal of the American Ceramic Society*, 86(12):2011–2018, 2003.

[134] Paola Gherardi and Egon Matijević. Homogeneous precipitation of spherical colloidal barium titanate particles. *Colloids and surfaces*, 32:257–274, 1988.

[135] Christopher W Beier, Marie A Cuevas, and Richard L Brutchey. Room-temperature synthetic pathways to barium titanate nanocrystals. *Small*, 4(12):2102–2106, 2008.

[136] Gul Ahmad, Matthew B Dickerson, Ye Cai, Sharon E Jones, Eric M Ernst, Jonathan P Vernon, Michael S Haluska, Yunnan Fang, Jiadong Wang, Guru Subramanyam, et al. Rapid bioenabled formation of ferroelectric $BaTiO_3$ at room temperature from an aqueous salt solution at near neutral ph. *Journal of the American Chemical Society*, 130(1):4–5, 2008.

[137] Federico A Rabuffetti, John S Lee, and Richard L Brutchey. Low temperature synthesis of complex $Ba_{1-x}Sr_xTi_{1-y}Zr_yO_3$ perovskite nanocrystals. *Chemistry of Materials*, 24(16):3114–3116, 2012.

[138] Christopher W Beier, Marie A Cuevas, and Richard L Brutchey. Low-temperature synthesis of solid-solution $Ba_xSr_{1-x}Ti_3$ nanocrystals. *J. Mater. Chem.*, 20(24):5074–5079, 2010.

[139] PP Phule and SH Risbud. Low temperature synthesis and dielectric properties of ceramics derived from amorphous barium titanate gels and crystalline powders. *Materials Science and Engineering: B*, 3(3):241–247, 1989.

[140] Toshinobu Yoko, Kanichi Kamiya, and Katsuhisa Tanaka. Preparation of multiple oxide $BaTiO_3$ fibres by the sol-gel method. *Journal of Materials Science*, 25(9):3922–3929, 1990.

[141] Un-Yeon Hwang, Hyung-Sang Park, and Kee-Kahb Koo. Behavior of barium acetate and titanium isopropoxide during the formation of crystalline barium titanate. *Industrial & engineering chemistry research*, 43(3):728–734, 2004.

[142] Guang J Choi, Sang K Lee, Kyoung J Woo, Kee K Koo, and Young S Cho. Characteristics of $BaTiO_3$ particles prepared by spray-coprecipitation method using titanium acylate-based precursors. *Chemistry of materials*, 10(12):4104–4113, 1998.

[143] P Davide Cozzoli, Andreas Kornowski, and Horst Weller. Low-temperature synthesis of soluble and processable organic-capped anatase tio2 nanorods. *Journal of the American Chemical Society*, 125(47):14539–14548, 2003.

[144] Timothy J Boyle, Ryan P Tyner, Todd M Alam, Brian L Scott, Joseph W Ziller, and BG Potter. Implications for the thin-film densification of tio2 from carboxylic acid-modified titanium alkoxides. syntheses, characterizations, x-ray structures of ti3 (μ3-o)(o2ch) 2 (onep) 8, ti3 (μ3-o)(o2cme) 2 (onep) 8, ti6 (μ3-o) 6 (o2cchme2) 6 (onep) 6,[ti (μ-o2ccme3)(onep) 3] 2, and ti3 (μ3-o)(o2cch2cme3) 2 (onep) 8 (onep= och2cme3) 1. *Journal of the American Chemical Society*, 121(51):12104–12112, 1999.

[145] Kazuo Nakamoto. *Infrared and Raman spectra of inorganic and coordination compounds*. Wiley Online Library, 1978.

[146] Zhihua Zhang, Xinhua Zhong, Shuhua Liu, Dongfei Li, and Mingyong Han. Aminolysis route to monodisperse titania nanorods with tunable aspect ratio. *Angewandte Chemie*, 117(22):3532–3536, 2005.

[147] S Doeuff, M Henry, C Sanchez, and J Livage. Hydrolysis of titanium alkoxides: modification of the molecular precursor by acetic acid. *Journal of Non-crystalline solids*, 89(1):206–216, 1987.

[148] PJ Thistlethwaite and MS Hook. Diffuse reflectance fourier transform infrared study of the adsorption of oleate/oleic acid onto titania. *Langmuir*, 16(11):4993–4998, 2000.

[149] GB Deacon and RJ Phillips. Relationships between the carbon-oxygen stretching frequencies of carboxylato complexes and the type of carboxylate coordination. *Coordination Chemistry Reviews*, 33(3):227–250, 1980.

[150] Alexander I Yanovsky, Mary I Yanovskaya, Victoriya K Limar, Vadim G Kessler, Nataliya Ya Turova, and Yuri T Struchkov. Synthesis and crystal structure of the double barium–titanium isopropoxide [ba4ti4 (μ4-o) 4 (μ3-or) 2 (μ-or) 8 (or) 6 (roh) 4][ba4ti4 (μ4-o) 4 (μ3-or) 2 (μ-or) 9 (or) 5 (roh) 3]. *J. Chem. Soc., Chem. Commun.*, (22):1605–1606, 1991.

[151] JI t Langford and AJC Wilson. Scherrer after sixty years: a survey and some new results in the determination of crystallite size. *Journal of Applied Crystallography*, 11(2):102–113, 1978.

[152] MH Frey and DA Payne. Grain-size effect on structure and phase transformations for barium titanate. *Physical Review B*, 54(5):3158, 1996.

[153] J Sheng, U Welzel, and EJ Mittemeijer. Nonmonotonic crystallite-size dependence of the lattice parameter of nanocrystalline nickel. *Applied Physics Letters*, 97(15):153109, 2010.

[154] Zaixing Huang, Peter Thomson, and Shenglin Di. Lattice contractions of a nanoparticle due to the surface tension: A model of elasticity. *Journal of Physics and Chemistry of Solids*, 68(4):530–535, 2007.

[155] Guido Busca, Vincenzo Buscaglia, Marcello Leoni, and Paolo Nanni. Solid-state and surface spectroscopic characterization of $BaTiO_3$ fine powders. *Chemistry of materials*, 6(7):955–961, 1994.

[156] I Laulicht and L Benguigui. Infrared spectra of hydrogen impurities in $BaTiO_3$ crystals. *Solid State Communications*, 32(9):771–775, 1979.

[157] S Kapphan and G Weber. Ir-absorption study of h and d-impurities in $BaTiO_3$ crystals. *Ferroelectrics*, 37(1):673–676, 1981.

[158] Uma D Venkateswaran, Vaman M Naik, and Ratna Naik. High-pressure raman studies of polycrystalline $BaTiO_3$. *Physical Review B*, 58(21):14256, 1998.

[159] Yury V Kolen'ko, Kirill A Kovnir, Inés S Neira, Takaaki Taniguchi, Tadashi Ishigaki, Tomoaki Watanabe, Naonori Sakamoto, and Masahiro Yoshimura. A novel, controlled, and high-yield solvothermal drying route to nanosized barium titanate powders. *The Journal of Physical Chemistry C*, 111(20):7306–7318, 2007.

[160] C Pithan, Y Shiratori, R Waser, J Dornseiffer, and F-H Haegel. Preparation, processing, and characterization of nano-crystalline $BaTiO_3$ powders and ceramics derived from microemulsion-mediated synthesis. *Journal of the American Ceramic Society*, 89(9):2908–2916, 2006.

[161] Detlev FK Hennings, Christoph Metzmacher, and B Seriyati Schreinemacher. Defect chemistry and microstructure of hydrothermal barium titanate. *Journal of the American Ceramic Society*, 84(1):179–182, 2001.

[162] GA Barbosa, A Chaves, and SPS Porto. Temperature dependence of the raman cross sections in $BaTiO_3$ and $SrTiO_3$. *Solid State Communications*, 11(8):1053–1055, 1972.

[163] Guan-Qun Xie, Meng-Fei Luo, Mai He, Ping Fang, Jing-Meng Ma, Yue-Fang Ying, and Zong-Lan Yan. An improved method for preparation of $Ce_{0.8}Pr_{0.2}$TOY solid solutions

with nanoparticles smaller than 10 nm. *Journal of Nanoparticle Research*, 9(3):471–478, 2007.

[164] Limiao Chen, Xiaoming Sun, Younian Liu, and Yadong Li. Preparation and characterization of porous MgO and NiO/MgO nanocomposites. *Applied Catalysis A: General*, 265(1):123–128, 2004.

[165] Luís F Da Silva, Lauro June Queiroz Maia, Maria Inês B Bernardi, JA Andres, and Valmor R Mastelaro. An improved method for preparation of $SrTiO_3$ nanoparticles. *Materials Chemistry and Physics*, 125(1):168–173, 2011.

[166] Seung-Beom Cho, Jun-Seok Noh, Dae-Young Lim, Seok-Hyoung Hong, and Richard E Riman. Low-temperature solution route to $BaTiO_3$ thin films on titanium metal substrate. *Materials Letters*, 57(26):4302–4308, 2003.

[167] Bi-Jun Fang, Hai-Qing Xu, Tian-Hou He, Hao-Su Luo, and Zhi-Wen Yin. Growth mechanism and electrical properties of $Pb[(Zn_{1/3}Nb_{2/3})_{0.91}Ti_{0.09}]O_3$ single crystals by a modified bridgman method. *Journal of crystal growth*, 244:318–326, 2002.

[168] Hongjun Zhou, Yuanbing Mao, and Stanislaus S Wong. Shape control and spectroscopy of crystalline $BaZrO_3$ perovskite particles. *Journal of Materials Chemistry*, 17(17):1707–1713, 2007.

[169] S-M Lee, S-N Cho, and Jinwoo Cheon. Anisotropic shape control of colloidal inorganic nanocrystals. *Advanced Materials*, 15(5):441–444, 2003.

[170] MohanD. Aggarwal, AshokK. Batra, RavindraB. Lal, BenjaminG. Penn, and DonaldO. Frazier. Bulk single crystals grown from solution on earth and in microgravity. In Govindhan Dhanaraj, Kullaiah Byrappa, Vishwanath Prasad, and Michael Dudley, editors, *Springer Handbook of Crystal Growth*, pages 559–598. Springer Berlin Heidelberg, 2010.

[171] Cheng-Yan Xu, Qi Zhang, Han Zhang, Liang Zhen, Jie Tang, and Lu-Chang Qin. Synthesis and characterization of single-crystalline alkali titanate nanowires. *Journal of the American Chemical Society*, 127(33):11584–11585, 2005.

[172] Per Martin Rørvik, Tone Lyngdal, Ragnhild Sæterli, Antonius TJ van Helvoort, Randi Holmestad, Tor Grande, and Mari-Ann Einarsrud. Influence of volatile chlorides on the molten salt synthesis of ternary oxide nanorods and nanoparticles. *Inorganic chemistry*, 47(8):3173–3181, 2008.

[173] Jun Xu, Jianfeng Xia, and Zhiqun Lin. Evaporation-induced self-assembly of nanoparticles from a sphere-on-flat geometry. *Angewandte Chemie*, 119(11):1892–1895, 2007.

[174] Achim Neubrand, Reinhard Lindner, and Peter Hoffmann. Room-temperature solubility behavior of barium titanate in aqueous media. *Journal of the American Ceramic Society*, 83(4):860–864, 2000.

[175] Kikuo Wakino, Tsutomu Okada, Norio Yoshida, and Kunisaburo Tomono. A new equation for predicting the dielectric constant of a mixture. *Journal of the American Ceramic Society*, 76(10):2588–2594, 1993.

[176] Satoshi Wada, Hiroaki Yasuno, Takuya Hoshina, Song-Min Nam, Hirofumi Kakemoto, and Takaaki Tsurumi. Preparation of nm-sized barium titanate fine particles and their powder dielectric properties. *Japanese journal of applied physics*, 42(9S):6188, 2003.

[177] Chen Zou, John C Fothergill, and Stephen W Rowe. The effect of water absorption on the dielectric properties of epoxy nanocomposites. *Dielectrics and Electrical Insulation, IEEE Transactions on*, 15(1):106–117, 2008.

[178] Ion Bunget and Mihai Popescu. *Physics of Solid Dielectrics*. Elsevier, 1984.

[179] J. C. Maxwell Garnett. Colours in metal glasses and in metallic films. *Philosophical Transactions of the Royal Society of London. Series A, Containing Papers of a Mathematical or Physical Character*, 203(359-371):385–420, 1904.

[180] Von DAG Bruggeman. Berechnung verschiedener physikalischer konstanten von heterogenen substanzen. i. dielektrizitätskonstanten und leitfähigkeiten der mischkörper aus isotropen substanzen. *Annalen der physik*, 416(7):636–664, 1935.

[181] Philseok Kim, Natalie M Doss, John P Tillotson, Peter J Hotchkiss, Ming-Jen Pan, Seth R Marder, Jiangyu Li, Jeffery P Calame, and Joseph W Perry. High energy density nanocomposites based on surface-modified $BaTiO_3$ and a ferroelectric polymer. *ACS nano*, 3(9):2581–2592, 2009.

[182] Zhong Li, Lisa A Fredin, Pratyush Tewari, Sara A DiBenedetto, Michael T Lanagan, Mark A Ratner, and Tobin J Marks. In situ catalytic encapsulation of core-shell nanoparticles having variable shell thickness: dielectric and energy storage properties of high-permittivity metal oxide nanocomposites. *Chemistry of Materials*, 22(18):5154–5164, 2010.

[183] Kwi-Il Park, Minbaek Lee, Ying Liu, San Moon, Geon-Tae Hwang, Guang Zhu, Ji Eun Kim, Sang Ouk Kim, Do Kyung Kim, Zhong Lin Wang, et al. Flexible nanocomposite generator made of $BaTiO_3$ nanoparticles and graphitic carbons. *Advanced Materials*, 24(22):2999–3004, 2012.

[184] VV Shvartsman, F Alawneh, P Borisov, D Kozodaev, and DC Lupascu. Converse magnetoelectric effect in $CoFe_2O_4$–$BaTiO_3$ composites with a core–shell structure. *Smart Materials and Structures*, 20(7):075006, 2011.

[185] Haimei Fan, Haiyan Li, Bingkun Liu, Yongchun Lu, Tengfeng Xie, and Dejun Wang. Photoinduced charge transfer properties and photocatalytic activity in Bi_2O_3/$BaTiO_3$ composite photocatalyst. *ACS applied materials & interfaces*, 4(9):4853–4857, 2012.

[186] Satoshi Wada, Takeyuki Suzuki, and Tatsuo Noma. Preparation of barium titanate fine particles by hydrothermal method and their characterization. *Nippon seramikkusu kyokai gakujutsu ronbunshi*, 103(12):1220–1227, 1995.

[187] D Völtzke, S Gablenz, H-P Abicht, R Schneider, E Pippel, and J Woltersdorf. Surface modification of barium titanate powder particles. *Materials chemistry and physics*, 61(2):110–116, 1999.

[188] Christopher W Beier, Marie A Cuevas, and Richard L Brutchey. Effect of surface modification on the dielectric properties of $BaTiO_3$ nanocrystals. *Langmuir*, 26(7):5067–5071, 2009.

[189] Wei-Heng Shih, David Kisailus, and Yen Wei. Silica coating on barium titanate particles. *Materials Letters*, 24(1):13–15, 1995.

[190] Christophe Huber, Catherine Elissalde, Virginie Hornebecq, Stéphane Mornet, Mona Treguer-Delapierre, François Weill, and Mario Maglione. Nano-ferroelectric based core–shell particles: towards tuning of dielectric properties. *Ceramics international*, 30(7):1241–1245, 2004.

[191] Hideki Matsumoto, Daisuke Nagao, Yoshio Kobayashi, and Mikio Konno. Silica-coating of barium titanate particles. *Characterization and Control of Interfaces for High Quality Advanced Materials II: Ceramic Transactions, Volume 198*, pages 57–61, 2007.

[192] Rajib Ghosh Chaudhuri and Santanu Paria. Core/shell nanoparticles: classes, properties, synthesis mechanisms, characterization, and applications. *Chemical reviews*, 112(4):2373–2433, 2011.

[193] Mei Fang, Tarja T Volotinen, SK Kulkarni, Lyubov Belova, and K Venkat Rao. Effect of embedding Fe_2O_3 nanoparticles in silica spheres on the optical transmission properties of three-dimensional magnetic photonic crystals. *Journal of Applied Physics*, 108(10):103501, 2010.

[194] I Ponomareva, I Naumov, I Kornev, Huaxiang Fu, and L Bellaiche. Modelling of nanoscale ferroelectrics from atomistic simulations. *Current Opinion in Solid State and Materials Science*, 9(3):114–121, 2005.

[195] EV Charnaya, AL Pirozerskii, Cheng Tien, and MK Lee. Ferroelectricity in an array of electrically coupled confined small particles. *Ferroelectrics*, 350(1):75–80, 2007.

[196] U Chung, Catherine Elissalde, Frédéric Mompiou, Jérôme Majimel, Sonia Gomez, Claude Estournès, Sylvain Marinel, Andreas Klein, François Weill, Dominique Michau, et al. Interface investigation in nanostructured $BaTiO_3$/silica composite ceramics. *Journal of the American Ceramic Society*, 93(3):865–874, 2010.

[197] Dmitry Nuzhnyy, Jan Petzelt, Viktor Bovtun, Martin Kempa, Maxim Savinov, Catherine Elissalde, U-C Chung, Dominique Michau, Claude Estournès, and Mario Maglione. High-frequency dielectric spectroscopy of $BaTiO_3$ core-silica shell nanocomposites: Problem of interdiffusion. *Journal of Advanced Dielectrics*, 1(03):309–317, 2011.

[198] Thomas D Schladt, Kerstin Koll, Steve Prüfer, Heiko Bauer, Filipe Natalio, Oliver Dumele, Renugan Raidoo, Stefan Weber, Uwe Wolfrum, Laura M Schreiber, et al. Multifunctional superparamagnetic $MnO@SiO_2$ core-shell nanoparticles and their application for optical and magnetic resonance imaging. *Journal of Materials Chemistry*, 22(18):9253–9262, 2012.

[199] Yuri A Barnakov, Minghui H Yu, and Zeev Rosenzweig. Manipulation of the magnetic properties of magnetite-silica nanocomposite materials by controlled stober synthesis. *Langmuir*, 21(16):7524–7527, 2005.

[200] Yu Lu, Yadong Yin, Brian T Mayers, and Younan Xia. Modifying the surface properties of superparamagnetic iron oxide nanoparticles through a sol-gel approach. *Nano letters*, 2(3):183–186, 2002.

[201] Rolf Koole, Matti M van Schooneveld, Jan Hilhorst, Celso de Mello Donegá, Dannis C Hart, Alfons van Blaaderen, Daniel Vanmaekelbergh, and Andries Meijerink. On the incorporation mechanism of hydrophobic quantum dots in silica spheres by a reverse microemulsion method. *Chemistry of Materials*, 20(7):2503–2512, 2008.

[202] I Abarkan, T Doussineau, and M Smaihi. Tailored macro/microstructural properties of colloidal silica nanoparticles via microemulsion preparation. *Polyhedron*, 25(8):1763–1770, 2006.

[203] Swadeshmukul Santra, Rovelyn Tapec, Nikoleta Theodoropoulou, Jon Dobson, Arthur Hebard, and Weihong Tan. Synthesis and characterization of silica-coated iron oxide nanoparticles in microemulsion: the effect of nonionic surfactants. *Langmuir*, 17(10):2900–2906, 2001.

[204] Andrés Guerrero-Martínez, Jorge Pérez-Juste, and Luis M Liz-Marzán. Recent progress on silica coating of nanoparticles and related nanomaterials. *Advanced Materials*, 22(11):1182–1195, 2010.

[205] Mandar M Shirolkar, Raja Das, Tuhin Maity, Pankaj Poddar, and Sulabha K Kulkarni. Observation of enhanced dielectric coupling and room-temperature ferromagnetism in chemically synthesized bifeo3@ sio2 core–shell particles. *The Journal of Physical Chemistry C*, 116(36):19503–19511, 2012.

[206] Stéphane Mornet, Catherine Elissalde, Virginie Hornebecq, Olivier Bidault, Etienne Duguet, Alain Brisson, and Mario Maglione. Controlled growth of silica shell on $Ba_{0.6}Sr_{0.4}TiO_3$ nanoparticles used as precursors of ferroelectric composites. *Chemistry of materials*, 17(17):4530–4536, 2005.

[207] Xingmei Guo, Xuguang Liu, Bingshe Xu, and Tao Dou. Synthesis and characterization of carbon sphere-silica core–shell structure and hollow silica spheres. *Colloids and Surfaces A: Physicochemical and Engineering Aspects*, 345(1):141–146, 2009.

[208] Shufen Wang, Hongming Cao, Feng Gu, Chunzhong Li, and Guangjian Huang. Synthesis and magnetic properties of iron/silica core/shell nanostructures. *Journal of Alloys and Compounds*, 457(1):560–564, 2008.

[209] Xiaoxiao Yu, Shengwei Liu, and Jiaguo Yu. Superparamagnetic γ-Fe_2O_3@SiO_2@TiO_2 composite microspheres with superior photocatalytic properties. *Applied Catalysis B: Environmental*, 104(1):12–20, 2011.

[210] Jian Xu and Carole C Perry. A novel approach to Au@SiO_2 core-shell spheres. *Journal of Non-Crystalline Solids*, 353(11):1212–1215, 2007.

[211] Andrea Schroedter, Horst Weller, Ramon Eritja, William E Ford, and Jurina M Wessels. Biofunctionalization of silica-coated cdte and gold nanocrystals. *Nano Letters*, 2(12):1363–1367, 2002.

[212] Yoshio Kobayashi, Hironori Katakami, Eiichi Mine, Daisuke Nagao, Mikio Konno, and Luis M Liz-Marzán. Silica coating of silver nanoparticles using a modified stöber method. *Journal of colloid and interface science*, 283(2):392–396, 2005.

[213] Carmen Vogt, Muhammet S Toprak, Mamoun Muhammed, Sophie Laurent, Jean-Luc Bridot, and Robert N Müller. High quality and tuneable silica shell–magnetic core nanoparticles. *Journal of nanoparticle research*, 12(4):1137–1147, 2010.

[214] XF Zhang, S Mansouri, L Clime, HQ Ly, L'H Yahia, and T Veres. Fe_3O_4–silica core–shell nanoporous particles for high-capacity ph-triggered drug delivery. *Journal of Materials Chemistry*, 22(29):14450–14457, 2012.

[215] Yanling Gao, Vladimir V Shvartsman, Anna Elsukova, and Doru C Lupascu. Low-temperature synthesis of crystalline $BaTiO_3$ nanoparticles by one-step "organosol"-precipitation. *Journal of Materials Chemistry*, 22(34):17573–17583, 2012.

[216] Johannes Lyklema. *Fundamentals of interface and colloid science: soft colloids*, volume 5. Academic press, 2005.

[217] Mauricio Escudey, Maria de la Luz Mora, Patricia Diaz, and Gerardo Galindo. Apparent dissolution during ultrasonic dispersion of allophanic soils and soil fractions. *Clays and Clay Minerals*, 37(5):493–496, 1989.

[218] Vladimir M. Gunko and Roman leboda. Carbon-silica adsorbents. In P. Somasundaran, editor, *Encyclopedia of Surface and Colloid Science, Second Edition - Eight-Volume Set (Print)*, pages 1120–1134. Taylor & Francis, 2006.

[219] George A Parks. The isoelectric points of solid oxides, solid hydroxides, and aqueous hydroxo complex systems. *Chemical Reviews*, 65(2):177–198, 1965.

[220] Maria Vamvakaki, Norman C Billingham, Steven P Armes, John F Watts, and Stephen J Greaves. Controlled structure copolymers for the dispersion of high-performance ceramics in aqueous media. *Journal of Materials Chemistry*, 11(10):2437–2444, 2001.

[221] Dong Kee Yi, Su Seong Lee, Georgia C Papaefthymiou, and Jackie Y Ying. Nanoparticle architectures templated by SiO_2/Fe_2O_3 nanocomposites. *Chemistry of Materials*, 18(3):614–619, 2006.

[222] S Pillai and MA Green. Plasmonics for photovoltaic applications. *Solar Energy Materials and Solar Cells*, 94(9):1481–1486, 2010.

[223] KR Catchpole and Albert Polman. Plasmonic solar cells. *Optics express*, 16(26):21793–21800, 2008.

[224] S Pillai, KR Catchpole, T Trupke, and MA Green. Surface plasmon enhanced silicon solar cells. *Journal of applied physics*, 101(9):093105, 2007.

[225] DM Schaadt, B Feng, and ET Yu. Enhanced semiconductor optical absorption via surface plasmon excitation in metal nanoparticles. *Applied Physics Letters*, 86(6):063106, 2005.

[226] Gustav Mie. Beiträge zur optik trüber medien, speziell kolloidaler metallösungen. *Annalen der physik*, 330(3):377–445, 1908.

[227] Alan S Edelstein and RC Cammaratra. *Nanomaterials: synthesis, properties and applications*. CRC Press, 1998.

[228] Vincenzo Amendola, Osman M Bakr, and Francesco Stellacci. A study of the surface plasmon resonance of silver nanoparticles by the discrete dipole approximation method: effect of shape, size, structure, and assembly. *Plasmonics*, 5(1):85–97, 2010.

[229] SJ Oldenburg, RD Averitt, SL Westcott, and NJ Halas. Nanoengineering of optical resonances. *Chemical Physics Letters*, 288(2):243–247, 1998.

[230] E Prodan, C Radloff, NJ Halas, and P Nordlander. A hybridization model for the plasmon response of complex nanostructures. *Science*, 302(5644):419–422, 2003.

[231] Peter Nordlander, C Oubre, E Prodan, K Li, and MI Stockman. Plasmon hybridization in nanoparticle dimers. *Nano Letters*, 4(5):899–903, 2004.

[232] E Prodan and PJCP Nordlander. Plasmon hybridization in spherical nanoparticles. *The Journal of chemical physics*, 120(11):5444–5454, 2004.

[233] Katri Laaksonen, Samu Suomela, Sakari R Puisto, Niko KJ Rostedt, Tapio Ala-Nissila, and Risto M Nieminen. Influence of high-refractive-index oxide coating on optical properties of metal nanoparticles. *JOSA B*, 30(2):338–348, 2013.

[234] Seung Ho Choi, You Na Ko, Jung-Kul Lee, Byung Kyu Park, and Yun Chan Kang. Core-shell-structure Ag-$BaTiO_3$ composite nanopowders prepared directly by flame spray pyrolysis. *Materials Chemistry and Physics*, 140(1):266–272, 2013.

[235] N Kalfagiannis, PG Karagiannidis, C Pitsalidis, NT Panagiotopoulos, C Gravalidis, S Kassavetis, P Patsalas, and S Logothetidis. Plasmonic silver nanoparticles for improved organic solar cells. *Solar Energy Materials and Solar Cells*, 104:165–174, 2012.

[236] Jinxia Xu, Xiangheng Xiao, Andrey L Stepanov, Fen Ren, Wei Wu, Guangxu Cai, Shaofeng Zhang, Zhigao Dai, Fei Mei, and Changzhong Jiang. Efficiency enhancements in Ag nanoparticles-SiO_2-TiO_2 sandwiched structure via plasmonic effect-enhanced light capturing. *Nanoscale research letters*, 8(1):1–5, 2013.

[237] Wenfei Shen, Jianguo Tang, Renqiang Yang, Hailin Cong, Xichang Bao, Yao Wang, Xinzhi Wang, Zhen Huang, Jixian Liu, Linjun Huang, et al. Enhanced efficiency of polymer solar cells by incorporated Ag-SiO_2 core-shell nanoparticles in the active layer. *RSC Advances*, 4(9):4379–4386, 2014.

[238] Wei EI Sha, Wallace CH Choy, Yongpin P Chen, and Weng Cho Chew. Optical design of organic solar cell with hybrid plasmonic system. *Optics express*, 19(17):15908–15918, 2011.

[239] Antonio Rogério Fiorucci, Luciana Maria Saran, Éder Tadeu Gomes Cavalheiro, and Eduardo Almeida Neves. Thermal stability and bonding in the silver complexes of ethylenediaminetetraacetic acid. *Thermochimica acta*, 356(1):71–78, 2000.

[240] Donald Pavia, Gary Lampman, George Kriz, and James Vyvyan. *Introduction to spectroscopy*. Cengage Learning, 2008.

[241] Hideki Sakai, Takashi Kanda, Hirobumi Shibata, Takahiro Ohkubo, and Masahiko Abe. Preparation of highly dispersed core/shell-type titania nanocapsules containing a single ag nanoparticle. *Journal of the American Chemical Society*, 128(15):4944–4945, 2006.

[242] Renjis T Tom, A Sreekumaran Nair, Navinder Singh, M Aslam, CL Nagendra, Reji Philip, K Vijayamohanan, and T Pradeep. Freely dispersible Au@TiO_2, Au@ZrO_2, Ag@TiO_2, and Ag@ZrO_2 core-shell nanoparticles: One-step synthesis, characterization, spectroscopy, and optical limiting properties. *Langmuir*, 19(8):3439–3445, 2003.

[243] Shigeki Yamamoto, Kazuhiko Fujiwara, and Hitoshi Watarai. Surface-enhanced raman scattering from oleate-stabilized silver colloids at a liquid/liquid interface. *interfaces*, 13:14, 2004.

[244] H Hövel, S Fritz, A Hilger, U Kreibig, and M Vollmer. Width of cluster plasmon resonances: bulk dielectric functions and chemical interface damping. *Physical Review B*, 48(24):18178, 1993.

[245] Arthur L Aden and Milton Kerker. Scattering of electromagnetic waves from two concentric spheres. *Journal of Applied Physics*, 22(10):1242–1246, 1951.

[246] Daniel J Ross and Reinhard Sigel. Mie scattering by soft core-shell particles and its applications to ellipsometric light scattering. *Physical Review E*, 85(5):056710, 2012.

[247] Sujit Kumar Ghosh and Tarasankar Pal. Interparticle coupling effect on the surface plasmon resonance of gold nanoparticles: from theory to applications. *Chemical Reviews*, 107(11):4797–4862, 2007.

[248] K-H Su, Q-H Wei, X Zhang, JJ Mock, David R Smith, and S Schultz. Interparticle coupling effects on plasmon resonances of nanogold particles. *Nano Letters*, 3(8):1087–1090, 2003.

[249] Stuart O Nelson. Density-permittivity relationships for powdered and granular materials. *Instrumentation and Measurement, IEEE Transactions on*, 54(5):2033–2040, 2005.

[250] Shaobo Yang, Tengfei Wu, Xinhua Zhao, Xingfei Li, and Wenbin Tan. The optical property of core-shell nanosensors and detection of atrazine based on localized surface plasmon resonance (lspr) sensing. *Sensors*, 14(7):13273–13284, 2014.

[251] Mojtaba Rahimabady, Li Lu, and Kui Yao. Nanocomposite multilayer capacitors comprising $BaTiO_3$@TiO_2 and poly (vinylidene fluoride-hexafluoropropylene) for dielectric-based energy storage. *Journal of Advanced Dielectrics*, 4(02), 2014.

[252] Suibin Luo, Shuhui Yu, Rong Sun, and Ching-Ping Wong. Nano Ag-deposited $BaTiO_3$ hybrid particles as fillers for polymeric dielectric composites: toward high dielectric constant and suppressed loss. *ACS applied materials & interfaces*, 6(1):176–182, 2013.

[253] Uvais Valiyaneerilakkal, Amit Singh, Kulwant Singh, CK Subash, SM Abbas, Rama Komaragiri, and Soney Varghese. Ferroelectric characteristics of mfis structure with p (vdf–trfe)/batio3 nanocomposite as ferroelectric layer. *Applied Physics A*, 117(3):1535–1540, 2014.

[254] Sara Dalle Vacche, Fabiane Oliveira, Yves Leterrier, Véronique Michaud, Dragan Damjanovic, and Jan-Anders E Månson. Effect of silane coupling agent on the morphology, structure, and properties of poly (vinylidene fluoride–trifluoroethylene)/batio3 composites. *Journal of Materials Science*, 49(13):4552–4564, 2014.

[255] Fang Fang, Wenhu Yang, Shuhui Yu, Suibin Luo, and Rong Sun. Mechanism of high dielectric performance of polymer composites induced by batio3-supporting ag hybrid fillers. *Applied Physics Letters*, 104(13):132909, 2014.

[256] David Black, Iulia Salaoru, and Shashi Paul. Route to enhance the efficiency of organic photovoltaic solar cells-by adding ferroelectric nanoparticles to p3ht/pcbm admixture. *EPJ Photovoltaics*, 5:50403, 2014.